SINTERED COMPOSITES PRODUCED FROM DIFFUSION-BONDED POWDERS MIXED WITH SIC CERAMIC

AUNG ZAW MYO

A THESIS REPORT SUBMITTED IN PARTIAL FULFILLMENT

OF THE REQUIREMENT FOR THE DEGREE OF

MASTER OF ENGINEERING IN AUTOMOTIVE ENGINEERING

SCHOOL OF ENGINEERING

KING MONGKUT'S INSTITUTE OF TECHNOLOGY LADKRABANG

YEAR 2024

KMITL-2024-EN-M-277-206

Thesis	Sintered composites produced from diffusion-bonded powders mixed with SiC ceramic
Student	Mr. Aung Zaw Myo
Student ID.	65016112
Degree	Master of Engineering
Program	Automotive and Advanced Transportation Engineering
Year	2024
Thesis Advisor	Asst. Prof. Dr. Mek Srilomsak
Co-Thesis Advisor	Dr. Ruangdaj Tongsri
Co-Thesis Advisor	Prof. Dr. Kazuaki Inaba

ABSTRACT

Powder metallurgy is commonly used in automotive, aerospace, and marine parts. However conventional sintered composites typically exhibit low ductility due to porosity, which originates from voids at powder particle corners in a green compact. Reduction of porosity can be achieved through novel processing techniques such as warm compaction, high velocity compaction, double compaction, and double sintering, although these methods may increase production costs. A new approach for enhancing the strength and ductility of sintered steel involves matrix modification and porosity reduction. This study explores the incorporation of 4.0 wt% silicon carbide instead of graphite into various diffusion-bonded powders, including Distaloy SA, Distaloy AE, Distaloy DH, and Distaloy DC1, resulting in the formation of pore-filling particles known as black particles and the emergence of ausferrite in the sintered steel matrix. The presence of ausferrite and pore-filling particles contributes to promising tensile strengths with low yield ratios and elongation values exceeding 5.0%. Under a normal load of 15N, sintered Distaloy DH + 4.0 wt. % SiC exhibits the highest coefficient of friction (COF), while sintered Distaloy DC1 + 4.0 wt. % SiC demonstrates the lowest COF. The inclusion of nickel (Ni) in Distaloy DC1 appears to positively affect the friction coefficient of sintered Distaloy composites. Among all sintered Distaloy composites, Distaloy SA + 4.0 wt. % SiC displays the highest average specific wear rate due to its

dual-phase ADI microstructure, whereas Distaloy AE + 4.0 wt. % SiC exhibits the lowest average specific wear rate owing to its ausferrite-MA ADI microstructure. Distaloy SA + 4.0 wt. % SiC demonstrates the highest average volume loss among all sintered Distaloy composites, attributed to its dual-phase ADI microstructure, whereas Distaloy AE + 4.0 wt. % SiC exhibits the lowest average volume loss due to its ausferrite-MA ADI microstructure. Analysis of the worn surface and wear debris of sintered Distaloy composites reveals that the primary wear mechanism consists of delamination, abrasive, and some oxidative wear, with additional observations of oxide fragment, tribo film, debris/oxide, micro crack, oxide forming, and black particle. Despite having the smallest hardness value compared to other sintered Distaloy composites, counter ball surfaces rubbing against sintered Distaloy SA + 4.0 wt. % composite exhibit the highest level of surface damage.

Keywords: Sintering, Silicon carbide, Austempered ductile iron microstructure, Ausferrite, and Tensile properties.

ACKNOWLEDGEMENTS

I express my deepest gratitude to the Thailand Advanced Institute of Science and Technology and Tokyo Institute of Technology (TAIST-Tokyo Tech) for the scholarship provided, a collaborative program between the National Science and Technology Development Agency (NSTDA, Thailand) and Tokyo Institute of Technology (Tokyo-Tech, Japan).

I would like to extend my appreciation to my thesis advisor, Dr. Ruangdaj Tongsri, for his invaluable suggestions and guidance throughout the planning and execution of this research project. I am also grateful to Asst. Prof. Dr. Mek Srilomsak from the Departments of Mechanical Engineering at King Mongkut's Institute of Technology Ladkrabang and Prof. Dr. Kazuaki Inaba from the Departments of Mechanical Engineering at Tokyo Institute of Technology, Japan, for their support and advice.

Special thanks are due to the National Science and Technology Development Agency (NSTDA) for financial support and to the staff and researchers at the Powder Metallurgy Research and Development Unit of the National Metal and Materials Technology Center (MTEC) for their assistance and technical guidance.

Lastly, I would like to express my gratitude to all lecturers and colleagues who have supported me throughout this journey. I am also thankful to my aunties for their unwavering support and encouragement. The completion of this thesis would have been impossible without the backing and inspiration from these individuals.

Aung Zaw Myo

TABLE OF CONTENTS

Page

LIST OF TABLES

Table Page

LIST OF FIGURES

Figure Page

LIST OF ABBREVIATIONS AND SYMBOLS

PM	Powder Metallurgy
C	Carbon
Si	Silicon
Mo	Molybdenum
Cu	Copper
Ni	Nickel
Fe	Iron
NRA	Nickel Rich Area
SiC	Silicon Carbide
DH	Distaloy DH
DC1	Distaloy DC1
SA	Distaloy SA
AE	Distaloy AE
Cr	Chromium
Fe_3C	Cementite
COF	Coefficient of friction
ADI	Austempered Ductile Iron
Bcc	Body centered cubic
Fcc	Face centered cubic
M-A	Martensite-Austenite
OM	Optical Microscope
SEM	Scanning Electron Microscope
TEM	Transmission Electron Microscopy
HIP	Hot Isostatic Pressing
EPMA	Electron Probe Micro-Analysis
XRD	X-Ray Diffraction Analysis
HEAs	High-Entropy Alloys
BP	Black Particle
AUS	Ausferrite
D_0	The degree of densification
ρ_a	The apparent density

ρ_s	The density of the fully consolidated metal
R	The universal gas constant
Ms	Martensite start temperature
α-Fe	Alpha Ferrite
γ- Fe	Gamma Austenite
Ps	The pearlite start temperature
Bs	Bainite start temperatures
μ	Friction Coefficient
f	The frictional force acting between two surfaces in contact
F_{load}	The normal force exerted on two surfaces

CHAPTER 1
INTRODUCTION

1.1 RESEARCH BACKGROUND

According to the nowadays technology is modern and developing expeditiously, producing sintered composites materials from diffusion-bonded powders mixed with silicon carbide ceramic are significantly related with the innovative transportation automotive industry by influencing various aspects of new materials and innovative component development. The work of (Backhaus-Ricoult, 1990) on interfaces between SiC and metals provides fundamental insights into the intricate interplay between SiC and metal matrices, laying the groundwork for the development of robust composites [1]. Sintered composites with SiC ceramic reinforcement exhibit superior mechanical properties, including increased hardness, wear resistance, and tensile strength. These properties are highly desirable in the automotive industry for components such as engine parts, gears, and bearings, contributing to improved performance and durability. (Schiepers et al., 1993) delve into the interaction between SiC and Ni, Fe, (Fe,Ni), and steel, unraveling the morphology and kinetics involved. This research is pivotal in comprehending the dynamic processes governing the formation of metal matrix composites [2]. (Pelleg, 1999)'s study on reactions in the matrix and interface of the Fe-SiC metal matrix composite system contributes valuable knowledge, shedding light on the mechanisms influencing the composite's structural and mechanical properties [3]. The lightweight nature of sintered composites aligns with the automotive industry's emphasis on lightweighting to enhance fuel efficiency in vehicles. Components with reduced weight contribute to lower fuel consumption and reduced emissions, essential factors in advanced transportation solutions.

The solid-state reaction between silicon carbide and iron, investigated by (Tang et al., 2002), is a cornerstone in understanding the chemical and physical transformations during the synthesis of sintered composites [4]. (Kalogeropoulou et al., 1995)'s research on the relationship between wettability and reactivity in the Fe/SiC system enhances the comprehension of the wetting behavior of molten metals on SiC, a critical aspect of composite fabrication [5]. SiC ceramic, when integrated into sintered composites, enhances their tribological properties. This is crucial for the automotive

industry, where components like brake systems, clutches, and transmission parts require materials with excellent wear resistance and low friction coefficients. (Kawanishi et al., 2009)'s exploration of the equilibrium phase relationship between SiC and a liquid phase in the Fe-Si-C System contributes critical data on the high-temperature behavior of the system, crucial for optimizing processing conditions [6].

Thermal Stability of SiC ceramic reinforcement provides sintered composites with improved thermal stability. In the automotive sector, this is valuable for components operating under high-temperature conditions, such as exhaust systems and engine components, contributing to increased reliability and longevity. (Tongsri and Vetayanugul, 2010)'s thermal analysis of Fe-carbide and Fe-C mixtures provides insights into the thermodynamics of the sintering process, aiding in the development of optimized processing parameters [7]. The ability to mix SiC ceramic with diffusion-bonded powders in the sintering process allows for the customization of materials to meet specific automotive requirements. Tailoring materials for applications such as electric vehicles (EVs) or high-performance sports cars is crucial for achieving optimal performance. The thermodynamic aspects during the processing of sintered materials, as studied by (Klein et al., 2015) , further enrich the understanding of the underlying principles governing the synthesis of sintered composites [8]. (Chakthin et al., 2008)'s work on the effect of the reaction between Fe and carbide particles on mechanical properties offers crucial insights into tailoring the mechanical performance of Fe-based composites [9].

Sintered composites produced through diffusion bonding enable the creation of complex geometries with high precision. This is advantageous for manufacturing intricate automotive components that require specific shapes and dimensions, promoting efficient and cost-effective production. The exploration of sintered Fe-Mo-Mn-Si-C alloys [10,12] and Fe-Mo-Si-C alloys with a ductile cast iron microstructure [11] showcases the versatility and potential of diverse compositions in tailoring the properties of sintered composites. (Nithimethakul et al., 2021)'s investigation into the effect of molybdenum on the microstructure and mechanical behavior of the sintered Fe-Mo-Mn-Si-C composite further expands the knowledge base on alloy design considerations [12].

As the automotive industry increasingly embraces electric vehicles, sintered composites can play a pivotal role in manufacturing components for electric vehicles EVs. These materials can be tailored for electric motor components, battery enclosures, and other parts critical to the functioning of electric propulsion systems. In the broader context, the development of powder metallurgy parts for automotive applications [13-14] and the finite element modeling of metal powder compaction processes underscore the practical implications of advancements in sintered composites for real-world applications [15]. Studies on high-velocity compaction mechanisms [16] and the effect of double pressing/double sintering on the sliding wear of self-lubricating sintered composites provide valuable insights into optimizing processing routes for enhanced composite performance [17]. The near-net-shape manufacturing capability of sintered composites reduces material waste, aligning with the automotive industry's commitment to sustainability and minimizing environmental impact in the production process. (Atkinson and Davies, 2000)' overview of fundamental aspects of hot isostatic pressing contributes to the understanding of alternative processing techniques, broadening the scope of methodologies available for sintered composite fabrication [18]. The adaptability of sintered composites with SiC ceramic reinforcement positions them as materials capable of meeting the evolving needs of advanced transportation technologies. This includes advancements in autonomous vehicles, connected transportation systems, and other emerging trends. (Ruangchai et al., 2017)'s work on the microstructure, hardness, and wear properties of sintered Fe-Mo-Si-C steels emphasizes the importance of comprehensive characterization to tailor composites for specific applications [19]. The effect of molybdenum on the microstructure and mechanical behavior of sintered Fe-Mo-Mn-Si-C composites adds another dimension to the alloy design considerations, illustrating the potential for optimizing properties through alloying [20].

The cost-effectiveness of sintered composites in large-scale production makes them viable for mass manufacturing in the automotive industry. This cost efficiency is essential for ensuring competitiveness and affordability in the production of vehicles and their components. (Morakotjinda et al., 2023)'s exploration of the promotion of ausferrite formation in as-sintered Fe-Mo-Si-C-(Cu) composites due to copper addition presents an innovative avenue for tailoring microstructures and properties [21]. The

investigation into sintered Fe-Ni-Si-C alloys adds to the diversity of compositions explored, providing a holistic perspective on the range of materials that can be synthesized using the proposed methodology [22]. The use of sintered composites produced from diffusion-bonded powders mixed with SiC ceramic brings forth materials with tailored properties that directly address the demanding requirements of the automotive and advanced transportation industry. From lightweighting and improved mechanical properties to thermal stability and adaptability to new technologies, these composites play a crucial role in shaping the future of transportation materials.

In this study, sintered composites were produced by combining four distinct powders, as outlined as Distaloy DH (1.47Mo-2.0Cu), Distaloy DC1 (1.50Mo-2.0Ni), Distaloy SA (0.50Mo-1.50Cu-1.75Ni) and Distaloy AE (0.50Mo-1.50Cu-4.00Ni) with a constant 4 wt. % SiC silicon carbide powder. This research study encompassed an examination of the microstructures, mechanical characteristics, and dry-sliding behaviors exhibited by the resulting sintered composites. The admixing of some alloying powders, such as nickel (Ni) and copper (Cu) powders, to iron (Fe) or Fe-based powders encounters a segregation problem leading to heterogeneous microstructures. The sluggish diffusion of alloying Ni element in Fe or Fe-based matrix causes a problem concerning the formation of nickel rich area (NRA) [23]. Weak NRA is detrimental to fatigue property in a sintered steel [24]. Although the use of diffusion-alloyed powders, produced by making metallic bonding of alloying powders onto the surface of Fe or Fe-based powder, can alleviate the segregation problem, the problem concerning the NRA formation still exists [25,26]. In previous studies, the admixing of Cu [27] or Ni and Cu [28] powder to pre-alloyed Fe-Mo powder has no NRA problem in sintered materials. This may hint that the materials processing condition, consisting of sintering at 1250 °C for 45 minutes and under vacuum atmosphere, and slow cooling, can reduce the NRA problem. However, it is still curious that the materials processing condition given above can reduce the NRA problem when the diffusion-bonded powders having Ni satellites are employed. In the case that the use of diffusion-bonded powders is successful without NRA problem, it can be proved that the material processing condition is a universal method for all types of Fe or Fe-based powders.

1.2 OBJECTIVES

The objectives are as the followings:

1) To prove that diffusion-bonded powders, namely Distaloy DH, Distaloy DC1, Distaloy SA and Distaloy AE powders, can be used to produce sintered 4.0 wt. % SiC-added materials without NRA problem under the materials processing condition, consisting of sintering at 1250 °C for 45 minutes and under vacuum atmosphere, and slow cooling.
2) To investigate microstructures, mechanical properties, and tribological properties of sintered materials produced from the mixtures of diffusion-bonded powders mixed with 4.0 wt. % SiC.

1.3 SCOPES

The scopes are as the followings:

1) Mixing Distaloy DH (1.47Mo-2.0Cu), Distaloy DC1 (1.50Mo-2.0Ni), SA (0.50Mo-1.50Cu-1.75Ni) and AE (0.50Mo-1.50Cu-4.00Ni) with 4 wt.% percent weight of silicon carbide SiC.
2) Uniaxial compacting powder mixture and sintering at 1250 °C for 45 mins in vacuum furnace and slow cooling down to room temperature with a rate of 0.1 °C/s.
3) Observation on microstructure of sintered Distaloy DH, Distaloy DC1, Distaloy SA and Distaloy AE composites by optical microscope OM, color optical microscopy OM and scanning electron microscope SEM, and phase identification of sintered composites by X-ray diffraction XRD.
4) Characterizing mechanical properties of sintered Distaloy DH, Distaloy DC1, Distaloy SA and Distaloy AE composites by tensile test and Rockwell macro hardness test.
5) Chemical distribution of sintered Distaloy DH, Distaloy DC1, Distaloy SA and Distaloy AE composites was determined by electron probe micro analyzer EPMA.

6) Utilization of pin-on-disk wears testing machine to study dry sliding wear behavior of sintered Distaloy DH, Distaloy DC1, Distaloy SA and Distaloy AE composites.
7) Observation of tribological properties from the wear testing of sintered Distaloy DH, Distaloy DC1, Distaloy SA and Distaloy AE composites by energy dispersive X-ray spectroscopy EDS and scanning electron microscopy SEM.

1.4 EXPECTED BENEFITS

To be able to produce sintered composites from diffusion-bonded powders mixed with SiC consisting of black particle enveloped with matrix microstructure with improved ductility. To apply the good mechanical properties and tribological properties for the future sintered composites producing from diffusion-bonded powders mixed with silicon carbide powder.

CHAPTER 2

LITERATURE REVIEW

2.1 POWDER METALLURGY (PM)

The automotive and advanced transportation industry heavily relies on powder metallurgy (PM) to revolutionize and enhance material properties. This critical connection between powder metallurgy and these sectors is underscored by numerous pivotal elements. The use of powder metallurgy for the manufacture of automobile components as shown in figure 2.1 [29].

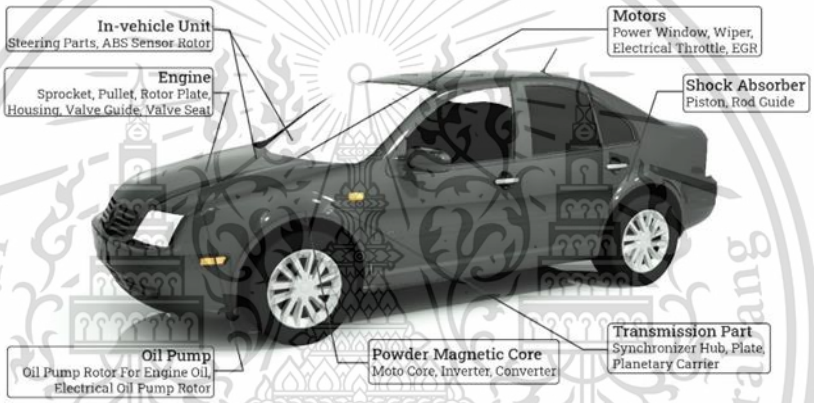

Figure 2. 1 The use of powder metallurgy for the manufacture of automobile components [29].

Powder metallurgy offers material design flexibility, enabling the creation and manufacturing of materials customized to meet the precise requirements of the automotive industry. This encompasses the attainment of targeted strength, hardness, and wear resistance properties. Powder metallurgy provides material design flexibility, enabling the customization and manufacture of materials with properties tailored to meet the precise requirements of the automotive industry. This encompasses the attainment of desired attributes such as strength, hardness, and wear resistance. PM techniques facilitate the development of lightweight materials possessing high strength-to-weight ratios, crucial for the automotive sector's objective of enhancing fuel efficiency and lowering emissions through lightweighting. The automobile components which are used of powder metallurgy are as shown in figure 2.2 [30].

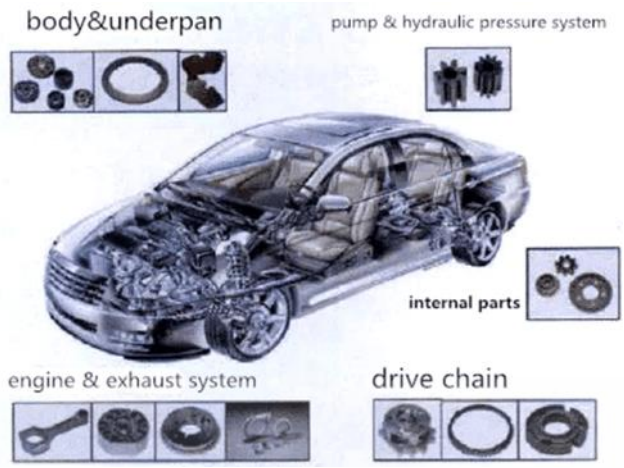

Figure 2. 2 The automobile components which are used of powder metallurgy [30].

PM techniques facilitate the production of lightweight materials characterized by high strength-to-weight ratios, crucial for achieving lightweighting objectives in the automotive sector. This advancement aligns with the industry's aims to enhance fuel efficiency and minimize emissions. PM enables the fabrication of intricate and complex shapes, offering automotive designers increased flexibility in component design, especially for parts with intricate internal structures and enhanced performance. PM offers automotive designers increased flexibility in component design by enabling the manufacture of intricate and complex shapes, particularly beneficial for creating parts with elaborate internal structures and enhanced performance. This capability enhances the production of complex geometries in the automotive industry. Due to the effectiveness of PM processes like sintering, it serves as a cost-efficient technique for the mass production of automotive parts, aligning with the industry's ongoing pursuit of cost-effectiveness and competitiveness.

Powder metallurgy processes, such as sintering, offer cost-effective means for large-scale production of automotive components, aligning with the industry's constant drive for cost efficiency and competitiveness. In components like gears, bearings, and brake systems, powder metallurgy allows for the incorporation of reinforcing elements such as ceramics, enhancing wear resistance and contributing to improved reliability and durability. Powder metallurgy enables the production of custom alloy compositions, optimizing material properties for specific automotive applications, particularly in achieving a balance between strength, ductility, and corrosion resistance.

Near-net-shape capabilities of powder metallurgy processes result in minimal material wastage during manufacturing, aligning with the automotive industry's focus on sustainability and environmental responsibility. By blending different powder components, powder metallurgy facilitates the development of advanced composite materials with enhanced performance characteristics, driving innovation in solutions for the automotive sector. As the automotive industry transitions toward electric vehicles, powder metallurgy becomes pivotal in producing components for electric motors, battery systems, and other critical parts due to its precision and efficiency. Powder metallurgy materials find applications in components subjected to friction and wear, such as engine parts and transmission components, allowing for the tailoring of materials for specific tribological properties crucial for improving efficiency and longevity.

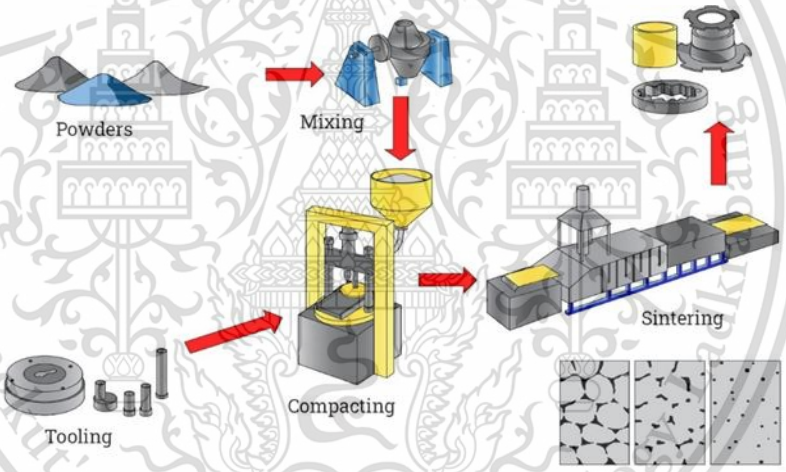

Figure 2. 3 Stages of powder metallurgy process [31].

Powder metallurgy involves the manufacturing of metal parts and components using metal powders. Typically, the process encompasses multiple stages.

2.1.1 Powder Production

Powder production marks the initial phase, focusing on creating metal powders. This can be accomplished using diverse methods like atomization, chemical precipitation, mechanical comminution (such as milling or grinding), or electrolytic techniques.

2.1.2 Powder Blending

Should the desired alloy composition necessitate the amalgamation of various metal powders, blending may be conducted to attain the desired composition.

2.1.3 Compaction

During this phase, the metal powder is subjected to high pressure within a die and punch setup to form a desired shape. The objective is to produce a "green compact" possessing the intended shape and dimensions.

2.1.4 Sintering

Following compaction, the green compact undergoes sintering, a process where it is exposed to elevated temperatures in a controlled environment, typically a furnace. Throughout sintering, the metal particles fuse together, yielding a dense, solid structure with enhanced strength and density.

2.1.5 Sizing

Occasionally, post-sintering procedures like sizing or coining are conducted to meet stricter dimensional tolerances or achieve surface textures.

2.1.6 Heat Treatment.

Heat treatment might be conducted to further improve the mechanical or physical characteristics of the final component, depending on its intended properties.

2.1.7 Finishing Operations

Following sintering and any supplementary procedures, finishing tasks like machining, grinding, polishing, or coating could be executed to attain the desired surface texture and dimensional precision of the final component.

The sequence of these phases might differ based on the specifications of the component and the materials applied. Powder metallurgy presents benefits such as the capacity to fabricate intricate geometries, optimal utilization of materials, and the potential for cost reduction in contrast to conventional machining techniques. To sum up, powder metallurgy plays a pivotal role in advancing novel materials for the automotive and advanced transportation sector. Its adaptability, cost efficiency, and capability to address the evolving needs of these industries establish it as an

indispensable technology in the quest for more efficient, robust, and eco-friendly transportation solutions.

2.2 POWDER CHARACTERISTIC

Powder metallurgy involves a variety of powder characteristics that impact powder behavior and performance throughout processing and in the finished sintered product. These traits comprise:

2.2.1 Particle Size Distribution

The spread of particle sizes influences compaction, green density, and sintering kinetics. Consistency in particle size distribution is key for uniform compaction and sintering outcomes.

2.2.2 Particle Shape

The morphology of powder particles whether spherical, irregular, or angular affects flowability, packing density, and interparticle friction. Spherical particles tend to flow more freely, and pack tightly compared to irregular or angular particles.

2.2.3 Surface Area

Powder particle surface area affects reactivity, sintering kinetics, and the interaction with additives or binders. Powders with high surface area may require additional processing steps to manage surface effects during sintering.

2.2.4 Flowability

Flowability refers to a powder's ability to move under gravity or applied pressure. It is influenced by factors such as particle size, shape, surface texture, and the presence of lubricants or binders.

2.2.5 Density

Bulk and tap densities determine packing behavior and green density in compacted parts. Higher powder densities typically yield greater green densities and improved sintering results.

2.2.6 Flow Rate.

Flow rate measures how quickly powder moves through a defined aperture under gravitational or applied forces. It serves as an indicator of powder flowability and can be assessed using standardized methods.

2.2.7 Chemical Composition

Powder chemical composition dictates material properties and phase changes during sintering. Alloying elements are introduced to customize properties like hardness, strength, and corrosion resistance in the final sintered product.

Mastering and regulating these powder characteristics is essential for refining the powder metallurgy process and attaining desired properties in the final sintered components. Diverse techniques, including powder synthesis, particle size refinement, and surface modification, can be utilized to tailor powder characteristics for specific applications. The degree of densification (D_0) serves as a valuable metric for assessing the consolidation of powders and can be defined by Equation 2.1, where $\rho_a$represents the apparent density and $\rho_s$denotes the density of the fully consolidated metal.

$$D_0 = \frac{\rho_a}{\rho_s} \times 100 \qquad (2.1)$$

2.3 POWDER MIXING

The powder mixing process within powder metallurgy plays a pivotal role in amalgamating various metal powders and additives to attain the desired composition and characteristics in the eventual sintered item. In this procedure, diverse powders, including metal powders, alloying components, lubricants, and binders, are meticulously blended to ensure uniformity and consistent distribution of constituents.

Commencing with the precise measurement and proportioning of powder constituents according to the targeted composition, the powder mixing process unfolds. These powders are amalgamated within a mixing vessel, which might range from a drum mixer to a V-blender or a ball mill, contingent upon batch size and mixing requisites. Stringently regulating the mixing duration and intensity is essential to guarantee thorough powder amalgamation while minimizing the potential for segregation or clumping. Moreover, methods such as intermittent mixing, reverse

mixing, or vacuum mixing can be employed to augment powder dispersion and achieve uniformity. Throughout the mixing stage, additives like lubricants and binders are frequently introduced to enhance powder flowability, bolster green strength, and ease compaction. It is imperative for these additives to be uniformly dispersed throughout the powder blend to ensure consistent performance during subsequent processing phases.

Upon completion of the mixing procedure, the homogenized powder blend is poised for additional processing, such as compaction, to shape green compacts, which are subsequently sintered to yield the final components endowed with the desired attributes. In summary, the powder mixing process is indispensable for upholding the quality and performance of the eventual sintered products in powder metallurgy applications.

2.4 COMPACTION

Preceding sintering, the compaction phase is pivotal in powder metallurgy, entailing the compression of loose powder particles into a dense form. This stage is crucial for attaining the targeted density and shape of the final sintered product.

During compaction, loose powder is introduced into a die cavity and subjected to significant pressure, typically administered through a mechanical or hydraulic press. This pressure compels the powder particles to bond together, resulting in a cohesive mass. The shape of the compact often mirrors the intended geometry of the final component. The compaction process parameters, including pressure application, dwell time, and die configuration, are meticulously regulated to ensure uniform density distribution and precise dimensional consistency. Additionally, the utilization of lubricants or binders may be essential to enhance powder flow and reinforce the structural integrity of the compacted form. Subsequent to compaction, the resultant green compact progresses through additional processing stages such as debinding (if binders are utilized) and sintering. These subsequent procedures metamorphose the green compact into a fully consolidated and dense entity possessing the desired mechanical attributes [32].

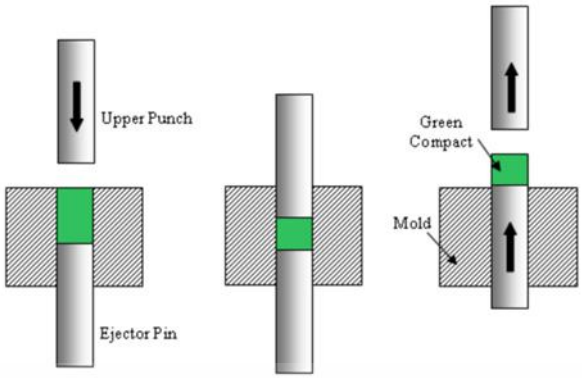

Figure 2. 4 The stages of compaction of powder (from left to right): filling, compaction, and ejection [32].

2.5 SINTERING

The sintering process, a method of heat treatment, is utilized in powder metallurgy to consolidate particles of a material, forming a solid mass without complete melting. This technique is widely employed to produce robust and intricate components. Throughout sintering, powder particles are heated to a temperature below their melting point but sufficiently high to enable atomic diffusion and bonding between neighboring particles. Typically, the sintering process comprises several stages:

2.5.1 Heating

Gradual heating of the powder compacts to the sintering temperature initiates particle bonding via atomic diffusion.

2.5.2 Dwell Time.

Upon reaching the desired temperature, the material is maintained at that level for a specific duration, known as the dwell time. This period facilitates adequate bonding between particles, resulting in the formation of a cohesive mass.

2.5.3 Cooling

Subsequent to the dwell time, the sintered material undergoes gradual cooling to ambient temperature. Swift cooling may induce thermal stresses and fracturing within the material.

2.5.4 Final Processing

Depending on the intended application, post-sintering procedures such as machining, grinding, or surface treatment may be employed to attain the desired dimensions and surface characteristics. The basics of sintering in the powder metallurgy process are as shown in figure 2.5 [33].

The efficacy of the sintering process hinges on various factors, encompassing powder composition, sintering temperature, heating rate, dwell time, and atmosphere. Optimizing these parameters is crucial to achieving the desired density, strength, and dimensional precision of the final product.

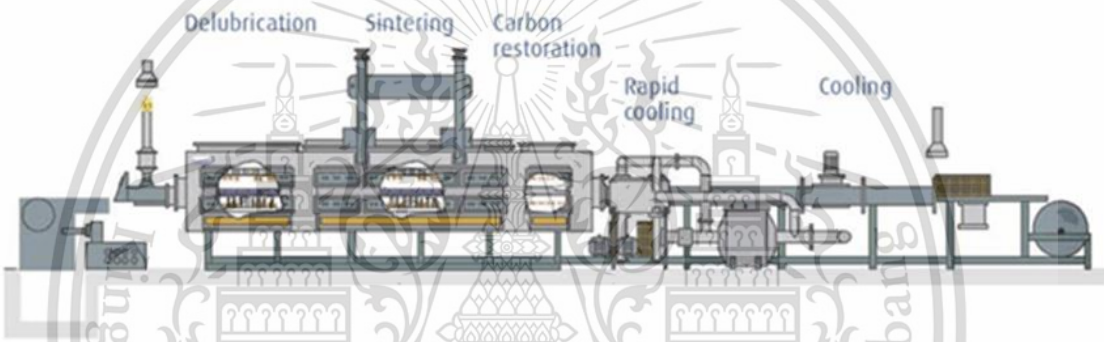

Figure 2. 5 Sintering in the powder metallurgy process [33].

2.6 SINTERING ATMOSPHERE

The sintering atmosphere, the environment where sintering occurs, can profoundly influence the properties of the resulting material. For a sintering atmosphere, the elements needed depend on the material being processed and the desired sintering conditions. However, common elements utilized include inert gases like argon, nitrogen, and helium, which establish a non-reactive setting, preventing material oxidation. Hydrogen is frequently employed in sintering atmospheres to reduce oxides and eliminate surface contaminants, enhancing sintering quality and densification.

Carbon monoxide and carbon dioxide can also be utilized to create reducing atmospheres, facilitating oxygen removal from the material and improving sintering kinetics. Alternatively, a vacuum environment may be employed in certain instances

to remove gases, creating a low-pressure setting that prevents oxidation and enhances material densification. The specific combination and proportions of these elements in the sintering atmosphere are customized to meet the requirements of the sintering process and achieve the desired properties in the final sintered product.

2.7 DISTALOY ELEMENTS

Distaloy, a series of iron-based powder metallurgy materials, was innovated by Höganäs AB. The composition of Distaloy varies based on the grade and intended application. Generally, Distaloy alloys contain elements like iron, carbon, copper, nickel, molybdenum, and occasionally other additives to enhance specific properties. These elements are meticulously chosen and adjusted to attain the desired mechanical, magnetic, and corrosion-resistant characteristics in the resulting sintered product.

2.7.1 Effects Of Distaloy Elements On Transformation Diagrams

The transformation diagrams, like phase diagrams or TTT (Time-Temperature-Transformation) diagrams, are notably impacted by the inclusion of diverse alloying elements in Distaloy materials. For instance, when elements such as nickel or molybdenum are introduced, they can cause shifts in phase boundaries or modify the kinetics of phase transformations, resulting in modifications to the microstructure and properties of the ultimate sintered product. These alterations are reflected in transformation diagrams by variations in phase compositions, transformation temperatures, and the emergence of new phases or microstructural characteristics.

2.7.2 Effect Of Distaloy Elements On Ferrite Hardness

The impact of Distaloy elements on ferrite hardness can fluctuate based on the alloying elements and their levels. For instance, carbon and nickel tend to enhance ferrite hardness through solid solution strengthening and the creation of carbides or intermetallic compounds. Conversely, manganese might lower ferrite hardness due to its effect on grain size and crystal structure. Consequently, the composition of Distaloy materials, encompassing the variety and concentrations of alloying elements, profoundly influences the ferrite hardness in the resultant sintered product.

2.7.3 Effect Of Distaloy Elements On The Formation Of Alloy Carbides

Distaloy elements play a significant role in shaping the formation of alloy carbides within sintered materials. Chromium, molybdenum, and tungsten, among other alloying elements, are known to facilitate carbide formation due to their strong affinity for carbon. These carbides are pivotal for enhancing the hardness and wear resistance of the final product. However, the precise impact hinges on factors such as element composition, concentration, and sintering conditions. Consequently, meticulous selection and balancing of alloying elements in Distaloy materials are paramount for optimizing carbide formation and enhancing overall product performance.

2.8 DIFFUSION-BONDED MATERIALS

Diffusion bonding creates composite materials by fusing two or more solid components through controlled heating and pressure, enabling atoms to diffuse across the interface and create strong bonds. This method is typically carried out in a vacuum or inert gas environment to prevent material contamination and oxidation. It's particularly useful for joining dissimilar materials like metals, ceramics, or composites that have disparate melting points or compositions, challenging to weld conventionally. The resulting diffusion-bonded materials boast exceptional mechanical properties, including superior strength, ductility, and resistance to fatigue, thanks to defect-free interfaces. This makes them well-suited for applications demanding dependable and resilient joints, such as aerospace, automotive, and medical sectors.

Techniques such as solid-state diffusion bonding, transient liquid phase bonding, and diffusion brazing are commonly employed, each with its advantages and limitations, depending on the materials involved and specific application needs. In summary, diffusion-bonded materials offer a flexible and efficient solution for uniting dissimilar materials, allowing for the creation of intricate and high-performing components across various industries.

2.9 MICROSTRUCTURE

The microstructures of sintered composite materials describe how the constituent phases and features are arranged and distributed within the material on a microscopic level, and these structures significantly influence the mechanical, thermal, and electrical properties of the material. Sintered composite materials are typically composed of various phases, including the matrix phase and additional reinforcement or additive phases like SiC particles, and the microstructure of these composites is shaped by factors such as material composition, processing conditions, and post-treatment methods. When observed under a microscope, the microstructure of sintered composites can reveal characteristics such as grain boundaries, pores, intermetallic phases, and the dispersion of particles. The arrangement and orientation of reinforcement phases within the matrix have a profound impact on the material's mechanical properties, such as its strength, stiffness, and resilience.

The analysis of the microstructures of sintered composite materials often employs techniques such as optical microscopy, scanning electron microscopy (SEM), and transmission electron microscopy (TEM), allowing researchers to examine the morphology, size, and distribution of phases and features with precision. A comprehensive understanding of the microstructures of sintered composite materials is vital for optimizing processing parameters, predicting material performance, and tailoring properties to meet specific application requirements. By manipulating the microstructure, engineers and researchers can develop composite materials with superior performance and reliability. The microstructures and TTT Diagram obtained by different types of cooling rates are shown in figure 2.6 [34].

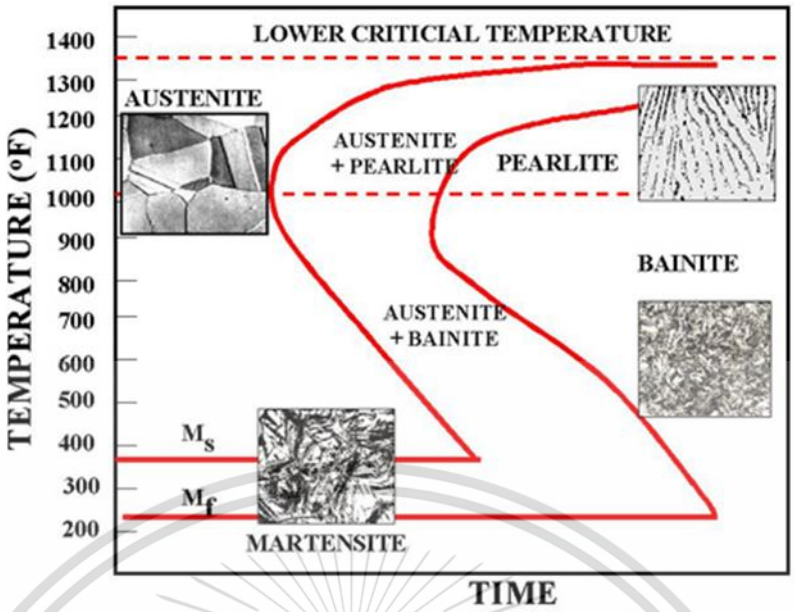

Figure 2. 6 Microstructures and TTT Diagram obtained by different types of cooling rates [34].

2.9.1 Ferrite Microstructure

Ferrite is a phase in steel with a body-centered cubic (BCC) crystal structure. It forms during the cooling of austenite or as a primary phase in certain steel compositions. Ferrite has relatively low hardness and strength, but it offers high ductility. The magnetic behavior of ferrite can vary; alpha-ferrite is ferromagnetic, while delta-ferrite is typically non-magnetic. The carbon content in ferrite is typically low compared to other phases in steel and the micrograph of microstructure of ferrite is shown in figure 2.7 [35].

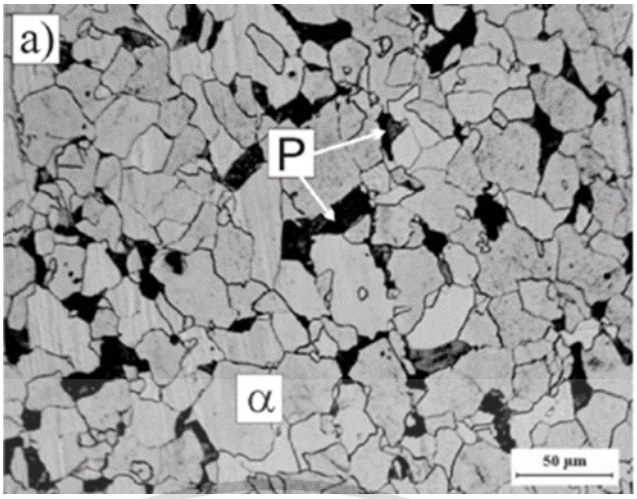

Figure 2. 7 The micrograph of microstructure of ferrite [35].

Ferrite is a magnetic, body-centered cubic (BCC) crystalline structure of iron. It is the softest and most ductile phase of iron and steel. Ferrite is stable at low temperatures and is the phase from which most steels are transformed to form their final microstructure by heat treatment. The ferrite microstructure is typically characterized by a grain structure with grain boundaries. The grains can vary in size and shape, but they are typically equiaxed (equally dimensioned in all directions). The grain boundaries are often decorated with precipitates, such as carbides or nitrides. Ferrite can also contain other phases, such as austenite, martensite, or bainite. The presence of these other phases depends on the composition and heat treatment history of the steel.

Ferrite is an important phase for many different applications. For example, ferrite is the phase that is present in mild steels and ferritic stainless steels. Ferrite is also used to produce high-purity iron for electrical and electronic applications. Examples of applications where ferrite is used are mild steel components, ferritic stainless-steel components, electrical and electronic components, magnetic components, core materials for transformers and motors. Ferrite is a versatile and important phase in steel. It is used in a wide range of applications due to its soft, ductile, and magnetic properties.

2.9.2 Austenite Microstructure

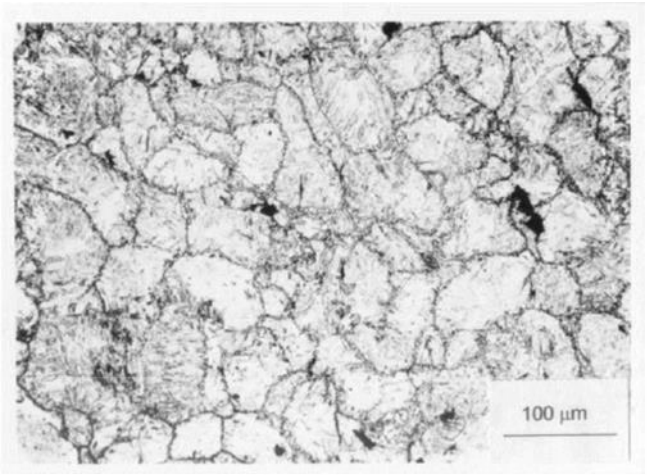

Figure 2. 8 The micrograph of microstructure of austenite [36].

Austenite is characterized by its face-centered cubic (FCC) crystal structure, making it more ductile than other phases like martensite. It forms at higher temperatures and exhibits relatively lower hardness and strength compared to martensite. The non-magnetic nature of austenite is a result of its FCC structure. The carbon content can vary, influencing the alloy's overall behavior. Austenite's high ductility makes it suitable for applications where plastic deformation is desired and the micrograph of microstructure of austenite is shown in figure 2.8 [36].

Austenite has a face-centered cubic (FCC) crystal structure, which is the densest packing of atoms. This gives austenite a high strength and toughness. Austenite is also non-magnetic. Austenite is the only phase of steel that can exist at room temperature when the carbon content is below 0.8%. However, it is not stable at room temperature and will eventually transform into other phases, such as ferrite and pearlite. The transformation of austenite to other phases is what gives steel its strength and hardness. Austenite is an important phase in steel because it is the phase that is responsible for the hardenability of steel. Hardenability is the ability of a steel to become hard when it is quenched. Steels that have a high austenite carbon content have a higher hardenability than steels with a low austenite carbon content. Austenite is also an important phase in stainless steels because it is the phase that gives stainless steels their corrosion resistance. The austenite phase is resistant to corrosion because it is a solid solution of chromium and nickel.

Austenite is a very important phase in steel and stainless steel, and it is the subject of much research. Austenite is a non-magnetic, face-centered cubic (FCC)

crystalline structure of iron and carbon. It is stable at high temperatures and is the phase from which most steels are transformed to form their final microstructure by heat treatment. The austenite microstructure is typically characterized by a grain structure with grain boundaries. The grains can vary in size and shape, but they are typically equiaxed (equally dimensioned in all directions). The grain boundaries are often decorated with precipitates, such as carbides or nitrides.

The austenite microstructure can also contain other phases, such as ferrite, martensite, or bainite. The presence of these other phases depends on the composition and heat treatment history of the steel. The austenite microstructure is important for many different applications. For example, austenite is the phase from which most steels are hardened by quenching. The austenite microstructure also affects the ductility, toughness, and corrosion resistance of steels.

2.9.3 Pearlite Microstructure

Pearlite is a lamellar structure composed of alternating layers of ferrite and cementite. Pearlite does not have a distinct crystal structure of its own but consists of layers of two distinct phases, ferrite, and cementite. It forms through the eutectoid reaction during the slow cooling of austenite. The hardness of pearlite is moderate, falling between the hardness of ferrite and cementite. The strength of pearlite is also moderate, making it a balanced phase in terms of strength. Pearlite exhibits good ductility, allowing for some deformation before fracture. Typically, pearlite is non-magnetic. The carbon content in pearlite is moderate, around 0.76 wt. % C.

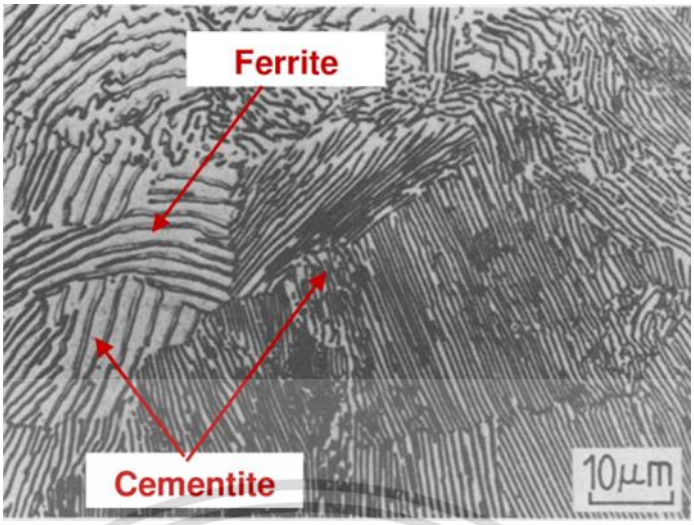

Figure 2. 9 The micrograph of microstructure of pearlite [37].

Pearlite is a common microstructure in various steels and is often found in normalized or annealed condition. Its balanced combination of strength and ductility makes it suitable for many engineering applications. Pearlite is a two-phase microstructure that consists of ferrite and cementite. It is the most common microstructure in steels and is responsible for the characteristic "pearly" appearance of steel when viewed under a microscope. Pearlite forms during the slow cooling of austenite. As the austenite cools, it transforms into ferrite and cementite. The ferrite and cementite form a lamellae structure, with alternating layers of ferrite and cementite and the micrograph of microstructure of pearlite is shown in figure 2.9 [37].

The properties of pearlite depend on the spacing of the ferrite and cementite lamellae. Pearlite with finer lamellae is harder and stronger than pearlite with coarser lamellae. Pearlite is a two-phase microstructure that forms in steel during eutectoid transformation of austenite. It is characterized by a lamellar structure of ferrite and cementite. Pearlite is the most common microstructure in steel and is responsible for many of the properties of steel, such as strength, hardness, and toughness. Pearlite is formed when austenite transforms to ferrite and cementite at a constant temperature of 723 degrees Celsius (1335 degrees Fahrenheit). This transformation is called the eutectoid transformation. The pearlite microstructure forms because the ferrite and cementite phases have the same crystal structure and can grow together in a lamellar structure.

Fine pearlite is stronger and harder than coarse pearlite, but it is also less ductile and tough. Pearlite is an important microstructure for many different applications. For example, pearlite is used in steels for its strength, hardness, and toughness. It is also used in steels for its good wear resistance and corrosion resistance. Examples of applications where pearlite is used are automotive components, aerospace components, oil and gas components, power generation components and structural steel.

2.9.4 Martensite Microstructure

Martensite is a hard and brittle microstructure that can be formed in some metals and alloys by cooling them rapidly from a high temperature. The martensite transformation is a diffusion less transformation, meaning that it occurs without the movement of atoms. Instead, the existing atoms in the metal or alloy rearrange themselves into a new crystal structure. The microstructure of martensite is characterized by a needle-like or lath-like morphology. This morphology is caused by the martensite transformation, which occurs in a series of small, localized regions called packets. The packets are separated by boundaries called prior austenite grain boundaries.

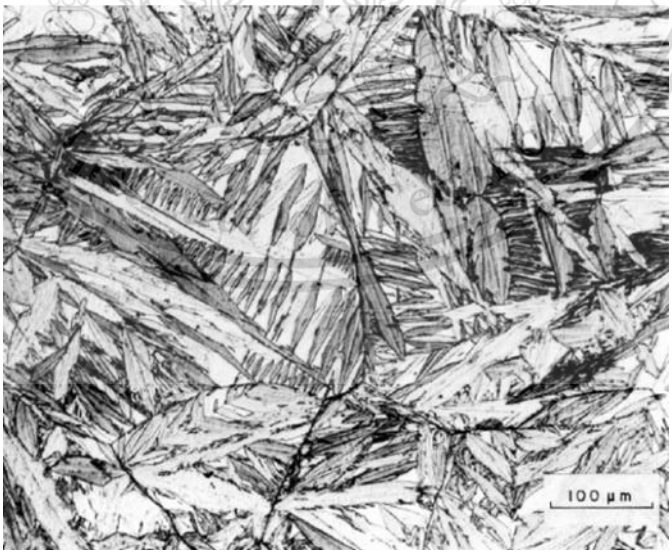

Figure 2. 10 The micrograph of microstructure of martensite [38].

The picture above shows a scanning electron microscope (SEM) image of a martensite microstructure. The needle-like and lath-like morphology of the martensite is clearly visible. Martensite is often used in applications where high hardness and strength are required, such as in cutting tools and wear-resistant parts. However, martensite is also brittle, which makes it susceptible to cracking. To improve the ductility of martensite, it can be tempered, which is a heat treatment process that partially transforms the martensite back into austenite.

Martensite is a metastable phase of steel that is formed when austenite (face-centered cubic iron) is rapidly cooled. Martensite has a body-centered tetragonal crystal structure, which is much stronger and harder than austenite. However, martensite is also more brittle and less ductile than austenite. The microstructure of martensite is characterized by needle-shaped grains called laths and the micrograph of microstructure of martensite is shown in figure 2.10 [38]. Laths are typically a few micrometers in width and tens of micrometers in length. The laths are arranged in packets, and the packets are separated by boundaries called midrib boundaries. The martensite microstructure in the image is a tempered martensite microstructure. Tempered martensite is formed by heating martensite to a temperature below the austenite transformation temperature and then quenching it. Tempering reduces the hardness and strength of martensite, but it also improves its ductility. Tempered martensite is the most common microstructure in steel products that require high strength and toughness, such as automotive parts, cutting tools, and aircraft components.

The martensite microstructure is characterized by a lath-like morphology. The laths are formed when the austenite phase transforms to the martensite phase during rapid quenching. The laths are typically aligned in a parallel or near-parallel fashion, and they are separated by boundaries called midribs. The martensite microstructure is very strong and hard, but it is also relatively brittle. This makes it ideal for applications where high strength and hardness are required, but ductility is not a critical factor. Martensite is often used in applications such as tools, dies, and wear-resistant coatings. The martensite microstructure can be visualized using a variety of microscopy techniques, including optical microscopy, scanning electron microscopy (SEM), and transmission electron microscopy (TEM). The image above shows a SEM image of a

martensite microstructure. Martensite is formed when austenite is rapidly quenched to a temperature below the martensite start temperature (Ms). The martensite transformation is a diffusion less transformation, meaning that it does not involve the diffusion of atoms. Instead, the martensite transformation is a shear transformation, meaning that the atoms in the austenite lattice are rearranged to form the new martensite lattice.

The martensite transformation is very rapid, and it can occur in as little as a few milliseconds. Martensite is known for its high hardness and strength, achieved through rapid cooling (quenching) of austenite. Its low ductility makes it brittle, but it is valued in applications where hardness and strength are paramount. The ferromagnetic property of martensite is a result of its crystal structure. The carbon content can vary, and it plays a significant role in influencing martensite's properties. This rapid transformation is what gives martensite its high strength and hardness. Martensite is a very versatile material, and it is used in a wide variety of applications. There are some of the most common applications of martensite. Martensite is often used in tools and dies because of its high strength and hardness. Martensite can be used to create wear-resistant coatings on other materials, such as steel and ceramics. Martensite is used in a variety of automotive components, such as crankshafts, camshafts, and gears. Martensite is used in a variety of aerospace components, such as landing gear and engine parts. Martensite is used in a variety of medical devices, such as scalpels and surgical instruments.

2.9.5 Bainite Microstructure

At temperatures ranging from 125 to 550 °C (depending on alloy content), bainite, a plate-like microstructure, forms in steels. Austenite, a high-temperature phase of iron with a cubic close-packed crystal structure, constitutes a typical low-carbon steel entirely above approximately 900 °C. Bainite typically appears as aggregates, termed sheaves, of ferrite plates separated by retained austenite, martensite, or cementite. The microstructure of bainite is illustrated in figure 2.11 [39].

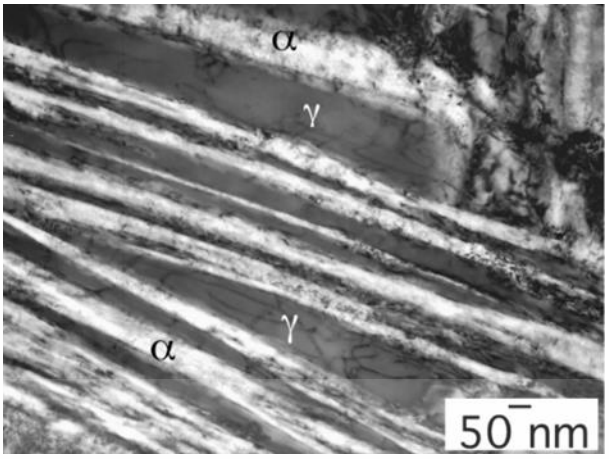

Figure 2. 11 The micrograph of microstructure of bainite [39].

Around the temperature range of 400-550 °C, upper bainite forms in sheaves. These sheaves consist of several laths of ferrite, roughly parallel to each other, exhibiting a Kurdjumov-Sachs relationship with the surrounding austenite, although this connection weakens as the transformation temperature decreases. The carbon concentration in the ferrite of these sheaves is below 0.03%, resulting in carbon-rich austenite surrounding the laths. Lower bainite, on the other hand, forms between 250 and 400 °C and adopts a more plate-like structure compared to upper bainite. In lower bainite, there are fewer low angle boundaries between the laths. Cementite nucleates at the interface between ferrite and austenite in lower bainite. The amount of cementite formed between the laths depends on the carbon content of the steel. In low carbon steel, discontinuous "stringers" or small cementite particles are typically present between the laths. In steel with higher carbon content, these stringers become continuous along the length of the adjacent laths.

Bainite is a phase in steel that forms through a process of moderate cooling from austenite. It has a mixed crystal structure, containing both ferrite and cementite. The hardness of bainite is moderate, falling between that of martensite and pearlite. Its strength is high, similar to martensite, but it offers higher ductility compared to martensite and lower than pearlite. The magnetic behavior of bainite is typically non-magnetic. The carbon content can vary, influencing the alloy's overall behavior. Bainite is a non-equilibrium microstructure that forms in steels when they are cooled rapidly from the austenite phase. It is characterized by a lath structure, with the laths oriented in the same direction. The laths are typically separated by ferrite or retained austenite.

The bainite microstructure can be classified into two types: upper bainite and lower bainite. Upper bainite forms at higher temperatures and has coarser laths than lower bainite. Lower bainite forms at lower temperatures and has finer laths than upper bainite.

The bainite microstructure is important for many different applications. For example, bainite is used in steels that require high strength and toughness, such as those used in automotive and aerospace components. Examples of the applications of bainite steels are automotive components such as crankshafts, camshafts, connecting rods, gears, axles, aerospace components such as landing gear, engine components, structural members, oil and gas industry such as drill pipes, casings, tubing, power generation industry such as turbine blades, rotors, and construction industry such as rebar, beams, columns. Bainite steels are also used in a variety of other applications, such as medical devices, cutting tools, and bearings.

2.9.6 Cementite Microstructure

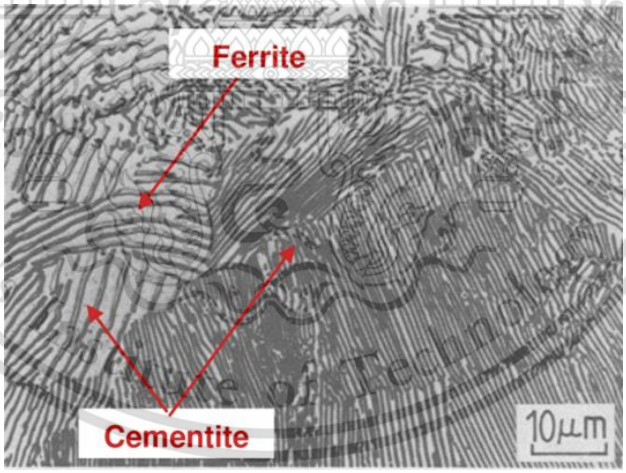

Figure 2. 12 The micrograph of microstructure of pearlite, which containing a lamellar mixture of ferrite and cementite [40].

Cementite (Fe_3C) is an iron carbide compound that often forms in conjunction with other phases like pearlite or bainite and the micrograph of microstructure of pearlite, which containing a lamellar mixture of ferrite and cementite is shown in figure 2.12 [40]. It has an orthorhombic crystal structure. Cementite is known for its very high hardness and strength, making it a hard and brittle phase in steel. It has low ductility,

and its brittleness can affect the overall mechanical properties of the steel. Cementite is typically non-magnetic. Its high carbon content (around 6.7 wt% C) contributes to its hardness and brittleness. Cementite is a hard and brittle intermetallic compound of iron and carbon (Fe_3C). It is the hardest phase of iron and is responsible for the high strength of steel. Cementite is stable at room temperature and is the major constituent of high-carbon steels and cast irons. The cementite microstructure is typically characterized by a plate-like or needle-like structure. The cementite plates can be evenly distributed throughout the microstructure, or they can be clustered together. The distribution of cementite plates has a significant effect on the strength and toughness of steel.

Cementite is a versatile phase that can be tailored to meet the specific requirements of a wide range of applications. Cementite is a hard and brittle intermetallic compound of iron and carbon with the chemical formula Fe_3C. It is the hardest phase in steel and is responsible for the strength and hardness of steel. Cementite is formed during the solidification of molten steel and the subsequent cooling of the steel. It can also be formed during heat treatment processes. Cementite is an important phase for many different applications. For example, the amount of cementite in steel affects its strength, hardness, toughness, and ductility. Cementite is also used in the production of hard metals, such as tungsten carbide and titanium carbide. Examples of applications where cementite is used are automotive components, aerospace components, oil and gas components, power generation components, cutting tools and wear parts.

2.9.7 Ausferrite Microstructure

Ausferrite is known for its unique microstructure, which includes acicular ferrite and high carbon austenite. Ausferrite has a mixed crystal structure, incorporating acicular ferrite and high carbon austenite. It forms through an isothermal transformation from austenite, typically with specific cooling rates. Ausferrite exhibits high hardness, contributing to its overall strength. Ausferrite has very high strength, making it suitable for applications requiring a combination of strength and toughness. Despite its high strength, ausferrite retains good ductility, allowing for deformation before failure. Ausferrite is typically non-magnetic. The carbon content in ausferrite

can vary, depending on the alloy composition and the micrograph of microstructure of ausferrite, which can be appreciated clearly the graphite shell as a second layer surrounding the inner nodule.is shown in figure 2.13 [41].

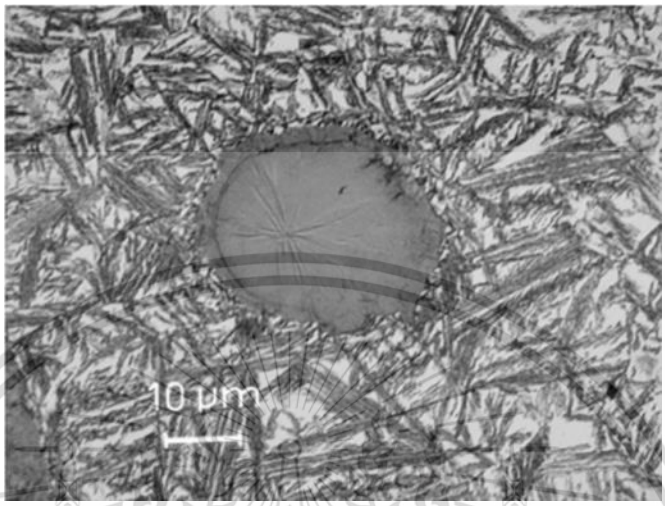

Figure 2. 13 The micrograph of microstructure of ausferrite, which can be appreciated clearly the graphite shell as a second layer surrounding the inner nodule [41].

Ausferritic steels are often used in applications where a combination of high strength, good ductility, and wear resistance is required, such as in automotive components and industrial machinery. Ausferrite is a microstructure that forms in steel during austenitic transformation at temperatures below the bainite start (Bs) temperature. It is characterized by a fine-grained structure of ferrite grains with a dispersion of fine carbides. Ausferrite is a relatively new microstructure that has been developed in recent years to improve the strength and toughness of steels. It is typically produced by quenching the steel to a temperature below the Bs temperature and then holding it at that temperature for a period of time. The holding time allows the austenite to transform to ausferrite and ausferritic structure formation (a) the nucleation of ferrite platelets, (b) the development of an ausferritic microstructure, and (c)-(e) the growth of acicular ferrite and the creation of carbon-saturated austenite are shown in figure 2.14 [42].

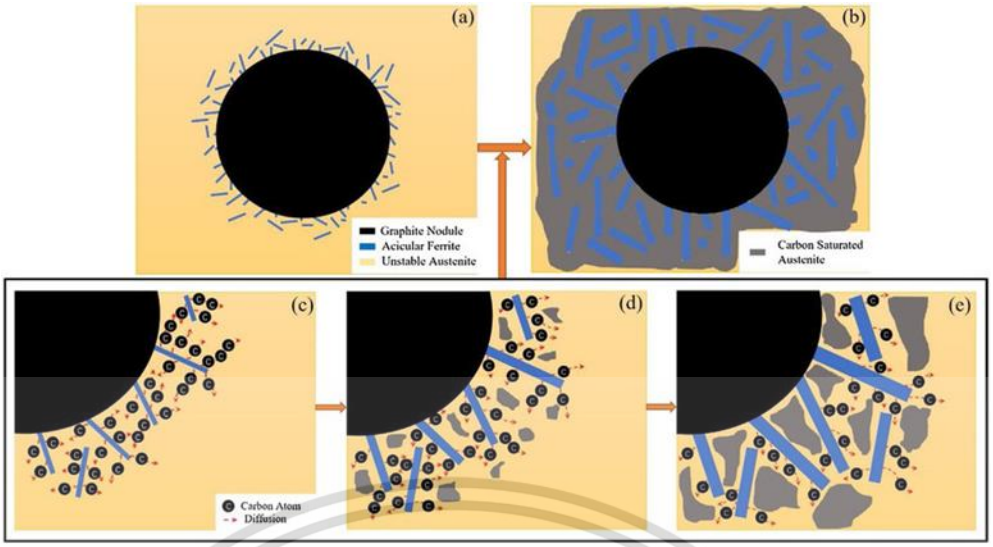

Figure 2. 14 Ausferritic structure formation (a) the nucleation of ferrite platelets, (b) the development of an ausferritic microstructure, and (c)-(e) the growth of acicular ferrite and the creation of carbon-saturated austenite [42].

Ausferrite is often used to produce high-strength steels with good toughness. It is also used to produce steel with good wear resistance and corrosion resistance. Ausferrite is a versatile microstructure that can be tailored to meet the specific requirements of a wide range of applications. Ausferrite is a microstructure that is formed when austenite is transformed to ferrite and cementite at a temperature below the pearlite start temperature (Ps). The ausferrite microstructure is characterized by a fine ferrite grain structure and a dispersion of cementite nanoparticles. Ausferrite is a microstructure that forms in steel during austenitic transformation at temperatures between the martensite start (Ms) and bainite start (Bs) temperatures. It is characterized by a fine-grained structure of ferrite grains. Ausferrite is typically classified into two types: upper ausferrite and lower ausferrite. Upper ausferrite forms at higher temperatures and has a coarser structure than lower ausferrite. Lower ausferrite forms at lower temperatures and has a finer structure than upper ausferrite.

Ausferrite has several advantages over other microstructures, including high strength, good ductility, good toughness, good wear resistance and good corrosion resistance. Examples of applications where ausferrite is used are automotive components, aerospace components, oil and gas components, power generation components, and medical devices. Ausferrite is a versatile microstructure that can be tailored to meet the specific requirements of a wide range of applications.

2.9.8 MA (Martensite-Austenite) Islands Microstructure

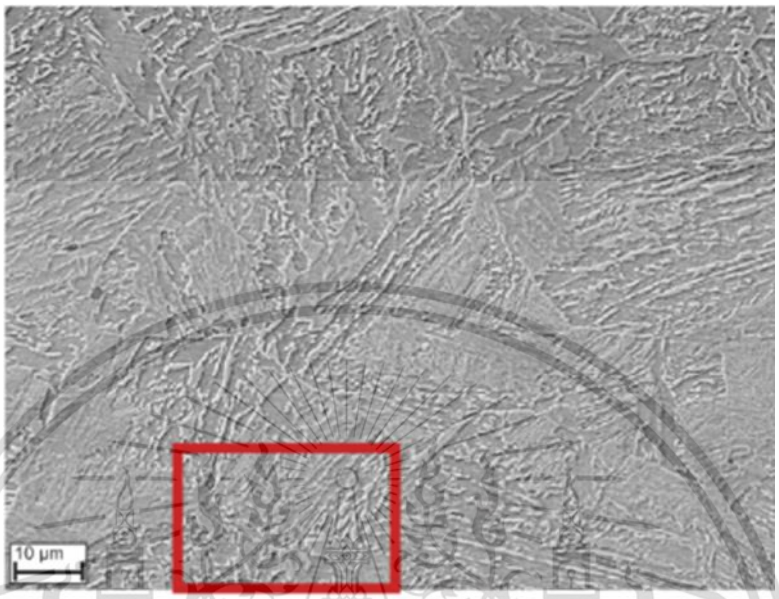

Figure 2. 15 The micrograph of microstructure of MA (Martensite-Austenite) islands, which composed of martensite in the center and austenite located at the outer rim [43].

MA islands (martensite-austenite islands) are a type of microstructure that forms in stainless steel during quenching. They are characterized by small islands of Austenite surrounded by Martensite. MA islands form when the steel is cooled too quickly during quenching. This prevents the austenite from fully transforming to martensite. Austenite islands are typically trapped within the martensite matrix and cannot transform to martensite at a later time. The presence of MA islands can have a significant impact on the properties of stainless steel. MA islands can increase the strength and hardness of the steel, but they can also reduce the toughness and ductility. MA islands are often found in stainless steel components that have been quenched to high hardness levels, such as razor blades and surgical instruments. They can also be found in stainless steel components that have been welded, as the welding process can cause the steel to be heated and cooled quickly. MA islands are an important microstructure to be aware of when designing and manufacturing stainless steel components. By understanding the formation and properties of MA islands, engineers can select the appropriate

quenching and welding parameters to produce the desired microstructure and properties and the micrograph of microstructure of MA (Martensite-Austenite) islands, which composed of martensite in the center and austenite located at the outer rim is shown in figure 2.15 [43].

Martensite is a hard and brittle microstructure that forms in steel during austenitic transformation at temperatures below the martensite start (Ms) temperature. It is characterized by a needle-like or plate-like structure of ferrite grains.MA islands are similar to martensite in terms of their microstructure and properties. However, MA islands are typically smaller and more dispersed than martensite. This is because MA islands form at lower temperatures than martensite. MA islands are often used to produce high-strength steels with good toughness. They are also used to produce steel with good wear resistance and corrosion resistance. MA (martensite-austenite) islands are a type of microstructure that forms in steel during austenitic transformation. They are characterized by small regions of austenite that are embedded in a martensite matrix. MA islands form when the steel is quenched to a temperature below the martensite start (Ms) temperature and then held at that temperature for a period of time. The holding time allows the austenite to transform to martensite. However, some of the austenite is unable to transform to martensite and remains as MA islands.

MA islands are important because they can improve the strength and toughness of steel. The martensite matrix provides strength, while the austenite islands provide toughness. Examples of applications of MA islands are automotive components, razor blades, surgical instruments, welded stainless steel components, aerospace components, oil and gas components, power generation components and medical devices. MA islands are a versatile microstructure that can be tailored to meet the specific requirements of a wide range of applications.

2.9.9 Dual-Phase Lamellar Microstructure

A dual-phase lamellar microstructure is a microstructure that consists of two different phases, typically a hard phase and a soft phase, arranged in a layered structure. The hard phase is typically much stronger than the soft phase, but it is also less ductile. The soft phase can confine and suppress the growth of necking in the hard phase, resulting in increased ductility without sacrificing strength. Dual-phase lamellar microstructures are formed by quenching steel from a high temperature to a

temperature below the martensite start temperature. This causes the austenite in the steel to transform to martensite. The martensite is a much stronger phase than the austenite, but it is also less ductile. The ferrite is a softer and more ductile phase that is not affected by the quenching process. Dual-phase lamellar microstructures offer a number of benefits. Dual-phase lamellar microstructures have a high strength due to the presence of the martensite phase. Dual-phase lamellar microstructures have a high ductility due to the presence of the ferrite phase. Dual-phase lamellar microstructures have good toughness, which is a measure of their ability to resist fracture. Dual-phase lamellar microstructures have good formability, which is a measure of their ability to be deformed without cracking and the micrograph illustrates both a lamellar microstructure and an alpha colony structure present in the test alloy is shown in figure 2.16 [44].

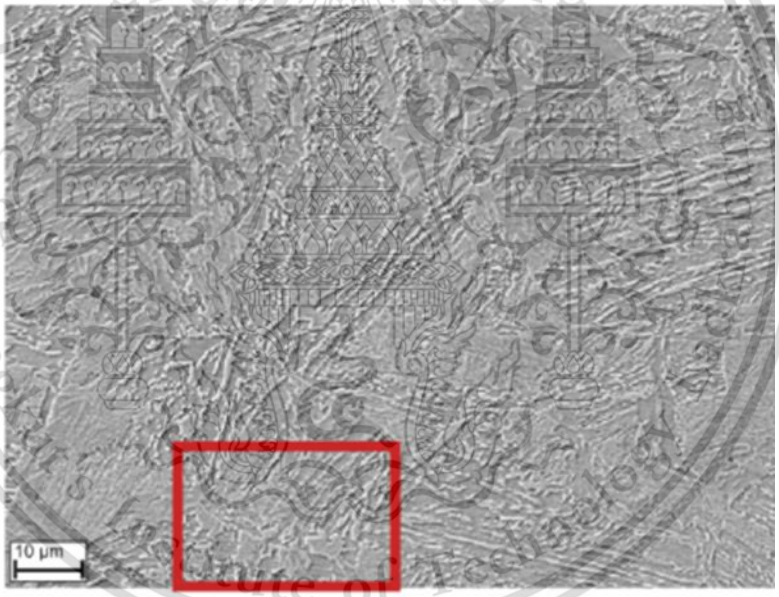

Figure 2. 16 The micrograph illustrates both a lamellar microstructure and an alpha colony structure present in the test alloy [44].

Dual-phase lamellar microstructures are a versatile and important type of microstructure that is used in a wide range of applications. They offer a number of benefits, including high strength, high ductility, good toughness, and good formability. Dual-phase lamellar microstructure is a type of microstructure in steel that consists of two different phases arranged in a layered structure: a hard phase and a soft phase. The hard phase is typically martensite, which is a very strong but brittle phase of steel.

The soft phase is typically ferrite, which is a softer and more ductile phase of steel. Dual-phase lamellar microstructures are created by quenching steel from a high temperature to a temperature below the martensite start temperature. This causes the austenite in the steel to transform to martensite. The martensite is a much stronger phase than the austenite, but it is also less ductile. The ferrite is a softer and more ductile phase that is not affected by the quenching process. The presence of ferrite in the dual-phase lamellar microstructure helps to improve the ductility of the steel. The ferrite layers can confine and suppress the growth of necking in the martensite layers. This results in a steel with both high strength and high ductility. Dual-phase lamellar microstructures are used in a variety of applications, including automotive components, aerospace components, and oil and gas components. They are particularly useful for applications where both high strength and high ductility are required.

There are some specific examples of how dual-phase lamellar microstructures are used in real-world applications. Dual-phase lamellar microstructures are used in a variety of automotive components, such as chassis parts, engine components, and body panels. They provide the strength and ductility required to withstand the demands of automotive applications, such as impact resistance and fatigue resistance. Dual-phase lamellar microstructures are also used in a variety of aerospace components, such as aircraft landing gear and helicopter rotor blades. They provide the high strength and ductility required to withstand the harsh conditions of aerospace applications, such as high temperatures and high stresses. Dual-phase lamellar microstructures are also used in a variety of oil and gas components, such as drill pipes and pipelines. They provide the high strength and ductility required to withstand the demanding conditions of oil and gas applications, such as high pressures and corrosive environments.

2.10 POROSITY

Porosity denotes the existence of empty spaces or voids within a material, typically quantified as the proportion of the material's volume occupied by these

voids. These voids can arise naturally or be deliberately introduced during various manufacturing processes like sintering, casting, or additive manufacturing.

The presence of porosity profoundly impacts the characteristics and behavior of materials, encompassing mechanical strength, thermal conductivity, and permeability. Elevated levels of porosity typically result in diminished mechanical properties and structural integrity, as these voids serve as focal points for stress concentration, reducing the material's load-bearing capacity. Porosity manifests in diverse forms, including closed porosity, where voids are not interconnected, and open porosity, which features interconnected voids allowing for the penetration of fluids or gases. The arrangement and dimensions of pores within a material also play a crucial role in determining its properties, with smaller and more uniformly distributed pores often correlating with enhanced mechanical performance.

Mitigating porosity is a prevalent objective in material processing, aiming to enhance the material's strength, ductility, and overall quality. Strategies such as optimizing processing parameters, selecting suitable additives or binders, and employing post-processing techniques like hot isostatic pressing (HIP) or vacuum impregnation are utilized to reduce porosity and enhance material properties.

2.11 DENSITY

The density of sintered composite materials plays a pivotal role in determining their mechanical, thermal, and electrical characteristics. It is conventionally quantified as the mass per unit volume, commonly expressed in grams per cubic centimeter (g/cm^3) or kilograms per cubic meter (kg/m^3). Sintered composite density is influenced by a myriad of factors, encompassing material composition, sintering process variables, and the presence of any inherent porosity or imperfections. Typically, higher densities signify greater material compactness and reduced void spaces, thereby potentially enhancing mechanical attributes like strength and rigidity.

Throughout the sintering process, powder particles undergo compaction and bonding via mechanisms such as diffusion, solid-state sintering, and liquid phase sintering. Densification dynamics are intricately linked to parameters such as temperature, pressure, duration, and the inclusion of additives or reinforcements. The

incorporation of additives or reinforcing phases, like SiC particles, can notably impact the density of sintered composite materials. These adjuncts may influence the packing density of the powder blend and the densification kinetics during sintering, ultimately shaping the ultimate density of the composite. In essence, sintered composite material density serves as a critical gauge reflecting their structural intricacies, constituent makeup, and processing intricacies. Mastery over density is indispensable for achieving desired material attributes and functionality across diverse application domains.

2.11.1 Effect Of SiC On Sintered Density

The sintered density of composite materials is influenced by various factors, including the SiC content, particle size, and distribution within the matrix. Introducing SiC particles into the powder mixture can alter packing density and sintering behavior, thereby impacting the final density of the sintered composite. Higher concentrations of SiC particles typically lead to decreased packing density in the powder mixture, primarily due to their larger size and irregular shape. This characteristic may impede particle rearrangement and compaction during the sintering process, resulting in a lower sintered density compared to compositions with lower SiC content.

Nevertheless, SiC can enhance densification mechanisms during sintering, particularly at elevated temperatures, by promoting grain boundary diffusion and liquid phase sintering. These mechanisms contribute to improved particle bonding and densification, potentially leading to a higher sintered density. Additionally, the homogeneous dispersion of SiC particles within the matrix can facilitate grain growth and minimize porosity formation during sintering, positively affecting the final density of the composite. The effect of SiC on sintered density is multifaceted, with considerations for factors such as concentration, particle characteristics, and processing conditions. Despite the potential initial decrease in packing density, the densification mechanisms promoted by SiC particles during sintering can ultimately result in a denser composite material.

2.12 WEAR TESTING

The fundamental aim of conducting a wear test lies in evaluating a material's ability to withstand wear and damage under diverse environmental and loading circumstances. Such tests are performed under controlled settings that replicate real-world wear scenarios materials might encounter. These settings encompass fluctuations in load, velocity, temperature, and environmental conditions. An array of methodologies exists for conducting wear tests, including the Pin-on-Disk, Ball-on-Plate, or Block-on-Ring tests. The selection of a particular method hinges on the application's specificity and the type of wear under scrutiny, whether it be abrasive, adhesive, erosive, or fretting wear.

An extensive array of materials, including metals, polymers, ceramics, composites, and coatings, can undergo testing. Material selection is contingent upon the envisaged application, be it automotive components, cutting tools, bearings, or biomedical implants. In this investigation, Distaloy powders, specifically DH, DC1, SA, and AE, mixed with 4.0 wt. % SiC, are employed. The wear test specimens are sintered at 1250 ℃ for 45 minutes in a vacuum furnace, subsequently cooled to room temperature at a rate of 0.1 ℃/s. Parameters such as wear scar diameter, wear rate, weight loss, and surface damage are typically measured during the wear test. These measurements serve to quantify the material's resistance to wear.

Wear tests play a critical role in numerous industries, including automotive, aerospace, manufacturing, and biomedical, where materials face the challenge of enduring wear and friction in crucial components. Employed as a quality control measure, wear tests ensure that materials adhere to specified durability and performance standards. In the realm of research and development, wear tests are instrumental in the creation of novel materials or the enhancement of existing ones to bolster their resistance to wear and prolong their operational lifespan. In essence, wear tests serve as indispensable instruments in materials science and engineering, providing insights into a material's behavior under abrasive or frictional conditions. This aids industries and researchers in making well-founded decisions regarding material selection, product innovation, and quality assurance.

2.12.1 The Pin On Disc Wear Tester

The pin-on-disc wear tester serves as a tool for evaluating the wear characteristics of materials through controlled sliding contact. It comprises a rotating disc and a stationary pin, mimicking real-world contact scenarios. By allowing precise control over parameters like load, speed, and duration, this equipment facilitates the examination of wear behavior under diverse conditions. Through its analysis of wear mechanisms like abrasive, adhesive, and erosive wear, the pin-on-disc wear tester assists in material selection, surface treatment assessment, and lubrication enhancement. Its significance extends across industries such as automotive, aerospace, manufacturing, and materials science, where it contributes to the advancement of wear-resistant materials and components and the figure 2.17 shows the diagram depicts a pin-on-disc wear testing apparatus [45].

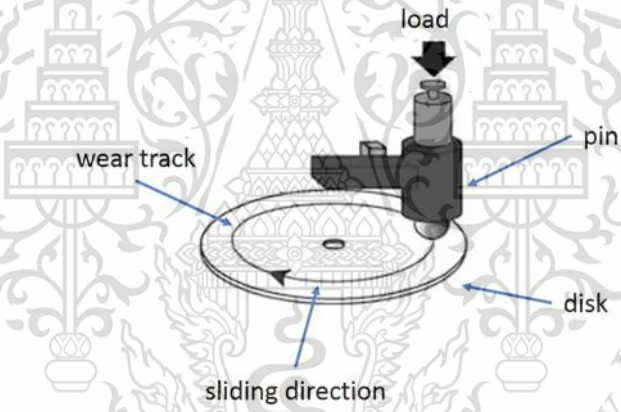

Figure 2. 17 The diagram depicts a pin-on-disc wear testing apparatus [45].

2.12.2 The Coefficient Of Friction (COF)

The coefficient of friction (COF) serves as a valuable indicator of a material's ability to withstand wear and friction, with a higher COF often suggesting heightened friction and potentially increased wear, thereby aiding in the assessment of the material's wear resistance. Utilizing COF data, engineers and researchers can make informed choices regarding material selection, tailoring materials to meet the specific COF requirements of diverse applications like automotive components, cutting tools, or bearings, ensuring reliable performance and longevity. In the development of new materials or the enhancement of existing ones, a comprehensive understanding of the

COF proves essential, enabling the design and engineering of materials better equipped to endure anticipated wear and friction levels within particular applications.

Industries rely on COF measurements to uphold quality standards, ensuring that manufactured products adhere to specified criteria for wear resistance, a practice particularly crucial in safety-sensitive sectors like automotive manufacturing. Exploring lubrication efficiency and various lubricants' efficacy constitutes a significant aspect of COF analysis, where a diminished COF signifies efficient lubrication, leading to friction reduction and wear mitigation, ultimately enhancing component longevity. Tribology, the field encompassing friction, wear, and lubrication studies, places considerable emphasis on COF, with wear tests commonly employed to delve into material tribological characteristics. Typically, the COF exhibits a correlation with a material's wear rate, with an elevation in COF often indicative of accelerated wear, implying a heightened rate of material deterioration.

Utilizing wear tests to gauge the COF allows researchers to emulate real-world scenarios characterized by prevalent friction and wear, aiding in the prediction of materials' performance in practical settings. Leveraging COF data facilitates the optimization of materials and surface treatments aimed at minimizing friction and wear; for instance, implementing coatings or treatments that reduce the COF can enhance a material's wear resistance. In safety-critical domains such as aerospace or medical device manufacturing, comprehending the COF holds paramount importance to guarantee component reliability and longevity, without succumbing to excessive wear. In essence, the coefficient of friction serves as a pivotal parameter in wear testing, furnishing insights into materials' reactions to friction and abrasion, thereby pertinent across diverse industries and research endeavors aimed at ensuring materials and components' performance, endurance, and safety across myriad applications and the figure 2.18 show a common graph illustrating the relationship between the coefficient of friction and time [46].

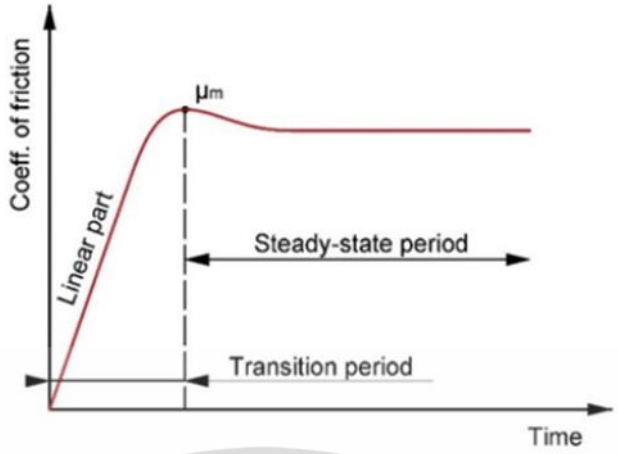

Figure 2. 18 A common graph illustrating the relationship between the coefficient of friction and time [46].

The friction coefficient, typically represented by the symbol μ (mhu), expresses the relationship between the frictional force acting between two surfaces in contact (f) and the normal force exerted on them F_{load}. It serves to quantify the resistance encountered during sliding or relative motion between these surfaces. Variations in the friction coefficient can arise from factors such as surface roughness, inherent material characteristics, the presence of lubricants, and the surrounding environmental conditions. A comprehensive understanding of the friction coefficient and its measurement are indispensable for both anticipating and regulating frictional responses across a spectrum of mechanical systems and operational scenarios. Its significance extends to pivotal aspects such as machinery efficiency, braking system efficacy, and the wear patterns observed in mechanical components. Moreover, the friction coefficient assumes a critical role in dictating the design considerations for materials and surface treatments aimed at achieving specific frictional properties and curtailing energy dissipation.

$$Friction\ Coefficient\ (\mu) = \frac{f}{F_{load}} \qquad (2.2)$$

2.12.3 Wear Rate.

The rate of wear signifies how quickly a material deteriorates or diminishes due to wear, erosion, or other damaging factors. It measures the extent of material loss

within a defined timeframe and under specific conditions. Variations in the wear rate can stem from factors like the nature of the wear mechanism, surface texture, lubrication, and operational surroundings. Grasping and computing the wear rate hold paramount importance in evaluating the effectiveness and endurance of materials, components, and machinery. This comprehension empowers engineers and researchers to anticipate component lifespans, fine-tune maintenance timetables, and devise strategies to mitigate wear-related challenges. Wear rate quantifies the pace or velocity at which a material succumbs to wear, typically gauged by the volume or mass lost per unit of sliding distance, duration, or cycle count. It delineates how rapidly a material wears away due to diverse wear mechanisms such as abrasive wear, adhesive wear, or erosive wear. The wear rate serves as a pivotal metric for appraising the efficacy and robustness of materials, components, and systems subjected to wear. The m^3/m or mm^3/mm is the common unit of wear rate. Familiarity with the wear rate aids in prognosticating component longevity, streamlining maintenance regimes, and selecting materials endowed with suitable wear resistance for particular applications.

2.12.4 Mass Loss

Mass applications ease in the mass of a material caused by wear, corrosion, erosion, or degradation. This measurement determines the quantity of material that has been depleted or shed within a defined timeframe or particular circumstances. Various mechanisms contribute to mass loss, encompassing abrasive wear, adhesive wear, and corrosive wear, among others. Assessing mass loss serves as a pivotal factor in appraising the resilience and operational lifespan of materials, components, and systems affected by wear or deterioration. Grasping and measuring mass loss hold paramount importance for projecting maintenance intervals, gauging the efficacy of protective coatings or surface treatments, and optimizing material choices for specific purposes.

2.12.5 Volume Loss

Volume loss denotes the decrease in material volume caused by factors like wear, corrosion, erosion, or degradation, representing the quantity of material removed

within a defined timeframe or under particular conditions. Various wear mechanisms, such as abrasive wear, adhesive wear, and erosive wear, contribute to volume loss. Evaluating volume loss is pivotal for assessing the longevity and resilience of materials, components, and systems exposed to wear or deterioration. It plays a crucial role in predicting maintenance schedules, appraising the effectiveness of protective coatings or surface treatments, and refining material choices for specific uses. Understanding and quantifying volume loss aids in optimizing performance and durability across diverse applications.

2.13 WEAR MECHANISM

A wear mechanism is the manner in which materials deteriorate or suffer harm when exposed to different mechanical, chemical, or environmental influences while in use. It involves the particular processes or interactions that result in the depletion of material, surface impairment, or alterations in physical characteristics. Among the wear mechanisms are abrasive wear, adhesive wear, corrosive wear, fatigue wear, and erosive wear, among others. Depending on the operating conditions and environmental variables, these mechanisms can operate independently or in conjunction with each other. Appreciating wear mechanisms is crucial for the development of materials, components, and systems capable of enduring and mitigating wear effects, thereby elongating their lifespan and enhancing performance and the figure 2.19 show the general wear mechanisms include adhesive wear, abrasive wear, fatigue wear, and corrosive wear [47].

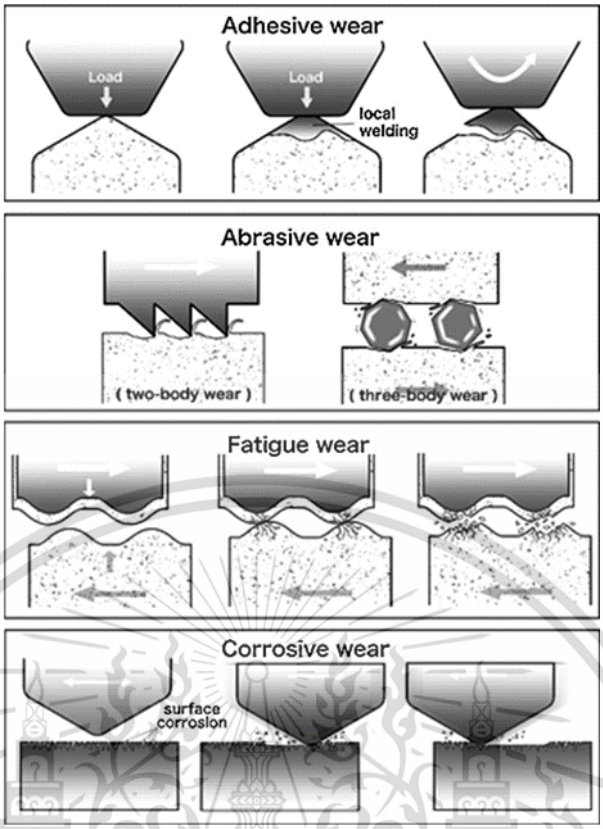

Figure 2. 19 General wear mechanisms include adhesive wear, abrasive wear, fatigue wear, and corrosive wear [47].

2.13.1 Adhesive Wear

Adhesive wear occurs as a consequence of materials suffering damage due to the adhesion and subsequent detachment of material from contacting surfaces, commonly observed in sliding or rubbing applications where two surfaces are pressed together. This type of wear results in the transfer of material from one surface to another, leading to surface damage and potential degradation of component performance. The degree of adhesive wear is influenced by factors such as material properties, surface roughness, contact pressure, and sliding velocity. Measures to mitigate adhesive wear include selecting materials with compatible properties, applying lubricants to reduce friction and adhesion, and employing surface treatments to improve wear resistance. Regular maintenance practices, such as cleaning and inspection, are crucial for early detection and mitigation of adhesive wear to prevent component failure and figure 2.20 shows the adhesive wear mechanism [48].

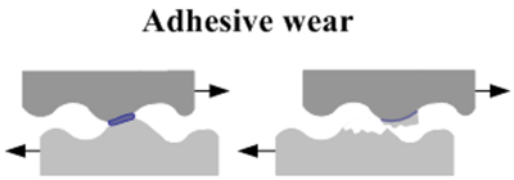

Figure 2. 20 The adhesive wear mechanism schematic [48].

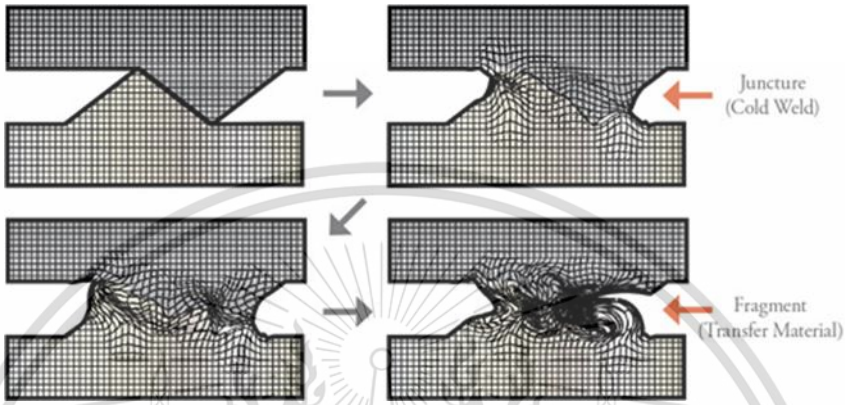

Figure 2. 21 The interaction causing adhesive wear between surfaces [49].

Adhesive wear manifests when materials degrade due to the phenomenon of two surfaces adhering and then separating, causing material transfer between them and the interaction causing adhesive wear between surfaces is shown in figure 2.21 [49]. This wear type is prevalent in direct surface contact scenarios like sliding or rolling components such as gears, bearings, and seals. It leads to wear debris formation and surface damage, impacting the performance and longevity of components. Severity of adhesive wear depends on factors like material composition, applied force, sliding speed, and surface roughness. Strategies to combat adhesive wear encompass material selection based on compatibility, lubrication to minimize friction and adhesion, and application of surface coatings for enhanced resistance. Routine maintenance, encompassing cleaning and inspection, aids in early detection and mitigation of adhesive wear, averting potential equipment breakdowns.

2.13.2 Abrasive Wear

Abrasive wear manifests when materials degrade due to the mechanical interaction between abrasive particles or surfaces sliding against each other. and figure 2.22 shows the abrasive wear mechanism [48]. This form of wear is widespread in

industrial settings where surfaces come into contact, including machinery, tools, and mechanical parts. It causes material removal from the surface, leading to wear and potentially impacting the component's performance and lifespan. The severity of abrasive wear varies based on factors like abrasive particle hardness, size, shape, applied load, and sliding speed. Strategies to mitigate abrasive wear involve selecting materials with high hardness and wear resistance, applying protective coatings or surface treatments for improved durability, and employing lubrication systems to minimize friction and wear. Furthermore, regular maintenance procedures, such as periodic cleaning and inspection of components, aid in detecting signs of abrasive wear and averting premature failure.

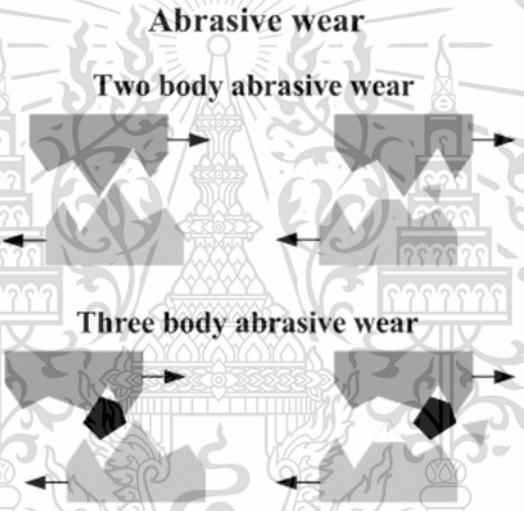

Figure 2. 22 The abrasive wear mechanism schematic [48].

2.13.3 Fatigue/Delamination Wear

Fatigue/delamination wear manifests when materials undergo degradation due to the repetitive application and removal of loads, causing layers to separate or the material to delaminate and figure 2.23 shows the adhesive wear mechanism [48]. This type of wear is frequently observed in components that experience cyclic loading, such as rotating machine elements, bearings, and structural parts. The cyclic stress induces the propagation of microscopic cracks within the material, ultimately leading to the development of delamination layers. The structural integrity of the component can be compromised by fatigue/delamination wear, potentially resulting in catastrophic failure if not addressed promptly. Strategies to mitigate

fatigue/delamination wear encompass the utilization of materials with enhanced fatigue resistance, the application of appropriate surface treatments to bolster fatigue strength, and the design of components featuring smoother surfaces to mitigate stress concentrations. Furthermore, regular inspections and maintenance procedures play a crucial role in identifying early indications of fatigue/delamination wear and averting catastrophic failures.

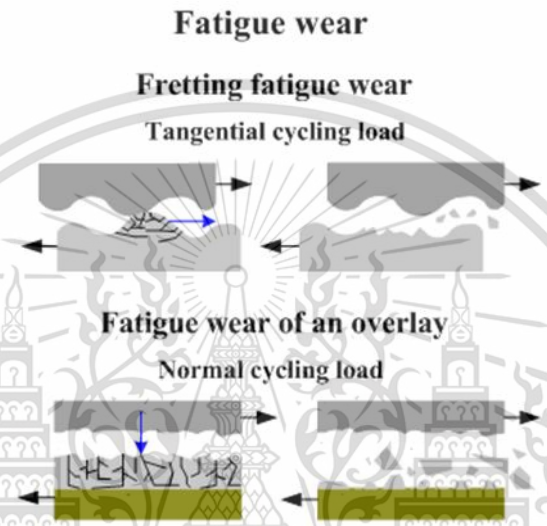

Figure 2. 23 The fatigue wear mechanism schematic [48].

2.13.4 Corrosive/Oxidative Wear

Corrosive/oxidative wear occurs when materials degrade due to both mechanical wear and chemical reactions with corrosive or oxidative substances, commonly found in harsh industrial environments and figure 2.24 shows the corrosive wear mechanism schematic [50]. This type of wear leads to accelerated material loss and surface damage when exposed to corrosive agents or oxidizing agents. Industrial applications prone to corrosive/oxidative wear include machinery, equipment, and components used in marine, chemical processing, and automotive systems. Figure 2.26 shows the surface damage due to the corrosion and oxidation wear [52]. The mechanisms underlying this wear involve the formation of corrosion products and oxides on the material's surface, weakening it and making it susceptible to mechanical abrasion and erosion and the figure 2.25 shows the example of copper surface experiencing oxidative wear [51]. Preventive strategies against corrosive/oxidative wear

encompass choosing corrosion-resistant materials, applying protective coatings, and adhering to proper lubrication and maintenance protocols.

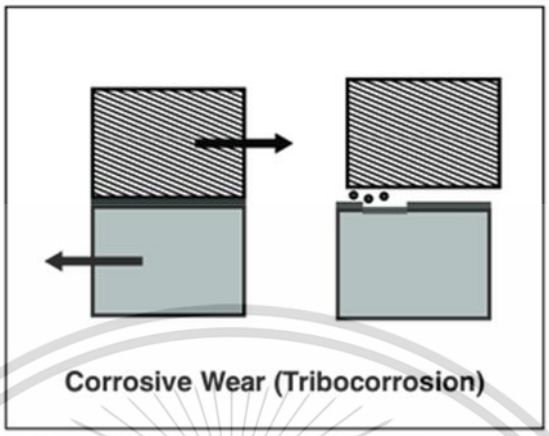

Figure 2. 24 The corrosive wear mechanism schematic [50].

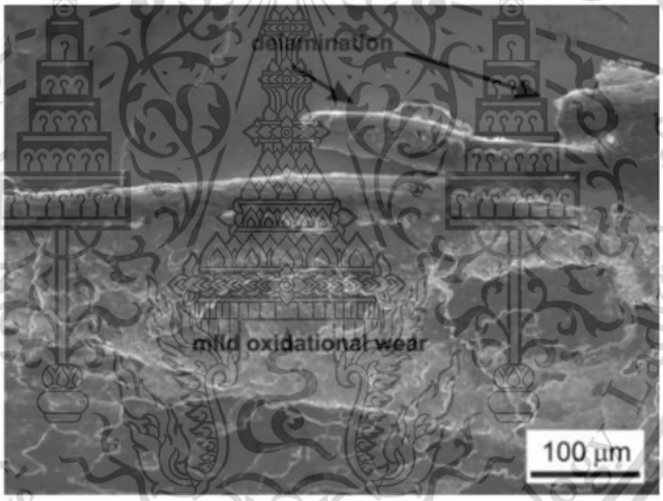

Figure 2. 25 Copper surface experiencing oxidative wear [51].

Figure 2. 26 The surface damage due to the corrosion and oxidation wear [52].

CHAPTER 3

RESEARCH METHODOLOGY

3.1 EXPERIMENTAL PROCEDURE

The following Figure 3.1 shows the experimental procedure for the sintered Distaloy DH (1.47Mo-2.0Cu), Distaloy DC1 (1.50Mo-2.0Ni), SA (0.50Mo-1.50Cu-1.75Ni) and AE (0.50Mo-1.50Cu-4.00Ni) with 4 wt.% percent weight of silicon carbide SiC.

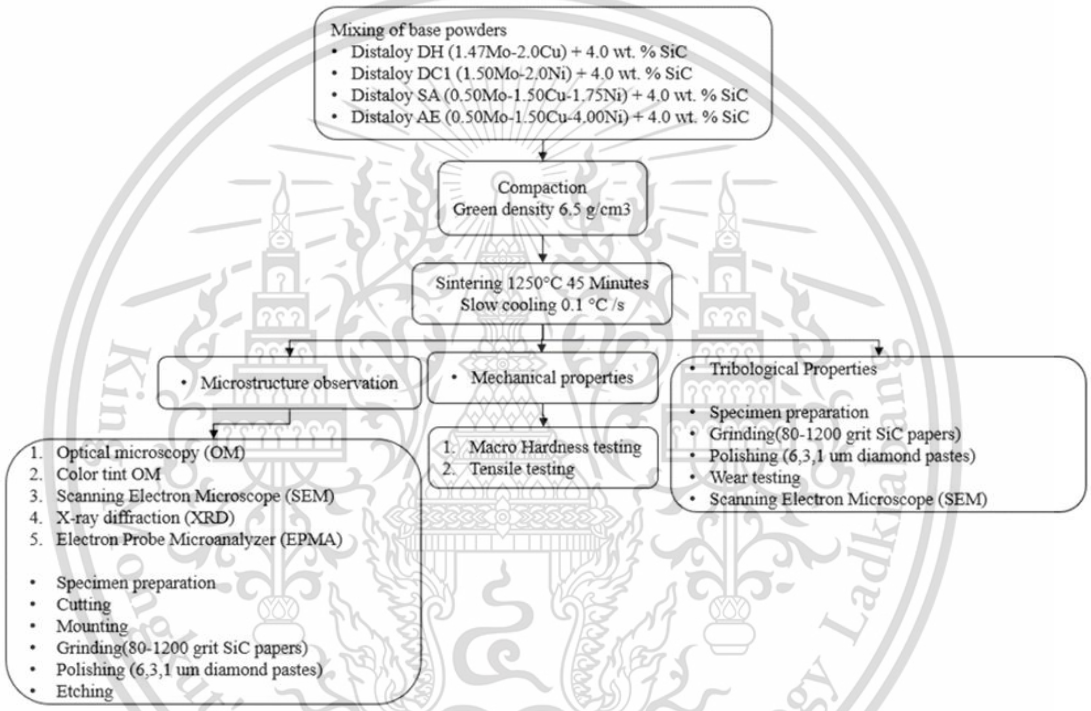

Figure 3. 1 Experimental procedure

3.2 MATERIALS PREPARATION

3.2.1 Diffusion-Bonded Powders

Figure 3.2 illustrates diffusion-bonded powders, namely Distaloy DH, Distaloy DC1, Distaloy SA, and Distaloy AE. Distaloy DH, denoted as Direct Hardening (DH), is a low-alloyed powder known for its exceptional hardenability. Distaloy DC1, designated as Dimensional Control (DC), is a specially formulated low-alloyed powder engineered to achieve stable dimensional changes regardless of density and to exhibit high strength after sintering. Distaloy SA originates from the sponge iron grade SC100.26,

further enhanced by diffusion bonding with 1.75% Ni, 1.5% Cu, and 0.5% Mo. Meanwhile, Distaloy AE shares the same powder base as Distaloy AB but features an increased Ni content of 4%, with Cu and Mo contents at 1.5% and 0.5%, respectively. These diffusion-bonded powders are obtainable from Hoganas, Sweden.

With additional copper enhancement, Distaloy DH demonstrates superior hardenability compared to Astaloy Mo, rendering it suitable for sinter hardening and various heat treatment processes. Incorporating graphite can yield a tensile strength of 700 MPa post a single pressing and sintering process. Distaloy DH is produced by diffusion bonding 2% Cu to Astaloy Mo, pre-alloyed with 1.5% Mo, ensuring good compressibility and minimal dimensional scattering.

Similarly, for Distaloy DC1, the introduction of graphite results in a tensile strength of 700 MPa after a single pressing and sintering process. Formulated through the diffusion bonding of 2% Ni to Astaloy Mo, pre-alloyed with 1.5% Mo, this dual-alloying approach ensures favorable compressibility and minimal dimensional variation.

Distaloy SA is suitable for densities up to 6.9 g/cm^3 following a single pressing, and with graphite inclusion, a sintered tensile strength of 600 MPa is typically attainable. Distaloy SA also boasts high green strength.

Regarding Distaloy AE, with Cu and Mo contents at 1.5% and 0.5%, respectively, its high Ni content and good compressibility facilitate the production of materials with a sintered tensile strength typically reaching 750 MPa. Distaloy AE demonstrates commendable hardenability and dimensional stability.

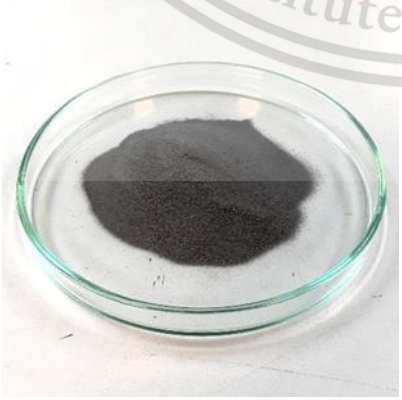

Distaloy DH powder

Distaloy DC1 powder

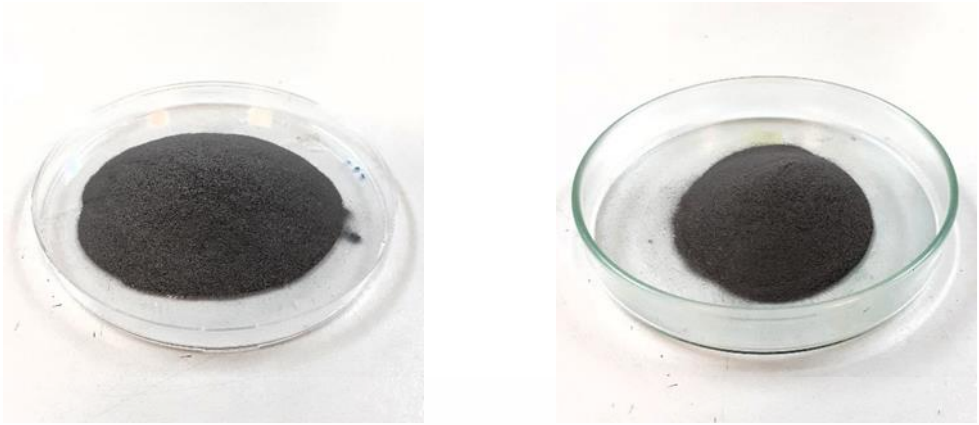

Distaloy SA powder Distaloy AE powder

Figure 3. 2 Diffusion bonded powders

3.2.2 Silicon Carbide (SiC) Powder

Displayed in figure 3.3 is silicon carbide powder (SiC), a commonly utilized reinforcing phases in diffusion-bonded powders due to its elevated strength and chemical stability, particularly in challenging environments. Additionally, SiC is employed to diminish the friction coefficient and mechanical interactions between surfaces in relative motion. These SiC powders can be obtained from Sigma-Aldrich in the USA, characterized by their hexagonal phase and a particle size of -400 mesh. The density of SiC at 25 °C (lit.) is 3.22 g/mL, and it has a molecular weight of 40.10.

Figure 3. 3 Silicon carbide powder

3.2.3 Zinc Stearate Powder.

Figure 3.4 illustrates zinc stearate powder, an additive incorporated as a lubricant or binding agent in the mixing stage of iron powder or other metallic-based

composites before compaction. This addition enhances blending properties, improves the flow with powdered metal, and ensures consistent porosity for the fabrication of Distaloy powders mixed with silicon carbide powders. Furthermore, it plays a crucial role in preventing the parts from adhering to the mold during the compaction process, resulting in a superior finish.

Figure 3. 4 Zinc stearate powder

3.2.4 Argon gas

Figure 3.5 illustrates the argon gas and application of argon gas, which is employed to safeguard sintered parts from chemical oxidation on their surfaces. Utilized in both the pre- and post-sintering stages, argon gas serves to eliminate oxygen from the air.

Figure 3. 5 Cylinders of argon gas

3.2.5 Etchants

Depicted in Figure 3.6 is the nital etchant, specifically nital 2% in ethanol as shown in Figure 3.7 and, employed for etching in optical microscopy (OM) and scanning electron microscopy (SEM) of the sintered composites. Nital etchant, a combination of nitric acid and alcohol, is commonly utilized for etching low carbon steels to reveal the metal's microstructure through selective chemical attack. This etchant has the ability to preferentially attack high-energy sites, such as boundaries and defects. Additionally, Figure 3.8 and Figure 3.9 showcase Picral and N2S2O5 etchants, which are utilized for etching in color-tinted optical microscopy (OM).

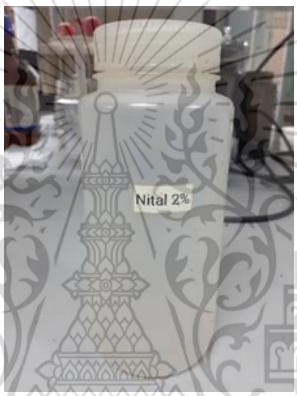

Figure 3. 6 The 2 % Nital etchant

Figure 3. 7 AR1069-G2.5L Ethanol

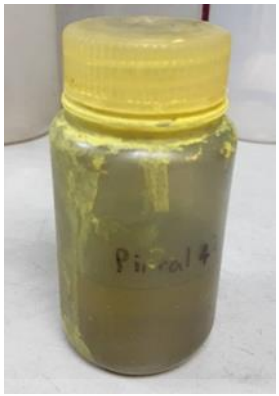

Figure 3. 8 Picral etchant

Figure 3. 9 N2S2O5 etchants

3.3 EXPERIMENTAL EQUIPMENT

3.3.1 The Analytical Digital Balance

The analytical digital balance is shown in Figure 3.10. The analytical digital balance 4-digit, utilized for lab weighing and wear analysis of tribological properties, is characterized by high levels of precision, strong environmental adaptability, and readability at 0.0001g.

Figure 3. 10 The 4-digit analytical digital balance

3.3.2 The Digital Balance

Utilized for laboratory weighing and density calculation, the Laboratory Digital balance 3-digit, as depicted in Figure 3.11, is characterized by high levels of accuracy and precision in analytical testing.

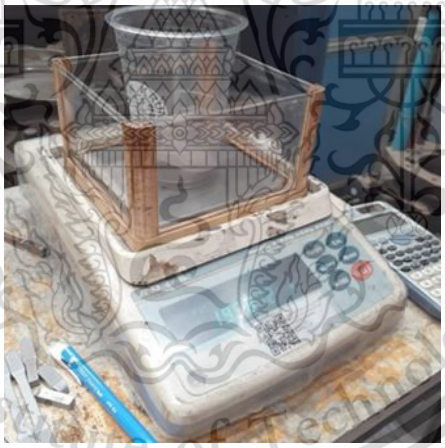

Figure 3. 11 The 3-digit digital balance

3.3.3 Power Blending Machine

Figure 3.12 illustrates the use of a powder blender, which is employed for the mixing of metal and additive powders in various area types. This blending process is executed by utilizing a rotating powder bottle operating at the revolution per minute as desired. In this study used around 1 hour for each rotating powders bottles.

Figure 3. 12 Powder blending machine

3.3.4 Hydraulic Pressing Machine

Figure 3.13 displays a hydraulic pressing machine with a 100-ton load, employed for compacting mixed powder into green tensile test bars and coin shape specimens with varying shapes depending on the die and mold. This process is accomplished through the application of the pressure of hydraulic.

Figure 3. 13 Hydraulic pressing machine

3.3.5 High Vacuum Sintering Furnace

Figure 3.14 showcases a high vacuum sintering furnace provided by SCHMETZ D59708 MENDEN, utilized for sintering specimens under a vacuum atmosphere. Following the sintering process, the specimen transforms into a green density material. In the microstructure, the sintering process significantly influences the grain size, pore

size, grain boundary shape, and distribution, thereby impacting the properties of the material.

Figure 3. 14 SCHMETZ D59708 MENDEN High vacuum sintering furnace

3.3.6 High Precision Cutting Machine.

Figure 3.15 illustrates the utilization of the Discotom-5 cutting machine, a high-precision cutting machine employed for shaping materials into specific forms to prepare specimens for characterization for the microstructure of the specimens.

Figure 3. 15 High precision cutting machine.

3.3.7 Hot Mounting Pressing Machine.

Figure 3.16 displays the hot mounting press, which is employed to prepare samples before the grinding and polishing stages. Mounting is carried out with the

objective of managing irregularly shaped or small-sized specimens, safeguarding coatings, or thin layers, ensuring excellent edge retention, and handling fragile materials during the preparation process. In using a hot mounting pressing machine, the hot mounting process involves mounting the specimen under both heat and pressure.

Figure 3. 16 Hot mounting pressing machine.

3.3.8 Grinding And Polishing Of Metallurgical Machine

Figure 3.17 features the Labopol-5 machine, a metallurgical grinding and polishing machine employed in the sample preparation process. The primary objective is to achieve a superior surface finish characterized by no scratches, no deformation, and a highly reflective sample surface, facilitated by the machine's reliable rotational speed.

Figure 3. 17 Grinding and polishing of metallurgical machine.

3.3.9 The Papers Of Silicon Carbide

Figure 3.18 depicts the utilization of silicon carbide paper (SiC paper) with grit sizes ranging from 80 to 4000, employed for the grinding of metallic specimens. This process aims to eliminate damaged surface layers and achieve a smooth, flat, and scratch-free surface for characterization of microstructure.

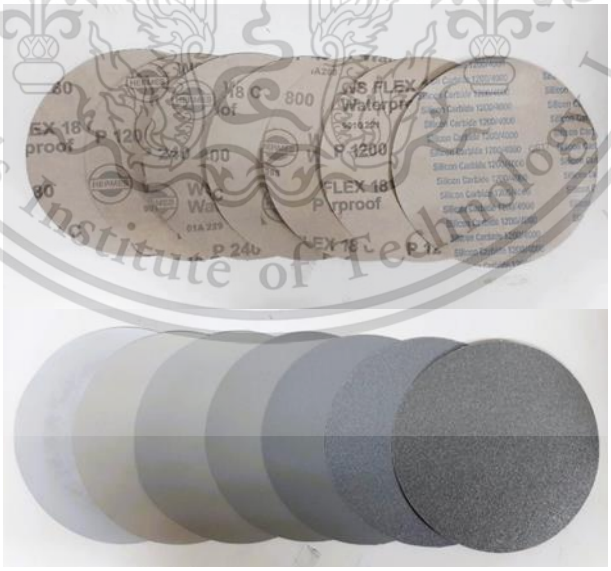

Figure 3. 18 The papers of silicon carbide (80-1200 grit SiC papers)

3.3.10 Polishing Micron Clothes

Figure 3.19 displays the application of micron polishing cloth, utilized subsequent to the grinding step to eliminate scratches generated during grinding. The purpose of the polishing step in specimen preparation is to achieve a smooth and reflective surface by removing the final thin layer of metal's deforming.

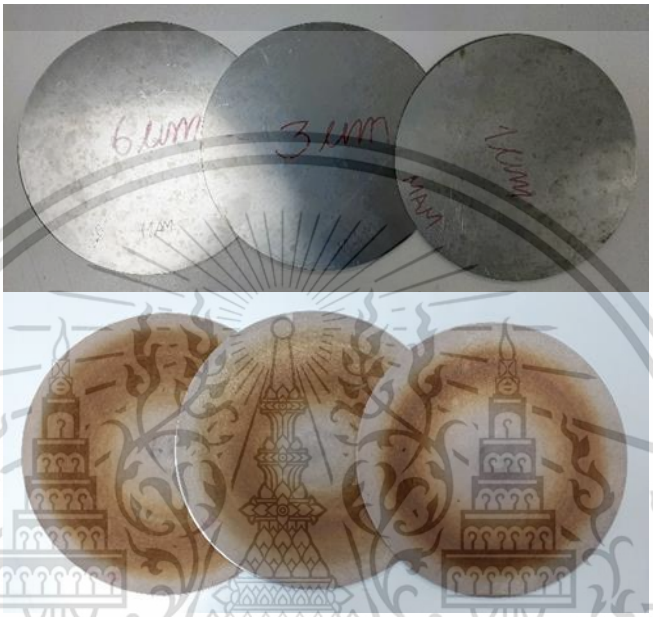

Figure 3. 19 Polishing micron clothes (6,3,1µm)

3.3.11 The Diamond Suspensions (6, 3 and 1 µm)

Figure 3.20 illustrates the diamond suspension in sizes 6, 3, and 1 µm, employed in the sample preparation process alongside polishing cloth to achieve rapid removal and generate a flawlessly polished surface, rendering it ready for analysis. The choice of diamond suspension type is contingent upon the desired surface finish and the type of material being processed.

Figure 3. 20 The diamond suspensions (6, 3 and 1 μm)

3.4 THE INSTRUMENTS OF CHARACTERIZATION

3.4.1 Digital Vernier Caliper

Figure 3.21 shows a digital vernier caliper, a precision instrument used for measuring both the external and internal dimensions of an object, presenting the numeric values for the measurements.

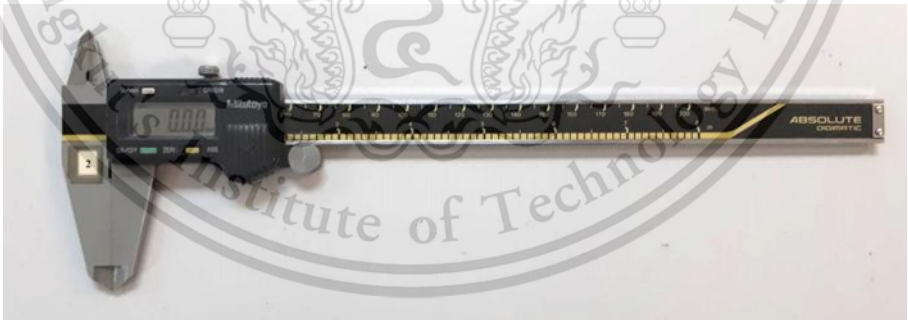

Figure 3. 21 Digital vernier caliper

3.4.2 Optical Microscope Machines.

Figure 3.22 features an Olympus STM7 Optical Microscope from Japan, which falls under the category of microscopes utilizing visible light and a lens system to magnify images, particularly small samples like the microstructure of specimens in this study. Optical microscopes, such as this one, are widely employed and straightforward

to develop, benefiting from the use of visible light, allowing direct observation of samples with the eye of the human.

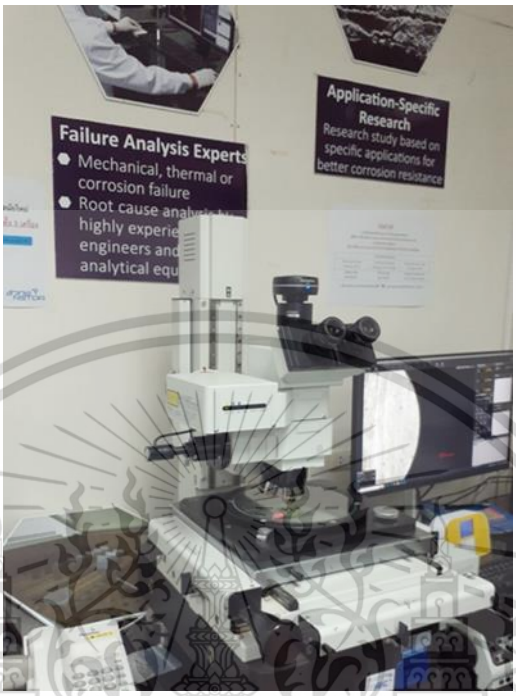

Figure 3. 22 The Olympus STM7, Optical microscope machine, Japan

3.4.3 Scanning Electron Microscope Machine

Figure 3.23 displays the utilization of a Hitachi SU8230 Scanning Electron Microscope (SEM) from Japan for the examination of wear debris, worn surfaces, counter ball surfaces and the specimens at the micro-scale. Scanning of SEM involves directing a focused electron beam over a surface to create an image, with the interaction between the focused electron beam and the sample producing secondary electrons, backscattered electrons, and characteristic X-rays. The detectors collect these signals, generating images displayed on the screen of the computer.

Figure 3. 23 The Hitachi SU8230, Scanning electron microscope machine, Japan.

3.4.4 The X-Ray Diffraction Analysis Machine

Figure 3.24 features X-ray diffraction analysis (XRD), employed for identifying the crystal phase and orientation, as well as revealing information about the chemical composition within a specimen. The identification of phases is accomplished through the comparison of acquired data with reference databases.

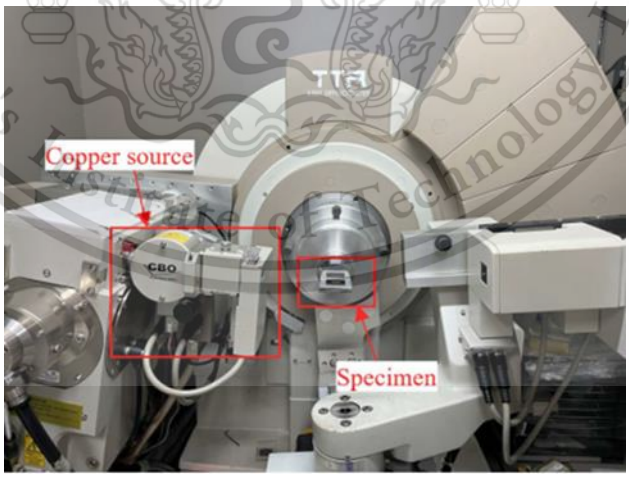

Figure 3. 24 The X-Ray diffraction analysis machine

3.4.5 The Testing Machine Of Macro Hardness

As displayed in figure 3.25, the Instron-930 macro hardness testing machine is utilized for measuring the hardness of macrostructures through conventional Rockwell hardness testing. Equipped with a high-precision tester, it ensures quick and direct results in the Rockwell test, eliminating the need for a secondary dimensional measurement requirement and reducing the potential for error of the human.

Figure 3. 25 The testing machine of macro hardness, Instron-930

3.4.6 The Instron 8801 Universal Testing Machine

Figure 3.26 illustrates the use of an Instron 8801 universal instrument, a universal testing machine employed to assess the tensile properties of materials in this research study. The testing equipment is capable of defining material properties, including strain hardening, plastic deformation, tensile strength, elasticity and yield strength of the specimens.

Figure 3. 26 The universal testing machine, Instron 8801

3.4.7 The Testing Machine Of Pin-On-Disc

Figure 3.27 displays the Pin-on-disc testing machine, conducted in accordance with ASTM G99, utilized to assess friction and wear characteristics in contacts of the sliding. This involves sliding between a rotating disc and a stationary pin, with the ability to vary wear track diameter and normal load. Electronic sensors are employed to monitor tangential frictional force and wear during the testing process.

Figure 3. 27 The ASTM G99testing machine of pin-on-disc

3.5 EXPERIMENTAL PROCEDURE

3.5.1 The Powders Mixing.

Table 3.1 provides the chemical composition of the mixed powder. Experimental sintered composites were created using four distinct Distaloy powders - namely, Distaloy DH, Distaloy DC1, Distaloy SA, and Distaloy AE. These sintered composites, prepared as reference materials, were mixed with a fixed 4 wt.% of silicon carbide powder. The mixing process involved combining the powders with 1 wt.% of Zinc stearate in a powder mixer operating at a speed of 6.5 RPM for around one hour duration.

Table 3.1 The nominal composition of experimental sintered composites.

Sintered composite	Base metal powder	SiC (wt.%)	Nominal composition (wt. %)					
			C	Si	Mo	Cu	Ni	Fe
DH	Distaloy DH	4.0	1.20	2.80	1.41	1.92	-	Bal.
DC1	Distaloy DC1	4.0	1.20	2.80	1.44	-	1.92	Bal.
SA	Distaloy SA	4.0	1.20	2.80	0.48	1.44	1.68	Bal.
AE	Distaloy AE	4.0	1.20	2.80	0.48	1.44	3.84	Bal.

3.5.2 Compaction

Figure 3.28 shows the standard tensile test bars, adhering to MPIF standard 10 and ASTM B783 having 6.5 ± 0.01 g/cm^3 of green density. They were crafted from mixed Distaloy powders using a 100-ton hydraulic pressing machine. For the tribological test, coin-shape specimens were prepared under conditions identical to those of the tensile test bars, and the dimensions of the coin-shape specimen are presented in Figure 3.29. To minimize the impact of back pressure, each specimen was maintained about 10 seconds in a die underneath the pressure.

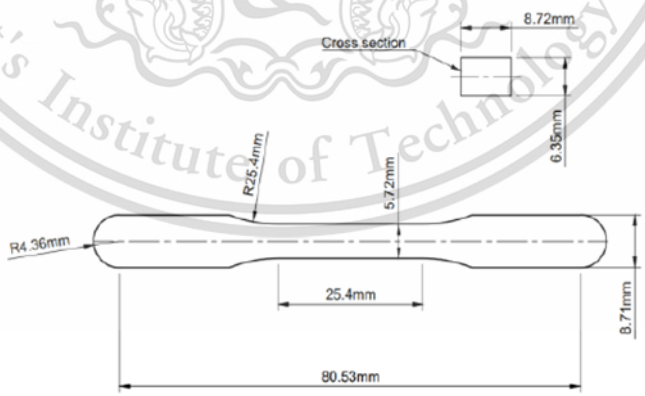

Figure 3. 28 The MPIF standard 10, ASTM B783 standard tensile test bar

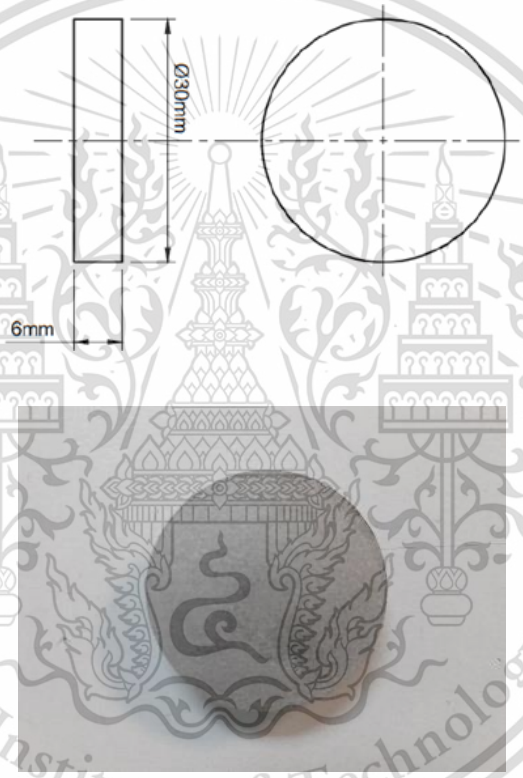

Figure 3. 29 The standard dimensions of coin-shaped specimen

3.5.3 Sintering

Comprising the green compacts with both standard tensile test bars and coin-shape specimens, underwent sintering in sintering furnace with a high vacuum due to its capability of achieving high temperatures while oxidization is minimizing. Figure 3.30 illustrates the sintering process, outlined in three stages under a vacuum atmosphere, commenced with the first stage heating up to 600°C for 60 minutes to reach the de-waxing temperature. This stage aimed to remove lubricants, binders, and other organic

materials from the specimen, enhancing the integrity of compacts for the process of the subsequent sintering. The following stage involved heating up to 1250°C, maintaining this temperature for 45 minutes to ensure phase stability (homogenization) of the material, transforming the entire specimen into the austenite phase. The final step of sintering involved a slowly gradual cooling process with 0.1 °C per second within the furnace.

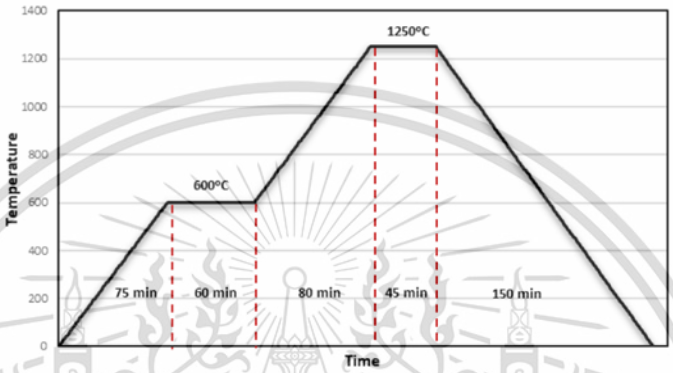

Figure 3. 30 The sintering profile of all sintered composites specimens

3.5.4 Microstructure Analysis

For observing the microstructure of specimens, optical microscopy and scanning electron microscopy serve as the tools. While optical microscopy is prevalently employed for general investigation ambitions, scanning electron microscopy offers more detailed insights into surface characteristics and composition. Consequently, this study utilizes optical microscopy to analyze the overall microstructure with optical microscope (Olympus STM7) machine and employs scanning electron microscopy for a detailed examination of microstructural features with scanning electron microscope (Hitachi SU8230) machine.

3.5.5 X-Ray Diffraction Analysis

Utilized for identifying crystalline phases and orientation within a material, X-Ray Diffraction Analysis (XRD) is employed in this study. The preparation of all XRD specimens involved cutting, grinding, and polishing and the analysis was conducted using Rigaku TTRAX III X-ray diffractometer with copper source. The conditions were

wavelength of 1.54 Å, conditions of step size of 0.2°, time 0.5 s/step and angle of 30-100°.

3.5.6 Mechanical Properties Test

3.5.6.1 Surface Preparation

All specimens underwent surface preparation, starting with grinding on silicon carbide paper ranging from 80 to 4000 grits, followed by polishing using diamond suspensions of 6, 3, and 1 µm. Subsequently, the polished surfaces were etched with a 2% Nital solution, and ethanol was employed to clean the surfaces before investigation.

3.5.6.2 Macro Hardness Test

In the assessment of macro-hardness, two specimens from each condition of sintered tensile test bar underwent hardness testing through the Rockwell hardness testing method, in accordance with ASTM E-18. By averaging measurements obtained from six different areas on each specimen the mean hardness value was determined. The Rockwell scale employed was HRB and the hardness measurement utilized a ball indenter with a 1/4-inch diameter.

3.5.6.3 Tensile Test

The Universal Testing Machine, specifically the Instron 8801, was employed to conduct tests on five sintered tensile test bar specimens for each condition of sintered Distaloy composites following ASTM E-8 guidelines. During the testing procedure, the specimens were placed in the machine, and a gradual extension ensued until the fracture happened.

3.5.7 Wear Test (Tribological Properties)

Conforming to ASTM G99-05(2010) and illustrated in figure 3.31, dry sliding wear experiments were conducted using a ball-on-disc wear machine. The experiments

involved sliding velocities of 0.1 m/s under normal load of 15N. All sintered Distaloy composites specimens were subjected to a sliding distance of 1,000 m at room temperature with a relative humidity of the test room. The tribometer test utilized disk specimens with a roughness of 4-5 μm, paired with a 6 mm diameter SKF chromium steel grade G20 ball with a hardness of 838 ± 21 HV and the counterpart material with a roughness of 4 μm.

The coefficient of friction COF graph was generated from the investigated friction torque using a load cell. The coefficient of friction was calculated by using Equation 3.1. From comparing the mass of specimens before and after the wear test, the average volume loss was determined. By using Equation 3.2, the volume loss of coin disk specimens was calculated where R represents the radius of wear track and d represents the width of wear track. Average volume loss of coin disk specimens was calculated from three sintered Distaloy composites specimens. Similarly, the volume loss of spherical-ended pin steel balls was calculated with Equation 3.3, where r is the pin end radius and d is the wear scar diameter. Average volume loss of pin steel balls was calculated from three sintered Distaloy composites specimens. According to equation 3.4 and by following each test, the wear rate was computed. Specific wear rate was calculated by dividing the wear rate into the normal load 15N as specified as equation 3.5. Average specific wear rate of coin disk specimens and pin steel balls were calculated from three sintered Distaloy composites specimens.

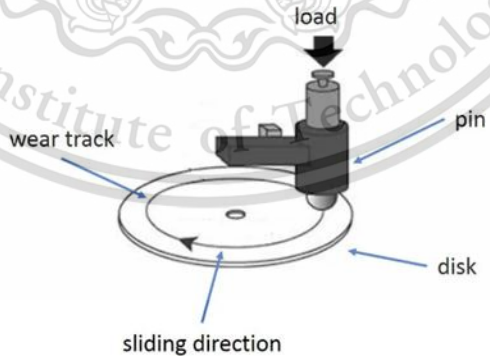

Figure 3. 31 The demonstration of pin steel ball-on-coin disk specimen wear test [45].

The testing conditions of wear test are as the following:

Normal load = 15N

Environment = air

Sliding velocity (m/s) = 0.1 m/s

Sliding distance (m) = 1,000 m

Revolution (RPM) = 160

Pin ball material = chromium steel ball (SKF)

Temperature (°C) = according to test room temperature

Relative humidity (%) = according to test room's relative humidity

The equations which were used for the wear test are as the following:

Coefficient of friction (μ),

$$Coefficient\ of\ friction\ (\mu) = \frac{frictionforce}{load\ test\ (15N)} \quad (3.1)$$

Volume loss of coin disk specimens (mm^3),

$$Coin\ disk\ volume\ loss = 2\pi R\ [r^2 \sin^{-1}\left(\frac{d}{2r}\right) - \left(\frac{d}{4}\right)(4r^2 - d^2)^{\frac{1}{2}}] \quad (3.2)$$

Where, r = pin end radius

R = wear track radius

d = wear track width

(Assuming no significant pin wear)

Volume loss of pin steel balls (mm^3),

$$Pin\ volume\ loss = \left(\frac{\pi h}{6}\right)\left[\frac{3d^2}{4} + h^2\right] \quad (3.3)$$

Where, h (mm)= $r - [r^2 - d^2/4]^{1/2}$

r = pin end radius

d = wear scar diameter

Pin ball diameter = 6 mm

Pin end radius = 3 mm

(Assuming no significant disk wear)

Wear rate of coin disk specimens and pin steel balls,

$$Wear\ rate = \left(\frac{volume\ loss}{distance}\right) \quad \textbf{(3.4)}$$

$$Specific\ wear\ rate = \left(\frac{wear\ rate}{load\ test\ (15N)}\right) \quad \textbf{(3.5)}$$

To gain insight into the impact of processing on wear behavior and the wear mechanism, worn surfaces and wear debris of the sintered Distaloy composites specimens were examined using a Scanning Electron Microscope SEM at the conclusion of each test.

CHAPTER 4

RESULTS AND DISCUSSIONS

4.1 SINTERED DENSITY OF THE SINTERED DISTALOY COMPOSITES

The specimens of this study have green density of 6.5 g/cm^3 respectively. Figure 4.1 shows the average sintered density of all tensile test bars after sintering at the assimilating condition which was performed at 1250°C with 45 minutes and slow cooling in the furnace. The sintered densities of Distaloy DH, Distaloy DC1, Distaloy SA and Distaloy AE with 4.0 wt. % SiC composites are 7.51, 7.47, 6.89 and 7.33 respectively. Figure 4.2 shows the average sintered densities of coin specimens. The results show that the average sintered densities of coin specimens of sintered composites are 7.55, 7.28, 6.63 and 6.62 respectively. It showed that the tensile test bars have slightly higher densities values than the coin specimens. It is because of a little difference of hydraulic pressure (120-125 bar) of hydraulic pressing machine during the compacting process.

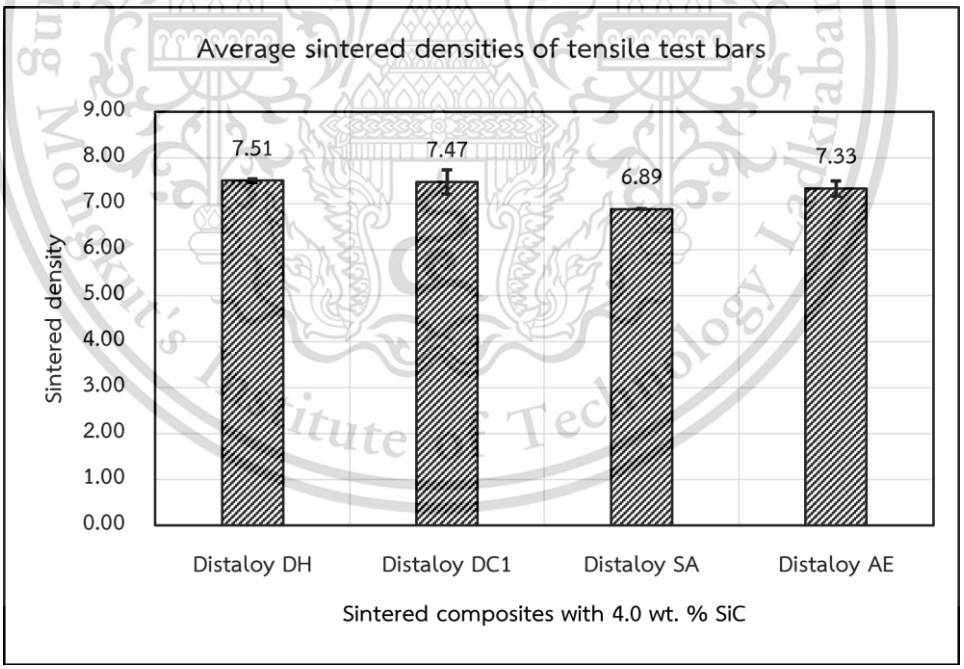

Figure 4. 1 Average densities of sintered Distaloy composites tensile test bars mixed with 4.0 wt. % SiC.

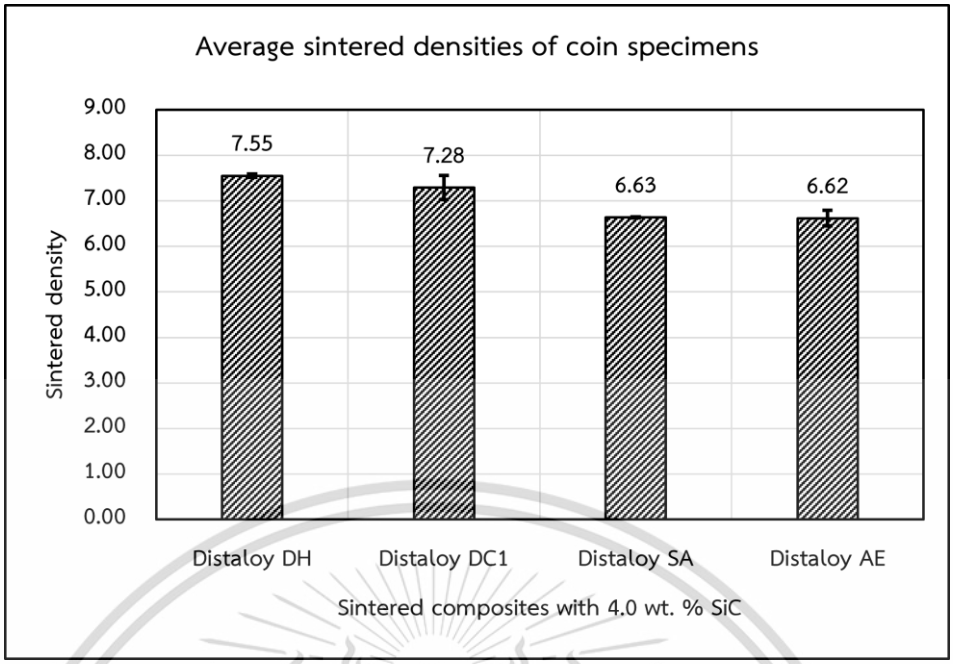

Figure 4. 2 Average densities of sintered Distaloy composites coin specimens mixed with 4.0 wt. % SiC

4.2 MICROSTRUCTURE OF THE SINTERED DISTALOY COMPOSITES

4.2.1 Optical Micrographs Of The Sintered Distaloy Composites

4.2.1.1 Distaloy DH (1.47Mo-2.0Cu) + 4.0 wt. % SiC

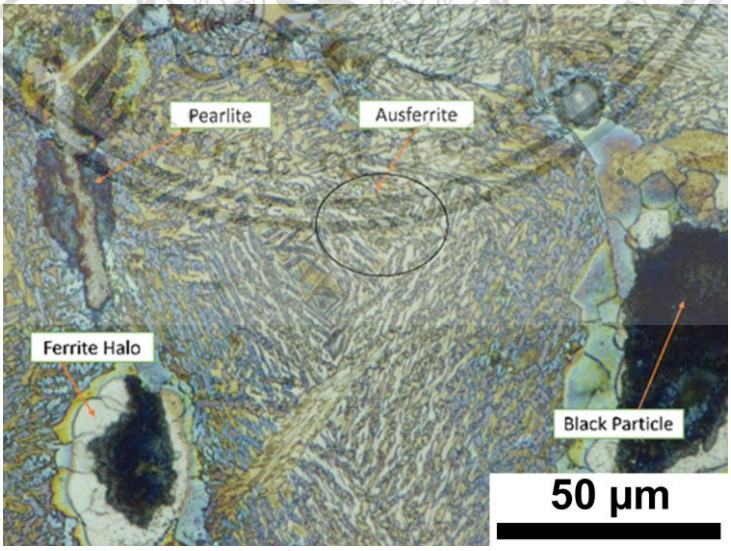

Figure 4. 3 Optical micrograph of sintered Distaloy DH (1.47Mo-2.0Cu) + 4.0 wt. % SiC

The result of optical micrograph of sintered Distaloy DH (1.47Mo-2.0Cu) + 4.0 wt. % SiC is shown in figure 4.3. The findings indicated that the microstructure consisted of black pearlite, ferrite halo, ausferrite, and pearlite. Ausferrite was characterized by the presence of white bainitic ferrite plates and brown austenite plates. Additionally, pearlite formation involved the combination of ferrite and cementite, where cementite represented carbides like M_3C. This dual-phase lamellar microstructure was identified as a strategy to overcome the strength-ductility trade-off dilemma.

4.2.1.2 Distaloy DC1 (1.50Mo-2.0Ni) + 4.0 wt. % SiC

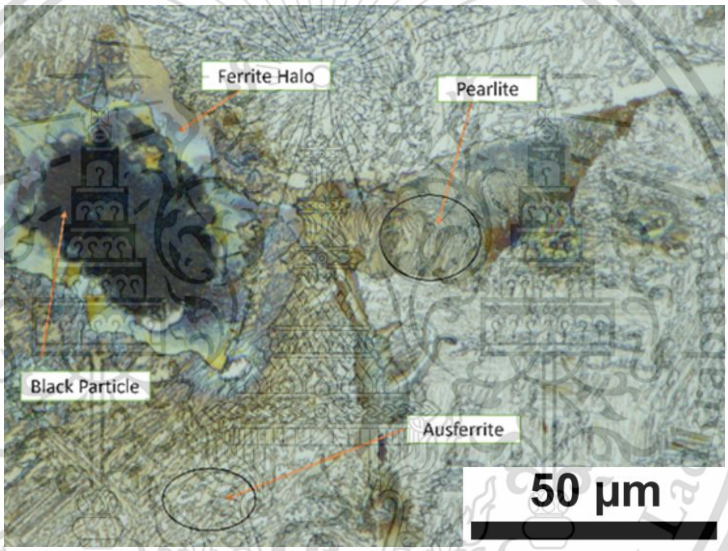

Figure 4. 4 Optical micrograph of sintered Distaloy DC1 (1.50Mo-2.0Ni) + 4.0 wt. % SiC

The result of optical micrograph of sintered Distaloy DC1 (1.50Mo-2.0Ni) + 4.0 wt. % SiC is shown in figure 4.4. The findings revealed that in sintered Fe-0.85Mo + 4.0 wt.% SiC alloy [54], sintered Fe + 5.0% SiC alloy [53], and sintered Distaloy DH and Distaloy DC1 steels, the ferrite halo formed through stable eutectoid transformation, while pearlite formation occurred via metastable eutectoid transformation, resembling mechanisms observed in as-cast ferritic-pearlitic ductile irons [55]. However, the emergence of ausferrite as a predominant microstructural constituent in sintered Distaloy DH and Distaloy DC1 steels under slow and continuous cooling represents a novel phenomenon.

The formation of ausferrite is highly contingent upon the stability of austenite due to two primary factors. Firstly, the stability of the austenite plate, a component of ausferrite, remains intact at room temperature. Secondly, typical ausferrite in an austempered ductile iron forms during isothermal heat treatment within the temperature range lying between pearlite and martensite transformation temperatures, approximately around 300-450 ℃ [56]. The stability of austenite, as evidenced by the presence of ausferrite, is attributed to the combined effect of alloying elements Mo, Si, and C in sintered Fe-Mo-Mn-Si-C composites [57].

Furthermore, the inclusion of Cu, acting as an austenite stabilizer, in sintered Distaloy DH steel, or Ni, also serving as an austenite stabilizer, in sintered Distaloy DC1 steel, would bolster the stability of austenite. Consequently, ausferrite emerges as the predominant microstructural component in the matrices of both sintered Distaloy DH and Distaloy DC1 steels.

4.2.1.3 Distaloy SA (0.50Mo-1.50Cu-1.75Ni) + 4.0 wt. % SiC

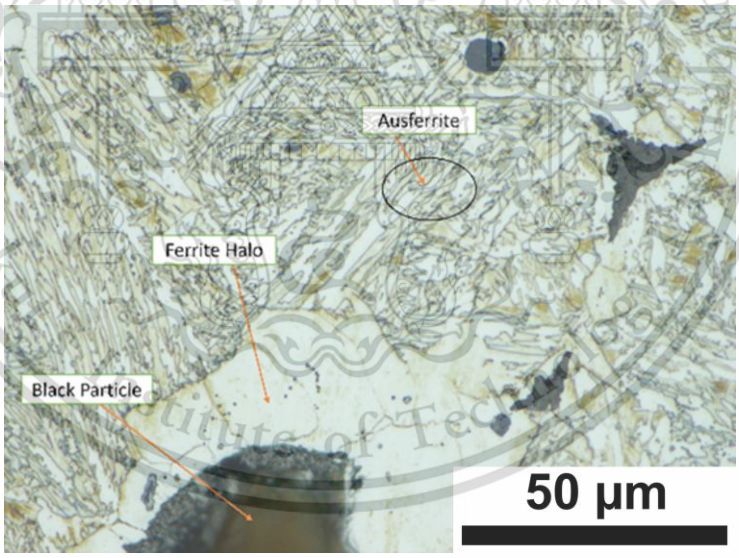

Figure 4. 5 Optical micrograph of sintered Distaloy SA (0.50Mo-1.50Cu-1.75Ni) + 4.0 wt. % SiC

The result of optical micrograph of sintered Distaloy SA (0.50Mo-1.50Cu-1.75Ni) + 4.0 wt. % SiC is shown in figure 4.5. The findings revealed a dual-phase ADI (Austempered Ductile Iron) [58] microstructure in the sintered Distaloy SA steel, characterized by the presence of a black particle embedded within a matrix consisting

of bainitic ferrite and martensite plates, which effectively suppresses stable and metastable eutectoid transformations. Austempered Ductile Iron (ADI) is a form of ductile iron subjected to a specialized heat treatment known as austempering. During this process, the iron is heated to a temperature within the austenite phase range and then rapidly cooled in a controlled bath at a specific temperature, leading to the formation of a distinctive microstructure. This microstructure comprises acicular ferrite and high carbon austenite, contributing to its remarkable mechanical characteristics, including exceptional strength, toughness, and resistance to wear. ADI is extensively utilized across diverse industries, such as automotive, machinery, and construction, where these properties are highly sought after. The coexistence of bainitic ferrite and martensite constituents in the sintered Distaloy SA steel signifies robust austenite stability, primarily attributed to the high Ni content of 4.0 wt. %, resulting in low temperature bainitic and martensitic phase transformations. This microstructural feature resembles that commonly observed in high-carbon steels subjected to low-temperature isothermal heat treatment [59,60].

Furthermore, the microstructural analysis of the sintered Distaloy SA (0.50Mo-1.50Cu-1.75Ni) + 4.0 wt. % SiC showcased a dual-phase ADI microstructure, with a black particle enveloped by a ferrite halo and unresolved zones comprising white bainitic ferrite plates and brown austenite plates. In traditional foundry metallurgy, the presence of graphite nodules, free ferrite, and ausferrite in ductile iron constitutes a dual-phase austempered ductile iron (Dual-phase ADI), which typically requires a specialized heat treatment procedure for formation. Remarkably, the sintered Distaloy SA (0.50Mo-1.50Cu-1.75Ni) + 4.0 wt. % SiC demonstrated the facile attainment of a dual-phase ADI microstructure through a single sintering cycle, suggesting its potential as a replacement for austempered ductile irons in certain applications.

4.2.1.4 Distaloy AE (0.50Mo-1.50Cu-4.00Ni) + 4.0 wt. % SiC

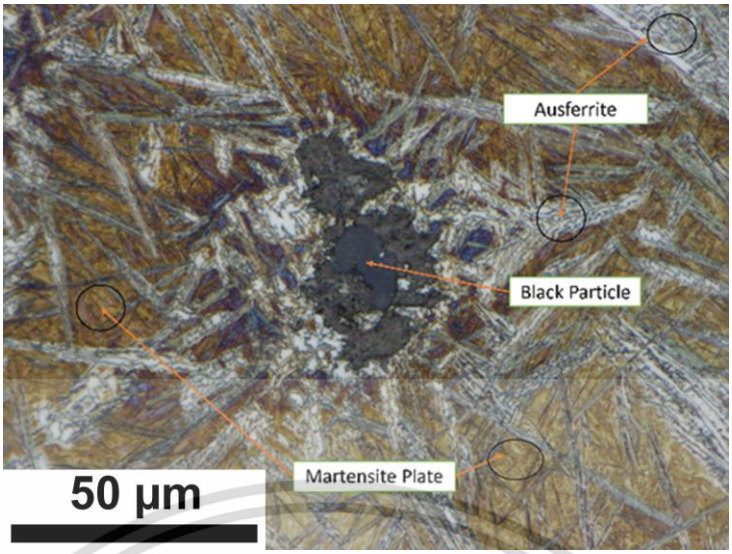

Figure 4. 6 Optical micrograph of sintered Distaloy AE (0.50Mo-1.50Cu-4.00Ni) + 4.0 wt. % SiC

The result of optical micrograph of sintered Distaloy AE (0.50Mo-1.50Cu-4.00Ni) + 4.0 wt. % SiC is shown in figure 4.6. The findings unveiled an ausferrite and MA (martensite-austenite) ADI (austempered ductile iron) microstructure in the sintered Distaloy AE composites, characterized by the presence of black particles enveloped by light blue areas and brown zones, where ferrite halos were completely absent. Upon high magnification observation, the light blue areas were identified as ausferrite, containing white bainitic ferrite plates and brown austenite plates, while the brown zones were recognized as MA islands housing martensite-austenite plates. The addition of 1.5 wt.% Cu and 4.0 wt.% Ni to the sintered Distaloy AE (0.50Mo-1.50Cu-4.00Ni) + 4.0 wt. % SiC led to the total replacement of pearlite nodules by ausferrite and MA islands, underscoring the alloy's distinct microstructural evolution.

Interestingly, a microstructure resembling ausferrite-MA ADI was previously documented in a sintered Fe-Ni-Si-C alloy with a 4.0 wt.% Ni content [60], and it was classified as ausferrite-MA ADI microstructure. However, such microstructures are rarely reported in traditional foundry practices concerning austempered ductile irons due to tempering temperatures being insufficiently low to facilitate martensite formation. MA ADI maintains the excellent mechanical characteristics found in conventional ADI, including its notable strength, toughness, and resistance to wear, while also potentially enhancing other aspects through specific modifications.

4.2.2 SEM Micrographs Of The Sintered Distaloy Composites

4.2.2.1 SEM of Distaloy DH + 4.0 wt. % SiC

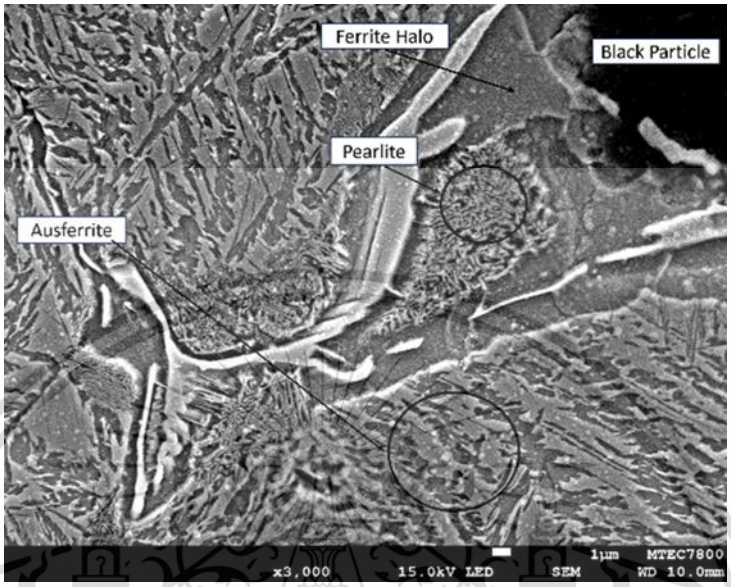

Figure 4. 7 SEM micrograph of sintered Distaloy DH (1.47Mo-2.0Cu) + 4.0 wt. % SiC

The result of SEM micrograph of sintered Distaloy DH + 4.0 wt. % SiC is shown in figure 4.7. The optical micrograph results of sintered Distaloy DH (1.47Mo-2.0Cu) + 4.0 wt.% SiC confirmed the presence of several distinct microstructural features. Specifically, the analysis revealed the existence of a black particle, a ferrite halo, pearlite, and ausferrite within the sample.

4.2.2.2 SEM of Distaloy DC1 + 4.0 wt. % SiC

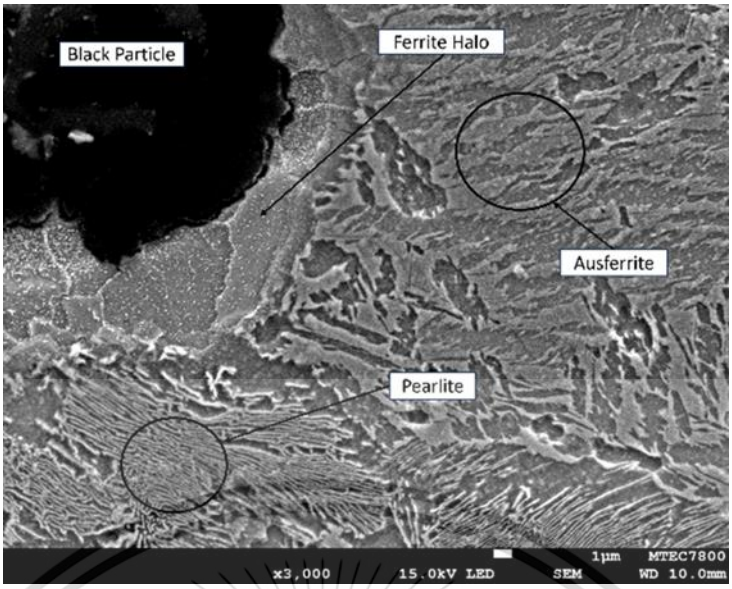

Figure 4. 8 SEM micrograph of sintered Distaloy DC1 (1.50Mo-2.0Ni) + 4.0 wt. % SiC

The presence of various microstructural features was confirmed in the optical micrograph results of sintered Distaloy DC1(1.50Mo-2.0Ni) + 4.0 wt.% SiC. Specifically, the analysis revealed that the sample contained a black particle, a ferrite halo, pearlite, and ausferrite.

4.2.2.3 SEM of Distaloy SA + 4.0 wt. % SiC

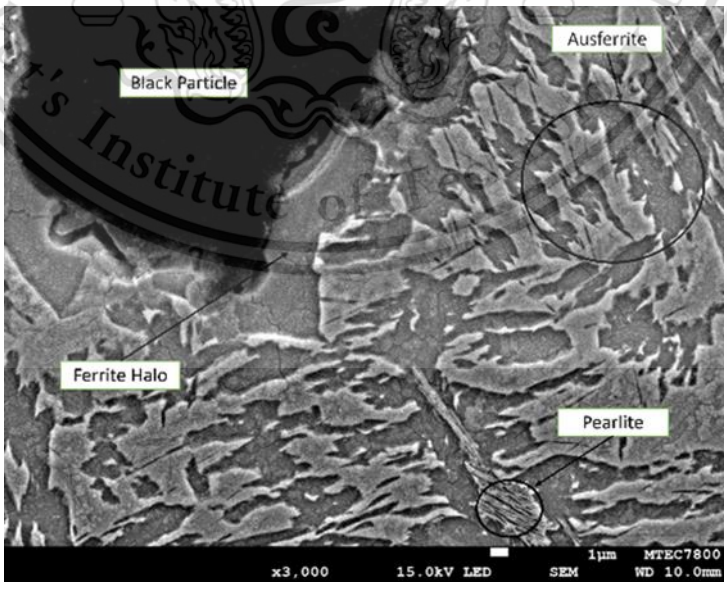

Figure 4. 9 SEM micrograph of sintered Distaloy SA (0.50Mo-1.50Cu-1.75Ni) + 4.0 wt. % SiC

The optical micrograph results of sintered Distaloy SA (0.50Mo-1.50Cu-1.75Ni) + 4.0 wt.% SiC verified the existence of diverse microstructural features. Specifically, the analysis clearly indicated the presence of a black particle, a ferrite halo, a small amount of pearlite, and ausferrite within the sample.

4.2.2.4 SEM of Distaloy AE + 4.0 wt. % SiC

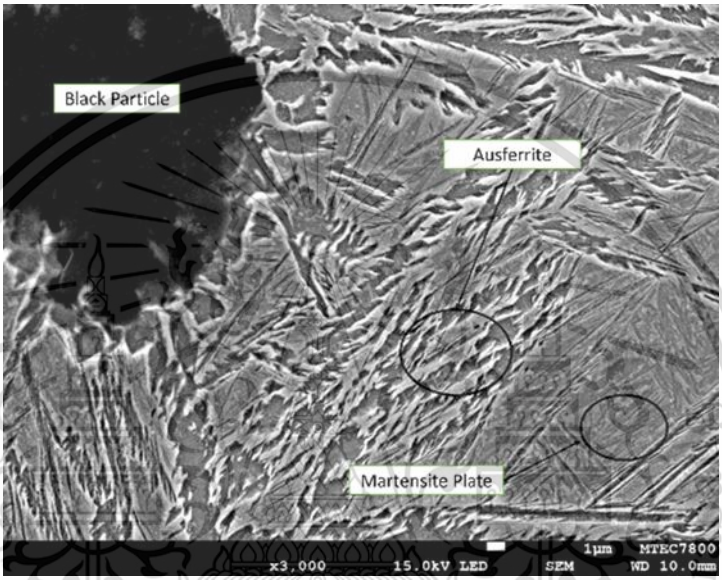

Figure 4. 10 SEM micrograph of sintered Distaloy AE (0.50Mo-1.50Cu-4.00Ni) + 4.0 wt. % SiC

SEM micrograph of sintered Distaloy AE's result is revealed the presence of multiple microstructural features in the sintered Distaloy AE (0.50Mo-1.50Cu-4.00Ni) + 4.0 wt.% SiC sample. Specifically, the analysis indicated the existence of a black particle, ausferrite, and MA islands composed of martensite plates within the sample.

4.3 XRD ANALYSIS OF THE SINTERED DISTALOY COMPOSITES

4.3.1 XRD of Distaloy DH + 4.0 wt. % SiC

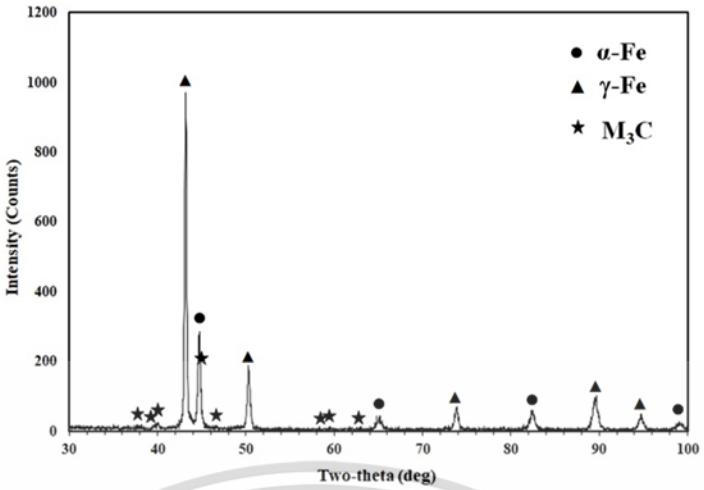

Figure 4. 11 X-ray diffraction pattern of sintered Distaloy DH (1.47Mo-2.0Cu) + 4.0 wt. % SiC

The result of X-ray diffraction pattern of sintered Distaloy DH (1.47Mo-2.0Cu) + 4.0 wt. % SiC revealed moderate peaks of α-ferrite with a body-centered cubic (bcc) crystal structure, along with strong peaks of γ-austenite exhibiting a face-centered cubic (fcc) crystal structure. Additionally, weak peaks of M_3C carbide with an orthorhombic crystal structure were observed. The XRD analysis confirmed the presence of ausferrite, characterized by γ-austenite and α-ferrite plates, and pearlite colonies, as indicated by the XRD peaks of M_3C carbide.

4.3.2 XRD of Distaloy DC1 + 4.0 wt. % SiC

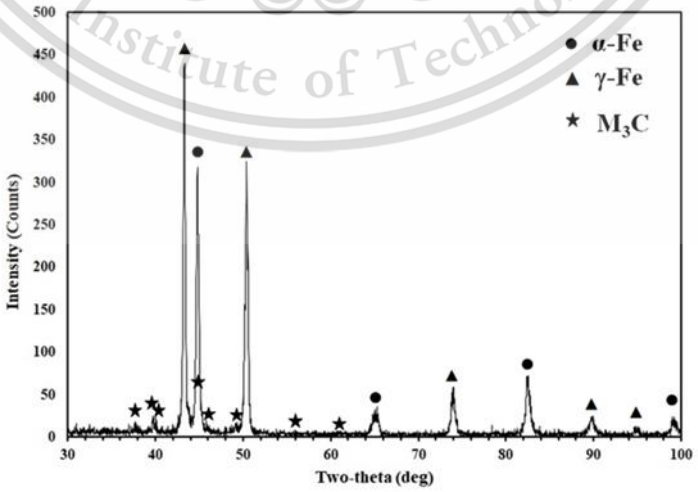

Figure 4. 12 X-ray diffraction pattern of sintered Distaloy DC1 (1.50Mo-2.0Ni) + 4.0 wt. % SiC

The finding of X-ray diffraction pattern of sintered Distaloy DC1 (1.50Mo-2.0Ni) + 4.0 wt. % SiC indicated that there were moderate peaks of **α**-ferrite characterized by a body-centered cubic (bcc) crystal structure, strong peaks of **γ**-austenite exhibiting a face-centered cubic (fcc) crystal structure, and weak peaks of M_3C carbide with an orthorhombic crystal structure. The matrices of both sintered Distaloy DH and Distaloy DC1 steels, comprising ferrite halo, pearlite, and ausferrite, imply the occurrence of three distinct phase transformations during slow post-sintered cooling. These transformations encompass the stable eutectoid transformation of austenite to ferrite halo, the metastable eutectoid transformation of austenite to pearlite, and the austempering transformation of austenite to ausferrite.

4.3.3 XRD of Distaloy SA + 4.0 wt. % SiC

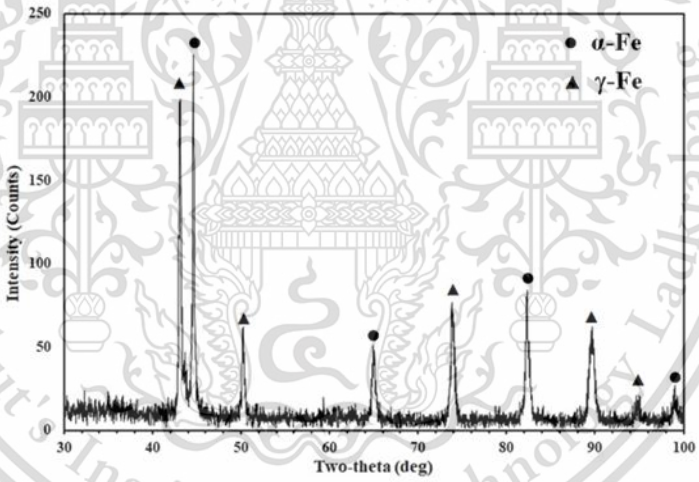

Figure 4. 13 X-ray diffraction pattern of sintered Distaloy SA (0.50Mo-1.50Cu-1.75Ni) + 4.0 wt. % SiC

The result of X-ray diffraction pattern of sintered Distaloy SA (0.50Mo-1.50Cu-1.75Ni) + 4.0 wt. % SiC revealed prominent peaks of **α**-ferrite characterized by a body-centered cubic (bcc) crystal structure, alongside robust peaks of **γ**-austenite demonstrating a face-centered cubic (fcc) crystal structure. This validation supports the microstructural feature identified in sintered Distaloy SA steel, where a black particle was enclosed within a matrix consisting of ferrite halo and ausferrite.

4.3.4 XRD of Distaloy AE + 4.0 wt. % SiC

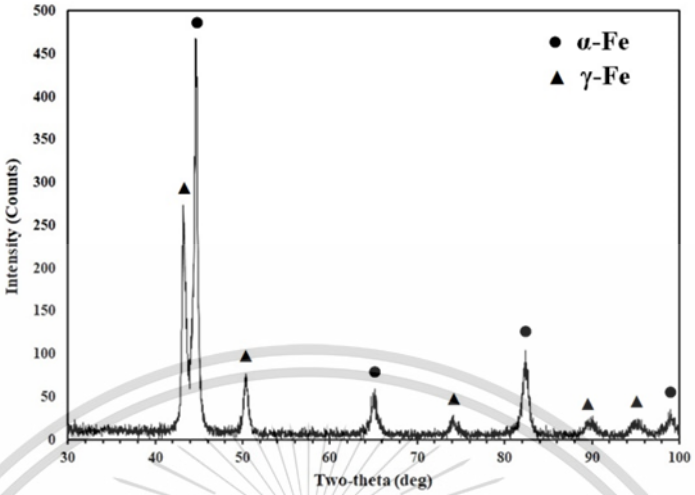

Figure 4. 14 X-ray diffraction pattern of sintered Distaloy AE (0.50Mo-1.50Cu-4.00Ni) + 4.0 wt. % SiC

The result of X-ray diffraction pattern of sintered Distaloy AE (0.50Mo-1.50Cu-4.00Ni) + 4.0 wt. % SiC demonstrated prominent peaks of α-ferrite, indicating a body-centered cubic (bcc) crystal structure, as well as robust peaks of γ-austenite, indicative of a face-centered cubic (fcc) crystal structure. This served as evidence that the microstructural feature observed in sintered Distaloy AE steel included a black particle embedded within a matrix composed of bainitic ferrite and martensite plates.

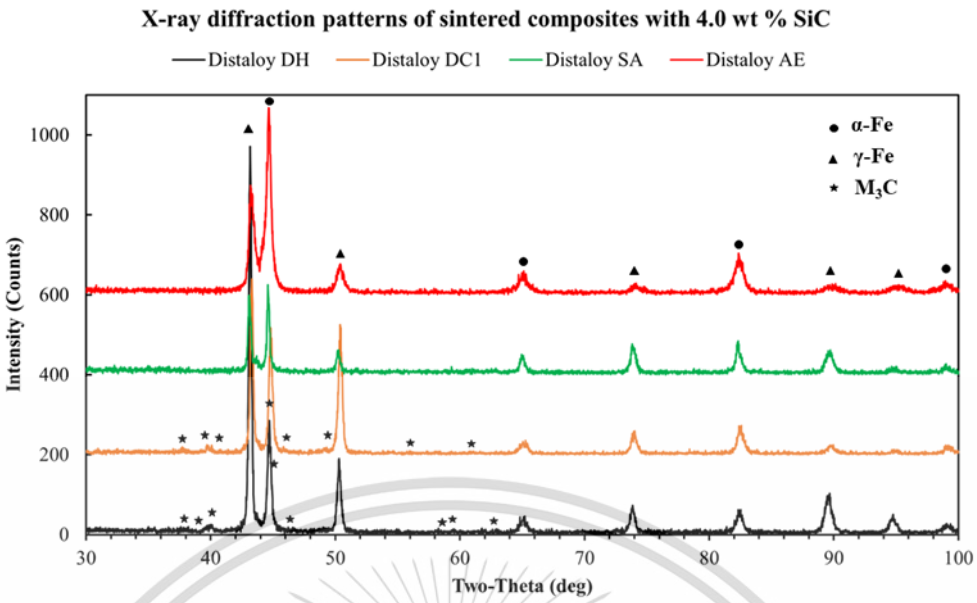

Figure 4. 15 The patterns of X-ray diffraction analysis of all sintered Distaloy composites

4.4 THE EPMA CHEMICAL DISTRIBUTION IN THE EXPERIMENTAL SINTERED DISTALOY COMPOSITES

Electron Probe Micro-Analysis, or EPMA, is a method employed in materials science for analyzing the elemental composition of a sample. This involves directing a concentrated electron beam onto the sample, which then emits characteristic X-rays that are measured to identify the elements present. Through EPMA, researchers can gain in-depth insights into the distribution and concentration of elements within the sample, aiding in the comprehension of its chemical makeup and structure. EPMA proves invaluable for scrutinizing the microstructure of materials and exploring elemental distribution, phase segregation, and various other microscopic characteristics.

In figure 4.16, EPMA elemental distribution maps were generated within the vicinity of pearlite colonies in sintered Distaloy DH steel. The analysis revealed that the pearlite colonies exhibited elevated levels of C, Mo, and Cu, alongside decreased concentrations of Fe and Si, in contrast to the adjacent ausferrite regions. Conversely, all elements, including C, Cu, Fe, Mo, and Si, displayed uniform distribution across the ausferrite areas. In figure 4.17, similar investigations were conducted on sintered Distaloy DC1 steel. The findings unveiled that pearlite colonies showcased heightened

C levels, but reduced Fe and Si concentrations compared to the surrounding ausferrite regions. Furthermore, the alloying elements Mo and Ni exhibited notably even distribution within both pearlite and ausferrite phases.

The elemental distribution maps suggest a correlation between low Si concentration and pearlite formation. It is widely acknowledged that an appropriate Si content can hinder carbide precipitation from austenite [62]. This inhibition occurs because the lack of a precipitation driving force makes it challenging for para-equilibrium carbides to form from austenite. Consequently, carbide precipitation can only occur through silicon partitioning, which may prolong the process significantly [63]. Moreover, the precipitation of M_3C carbide lamellae within pearlite colonies in both sintered Distaloy DH and Distaloy DC1 steels is attributed to the high C concentration in austenite, facilitating carbide precipitation due to the substantial driving force for the reaction, even in para-equilibrium conditions.

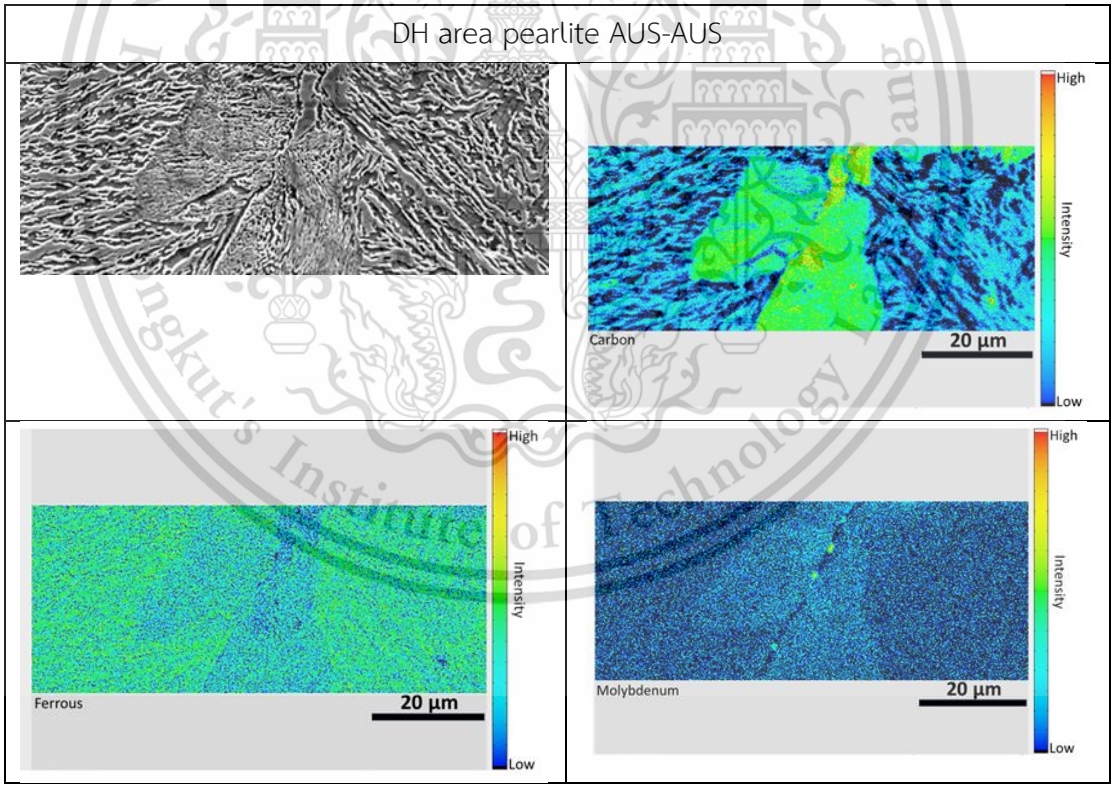

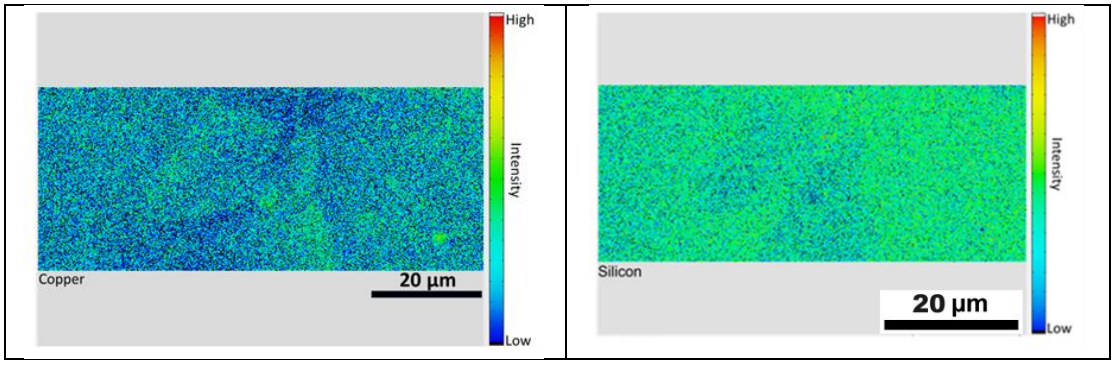

Figure 4. 16 Elemental distribution of EPMA maps of sintered Distaloy DH + 4.0 wt.% SiC composites

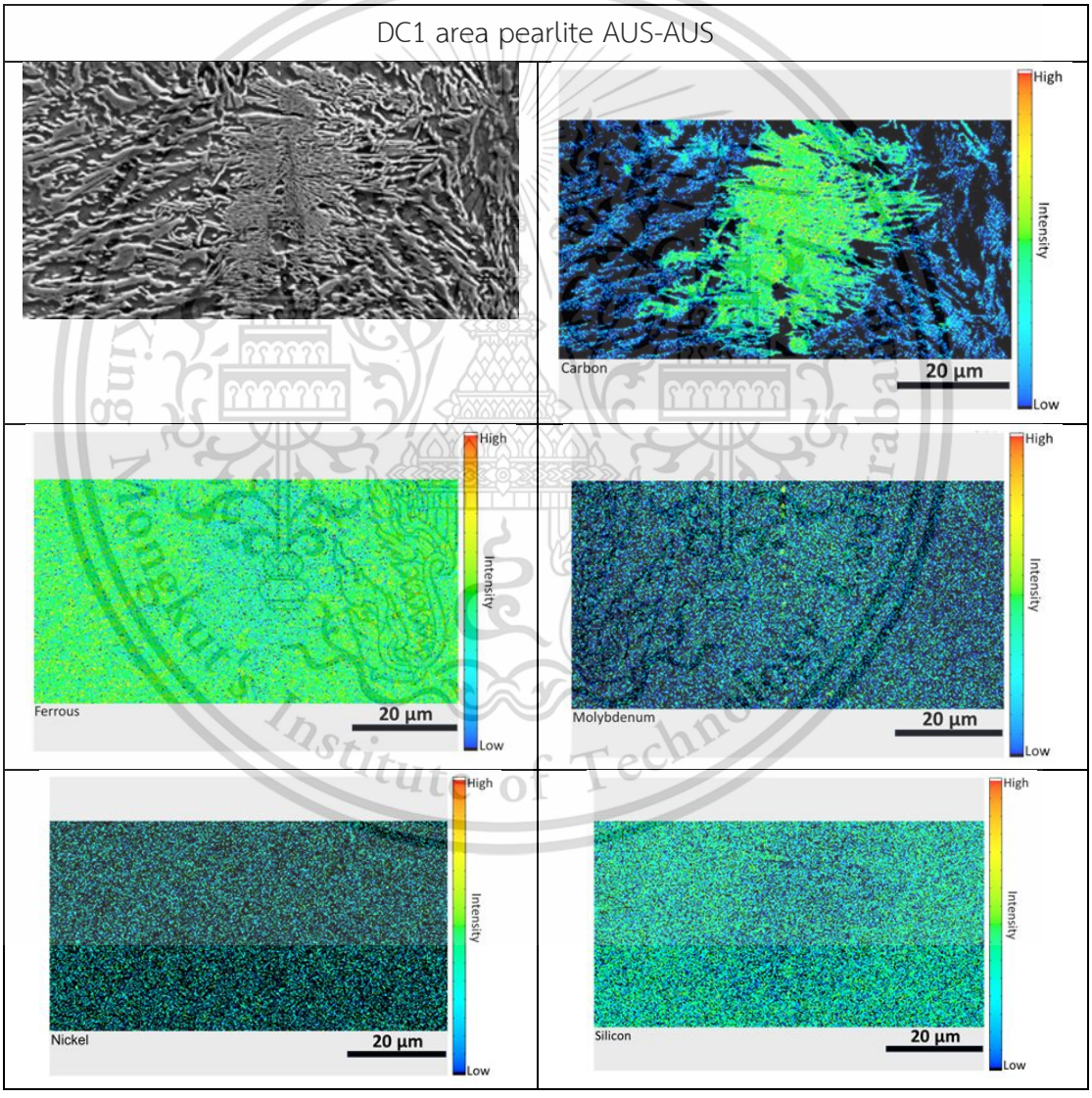

Figure 4. 17 Elemental distribution of EPMA maps of sintered Distaloy DC1 + 4.0 wt.% SiC composites

4.5 MECHANICAL PROPERTIES OF THE SINTERED DISTALOY COMPOSITES

4.5.1 Macro Hardness And Tensile Properties Of The Sintered Distaloy Composites

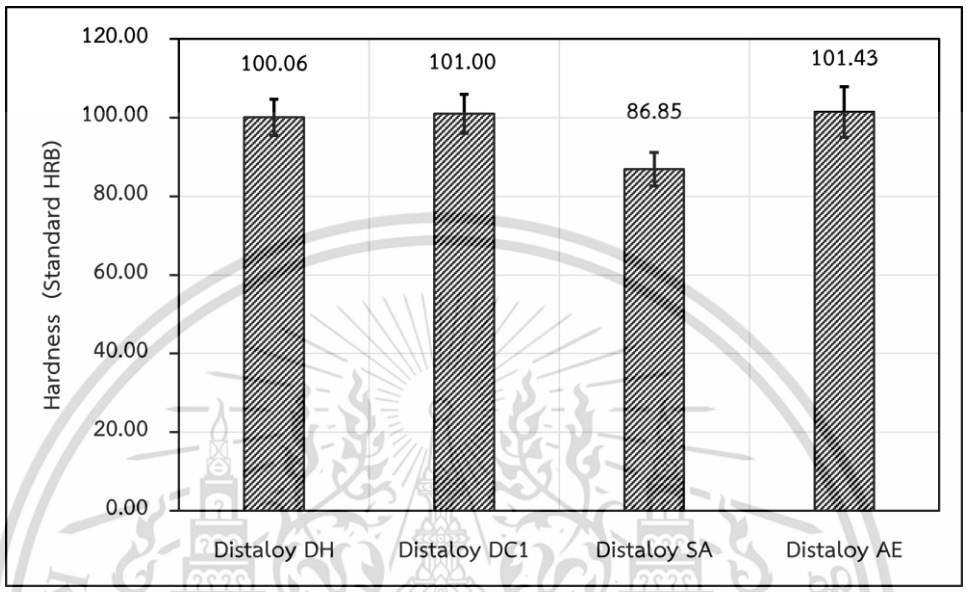

Figure 4. 18 The macro hardness values of the sintered Distaloy composites

The outcomes of all the experimental sintered Distaloy composites demonstrated favorable mechanical properties, with ultimate tensile strength (UTS) values exceeding 700 MPa, yield strength (YS) values surpassing 250 MPa, elongation values greater than 5.0%, and hardness values exceeding 80 HRB as shown in figure 4.18 and figure 4.19.

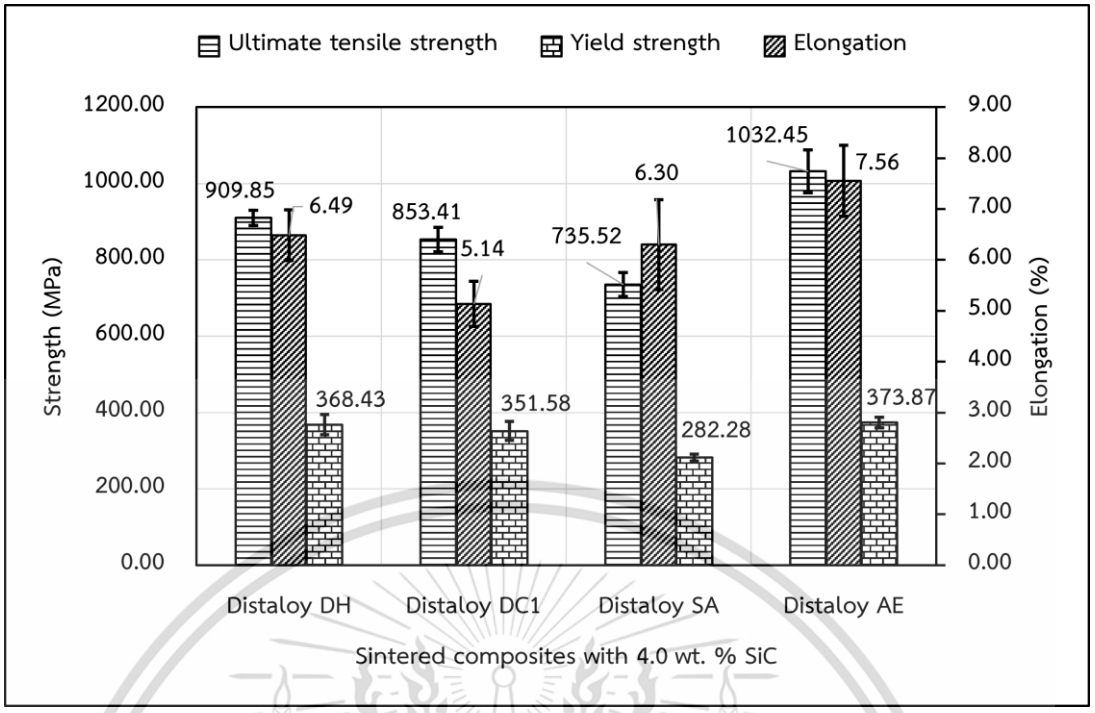

Figure 4. 19 The tensile properties of the sintered Distaloy composites

Figure 4.19 presents the tensile properties of the experimental sintered Distaloy composites. Notably, the sintered Distaloy AE composites exhibited elevated highest tensile strength, highest hardness, and considerable highest elongation. Conversely, the sintered SA composites displayed the lowest tensile strength and hardness, albeit with a notably high elongation value.

Regarding tensile strength and elongation, it was noted that among the experimental sintered steels, the sequence in terms of tensile strength was sintered Distaloy AE is greater than sintered Distaloy DH and sintered DC1 is greater than sintered SA, while in terms of elongation, it was sintered Distaloy AE is greater than sintered Distaloy DH and sintered Distaloy SA is greater than sintered Distaloy DC1. This suggests a collaborative relationship between strength and ductility in the experimental sintered Distaloy composites. Typically, materials with high strength often experience compromised ductility, a phenomenon known as the strength-ductility trade-off dilemma. Various strategies exist to address this challenge in materials, literature suggested that overcoming the strength-ductility trade-off dilemma in materials relies on various factors including the dual-phase lamellar microstructure [64], core-shell microstructure [65], nano-twinning [66], dual heterogeneous structure [67], heterogeneous structure [68], metastability-engineering strategy [69], and micro-

banding coupled with the accumulation of a high density of dislocations in single-phase high-entropy alloys (HEAs) [70]. Upon analyzing the microstructural characteristics of sintered Distaloy DH, Distaloy DC1, and Distaloy SA composites, it becomes evident that the dual-phase lamellar microstructure, characterized by alternating bainitic ferrite and austenite plates, acts as the mechanism for mitigating the strength-ductility trade-off dilemma. In contrast, when juxtaposed with the microstructures of materials adept at tackling the strength-ductility trade-off issue as delineated in references [64-70], the microstructural composition of sintered Distaloy AE composites seems to possess a distinctive characteristic dual-phase lamellar microstructure, ausferrite-MA ADI microstructure demonstrating its ability to bypass the strength-ductility dilemma of trade-off challenge.

4.6 WEAR TEST OF THE SINTERED DISTALOY COMPOSITES (TRIBOLOGY PROPERTIES)

A wear test, also referred to as a wear resistance test, serves as a mechanical evaluation method aimed at gauging materials' ability to endure wear and abrasion under specific circumstances. Its purpose lies in assessing the durability and functionality of materials in scenarios characterized by friction, rubbing, and abrasive interactions. It aims to determine how effectively a material can withstand wear and damage when exposed to diverse environmental and loading conditions. For this study, Distaloy powders namely Distaloy DH, Distaloy DC1, Distaloy SA, and Distaloy AE mixed with 4.0 wt. % SiC are utilized. The samples designated for the wear test undergo sintering at 1250 ℃ for 45 minutes in a vacuum furnace, followed by gradual slow cooling to room temperature at a rate of 0.1 ℃/s. Typically, the wear test entails the measurement of parameters such as coefficient of friction, specific wear rate, volume loss, analysis of worn surfaces, analysis of wear debris and wear scar diameter which aids in quantifying the material's wear resistance. The conditions for the wear test used for the sintered Distaloy composites are as follows.

Pinball chromium = Ø diameter 6 mm

Distance = 1000 m

Track radius = 6 mm

Speed = 160 rpm (velocity 0.1 m/s)

Time duration = 02 hours: 45 minutes

Room temperature = 29-33 ℃

Relative humidity = 64-74 %

Load test = 15 N

4.7 COEFFICIENT OF FRICTION (COF) OF SINTERED DISTALOY COMPOSITES

The coefficient of friction (COF) plays a crucial role in wear testing as it provides valuable insights into how materials behave and respond when subjected to friction and abrasion conditions. Understanding the coefficient of friction is vital during wear testing, as it offers valuable insights into the performance and interaction of materials under friction and abrasion circumstances. In wear testing, the coefficient of friction is pivotal as it offers critical insights into how materials behave and perform when experiencing friction and abrasion.

The friction coefficient properties of sintered Distaloy composites were investigated under various conditions. The testing involved a sliding velocity of 0.1 m/s and a normal load of 15N, with all specimens tested over a sliding distance of 1,000 m at room temperature and a relative humidity range of 64-74%. The tribometer test utilized disk specimens with a roughness of 4-5 μm, paired with a 6 mm diameter ball made of SKF chromium steel grade G20, having a hardness of 838 ± 21 HV and a roughness of 4 μm as the counterpart material. Friction tests conducted at various normal loads revealed two distinct stages in the friction coefficient plotted against sliding distance for all sintered Distaloy composites. Following an initial stage, the friction coefficient values of all sintered alloys remained consistent regardless of the sliding distance. Under a normal load of 15N, sintered Distaloy DH + 4.0 wt. % SiC exhibited the highest COF, whereas the COF values of sintered Distaloy DC1 + 4.0 wt. % SiC and sintered Distaloy SA + 4.0 wt. % SiC were the lowest. The inclusion of 2.0 wt.% Cu appears to positively influence the friction coefficient of the sintered Distaloy composites. The results revealed a two-stage wear mechanism, consisting of the run-in stage and the stable stage. During the run-in stage, observed in the initial 0-100m of the test, the friction coefficient exhibited instability due to the low roughness of the point contact between the ball and the surface of the sintered composite. However,

as the test progressed beyond 100m, the friction coefficient stabilized with increasing distance, indicating a transition to a steady state. This stability in friction coefficient was attributed to the transition from point contact to surface contact between the counter ball and the sintered composites, accompanied by the flaking off of graphite particles from the surface, which acted as a lubricant, thereby reducing the friction coefficient.

Furthermore, the results depicted in figure 4.21 illustrated that sintered Distaloy DC1 composites exhibited the lowest average coefficient of friction, whereas sintered Distaloy DH composites demonstrated the highest average coefficient of friction.

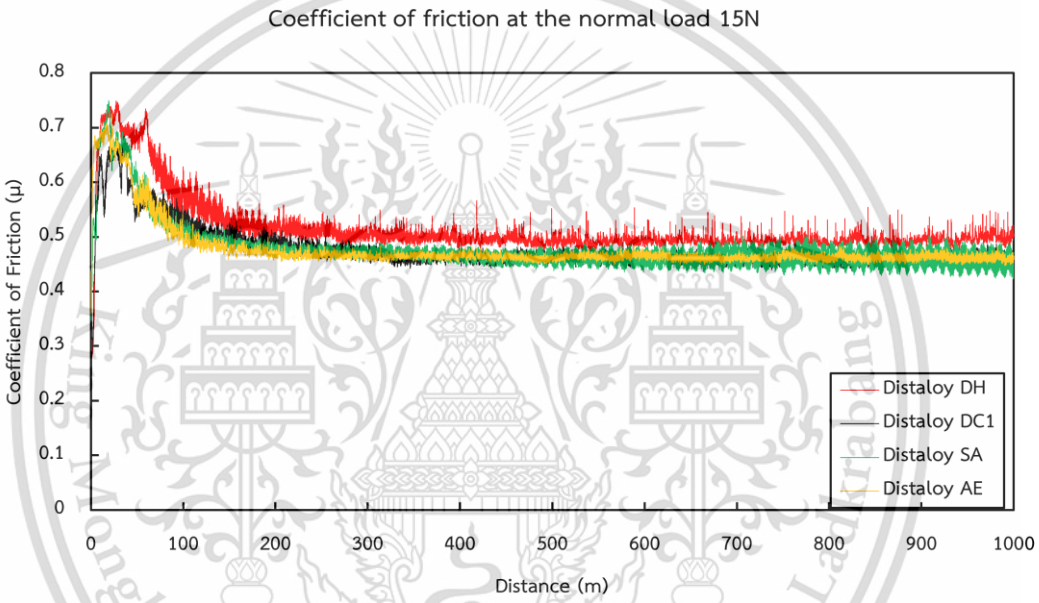

Figure 4. 20 The coefficient of friction at load 15N of all sintered Distaloy composites

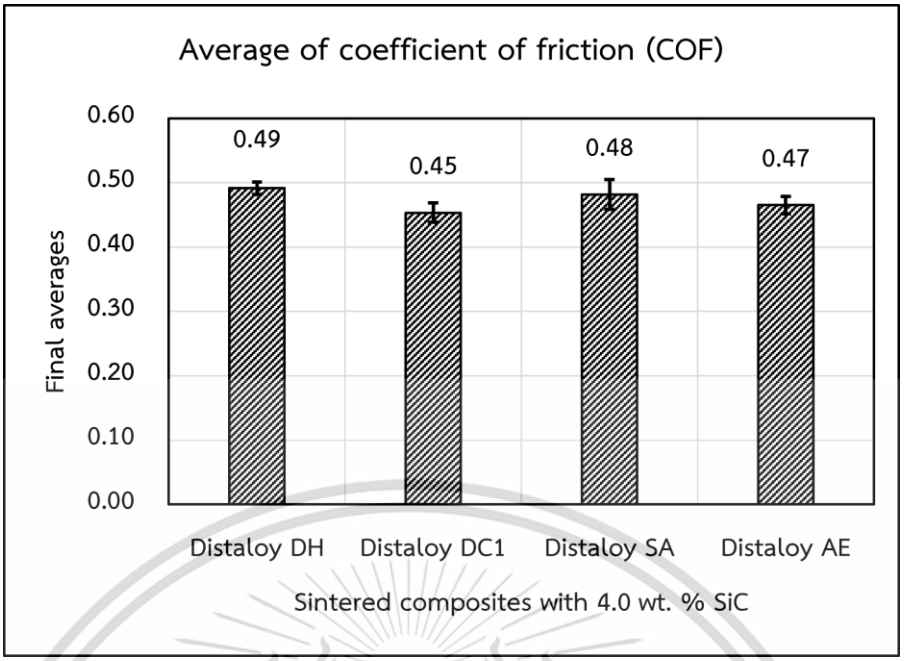

Figure 4. 21 The average of coefficient of friction at load 15N of the sintered Distaloy composites

4.8 SPECIFIC WEAR RATES OF THE SINTERED DISTALOY COMPOSITES

The wear test results were utilized to calculate the specific wear rates of the sintered Distaloy composites, offering insight into how much material is lost per unit load and sliding distance. This parameter is crucial for assessing the wear resistance of materials and their performance under friction and abrasion conditions. By measuring the weight loss of the specimens' post-wear test, the specific wear rates were determined, providing valuable data on material loss relative to sliding distance and load. Comparing these specific wear rates among the different sintered Distaloy composites allowed for an assessment of their relative wear resistance properties. The average specific wear rate of the coin specimens denotes the measure of material loss per unit load and sliding distance observed during the wear test executed on the coin-shaped specimens. Similarly, the average specific wear rate of the steel balls reflects the pace at which material is worn away per unit load and sliding distance during the wear test carried out on the steel balls.

The specific wear rates offered valuable insights into the tribological behavior of the sintered Distaloy composites, contributing to the evaluation of their suitability for various applications where wear resistance is paramount. The wear rate, which

corresponds to the sliding distance and applies a normal load of 15N, is utilized to quantify material removal during tribology tests. In figure 4.22, the average specific wear rate of the coin specimens is illustrated. It was observed that sintered Distaloy SA composites exhibited the highest average specific wear rate, while sintered Distaloy AE composites displayed the lowest. This difference can be attributed to the presence of ausferrite-MA ADI microstructure in sintered Distaloy AE composites and dual-phase ADI microstructure in sintered Distaloy SA composites. Figure 4.23 depicts the average specific wear rate of steel balls. The results indicated that sintered Distaloy SA composites exhibited the highest average specific wear rate, whereas sintered Distaloy DC1 composites displayed the lowest. This variation is due to the microstructural differences between the two materials, with sintered Distaloy DC1 composites containing ferrite halo, pearlite, and ausferrite microstructure, and featuring dual-phase ADI microstructure of sintered Distaloy SA composites.

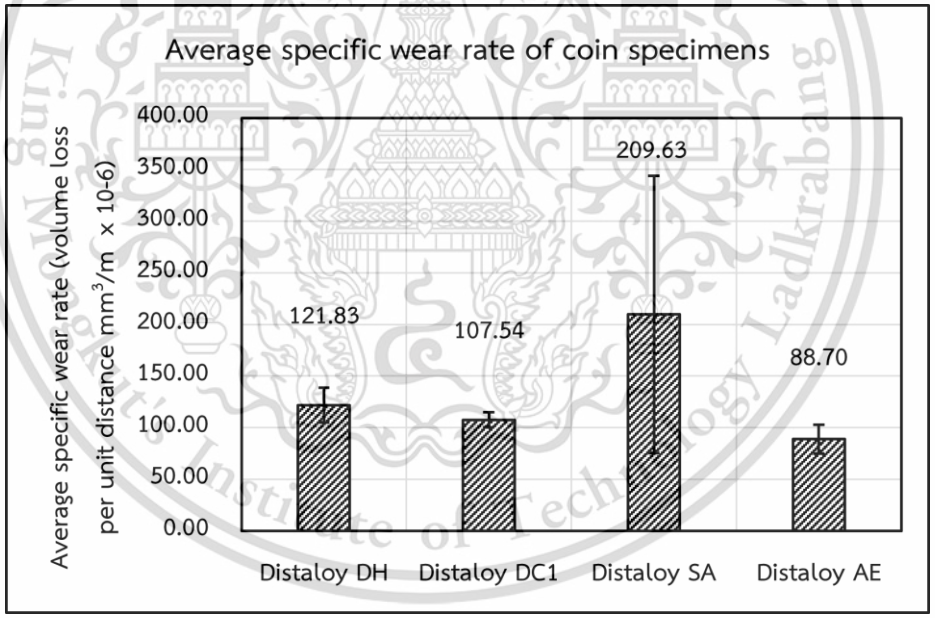

Figure 4. 22 The average of specific wear rate at test load 15N of coin specimens of sintered Distaloy composites

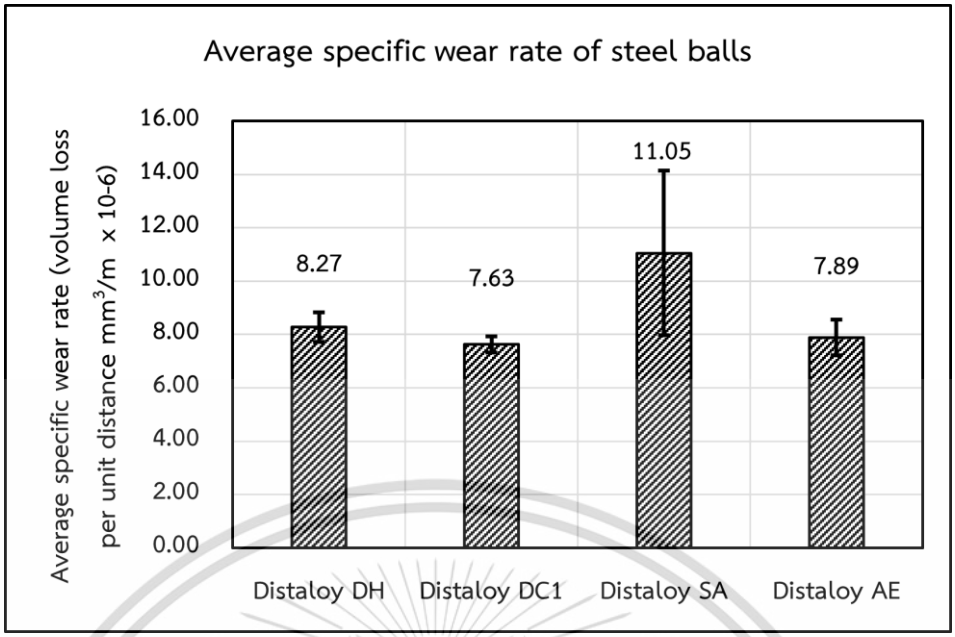

Figure 4. 23 The average of specific wear rate at test load 15N of pin steel balls

4.9 VOLUME LOSS OF THE SINTERED DISTALOY COMPOSITES

The reduction in volume experienced by the sintered Distaloy composites due to wear and abrasion during testing or application is known as volume loss. The average volume loss of the coin specimens denotes the typical reduction in volume experienced by these specimens due to wear and abrasion during testing or application. An average decrease in volume, observed in the steel balls during testing or application, indicates the typical reduction in volume due to wear and abrasion, as represented by the average volume loss of the steel balls.

In figure 4.24, the average volume loss of coin specimens for sintered Distaloy composites is depicted. With sintered Distaloy AE composites featuring an ausferrite-MA ADI microstructure and sintered Distaloy SA composites having a dual-phase ADI microstructure, it was observed that sintered Distaloy SA composites exhibited the largest average volume loss, while sintered Distaloy AE composites displayed the smallest average volume loss. Figure 4.25 illustrates the average volume loss of steel balls. According that sintered Distaloy DC1 composites possess a microstructure consisting of ferrite halo, pearlite, and ausferrite, whereas sintered Distaloy SA composites feature a dual-phase ADI microstructure, the results revealed that sintered

Distaloy SA composites experienced the highest average volume loss, whereas sintered Distaloy DC1 composites demonstrated the lowest average volume loss.

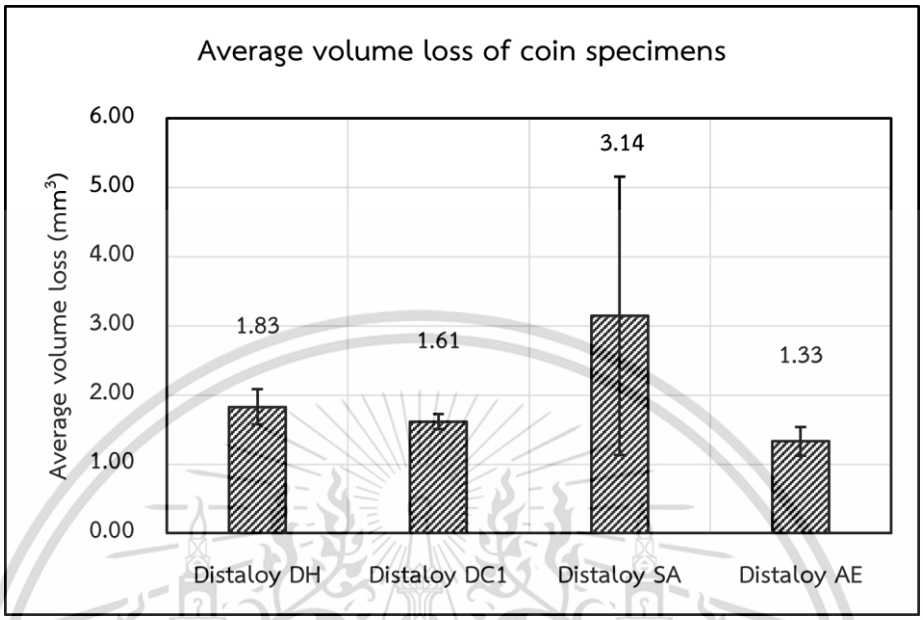

Figure 4. 24 The average volume loss at test load 15N of coin specimens of sintered Distaloy composites

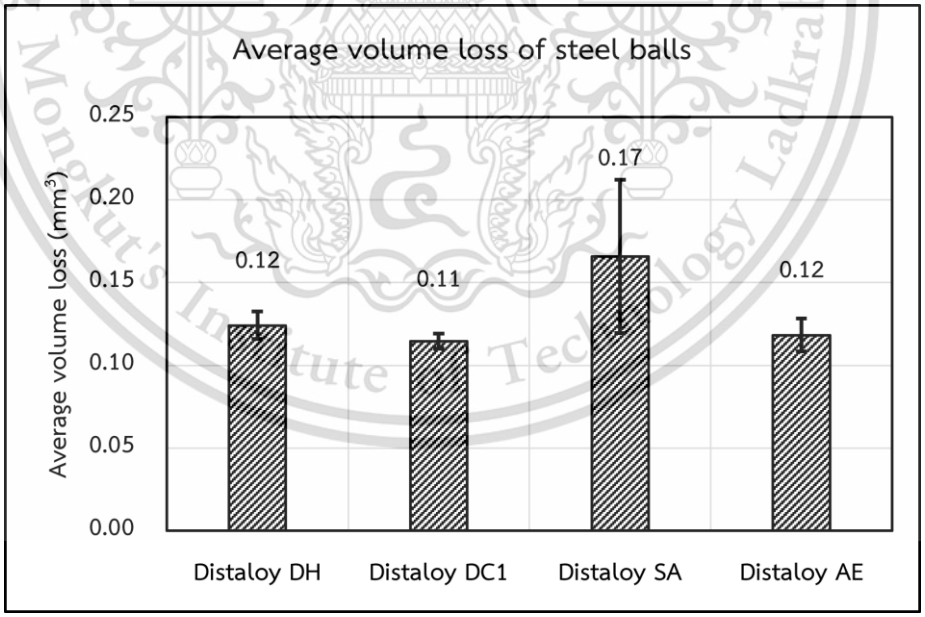

Figure 4. 25 The average volume loss at test load 15N of pin steel balls

4.10 WORN SURFACES AND WEAR DEBRIS OF SINTERED DISTALOY COMPOSITES.

4.10.1 Worn Surfaces Of All Sintered Distaloy Composites At The Normal Load 15N

The worn surfaces of all sintered Distaloy composites were subjected to examination under a normal load of 15N. An assessment was conducted to observe the degree of wear and damage sustained by the Distaloy composites following the wear testing. Abrasive wear manifests when hard particles or abrasive substances slide against a surface, leading to material removal through mechanical abrasion [71], [72]. This phenomenon commonly occurs when there is relative movement between two surfaces with differing levels of hardness, causing the softer material to be abraded by the harder particles. Adhesive wear, conversely, occurs when two surfaces make direct contact, resulting in the formation of molecular bonds between them. As these surfaces slide or rub against each other, these bonds may rupture, causing material transfer from one surface to the other. This material transfer can result in the generation of wear debris and surface damage. Delamination wear entails the gradual separation or peeling of layers from the surface of a material. It typically occurs in laminated or layered materials where the bonding between layers is weaker than the cohesive forces within the layers. Delamination wear may arise due to cyclic loading, thermal stresses, or other mechanical factors, leading to the creation of distinct layers or flakes on the material's surface.

Upon inspection of the worn surfaces of all sintered composites under a normal load of 15N, it was noted that three common wear mechanisms, namely abrasive, adhesive, and delamination/fatigue, were evident on the surfaces of each sintered alloy. These mechanisms included the presence of oxide fragments, oxide formation, microcracks, delamination, debris/oxide, and black particles. In figure 4.26, the results of the wear test conducted on sintered Distaloy DH + 4.0% wt. SiC revealed the occurrence of wear mechanisms such as delamination, oxide fragments, tribo film, debris/oxide, and abrasive wear grooves. The wear test results for sintered Distaloy DC1 + 4.0% wt. SiC indicated the presence of wear mechanisms including delamination

and microcracks. For sintered Distaloy SA + 4.0% wt. SiC, the wear test results showed wear mechanisms such as delamination and oxide formation. Similarly, in the case of sintered Distaloy AE + 4.0% wt. SiC, the wear test results highlighted wear mechanisms such as delamination and the presence of black particles.

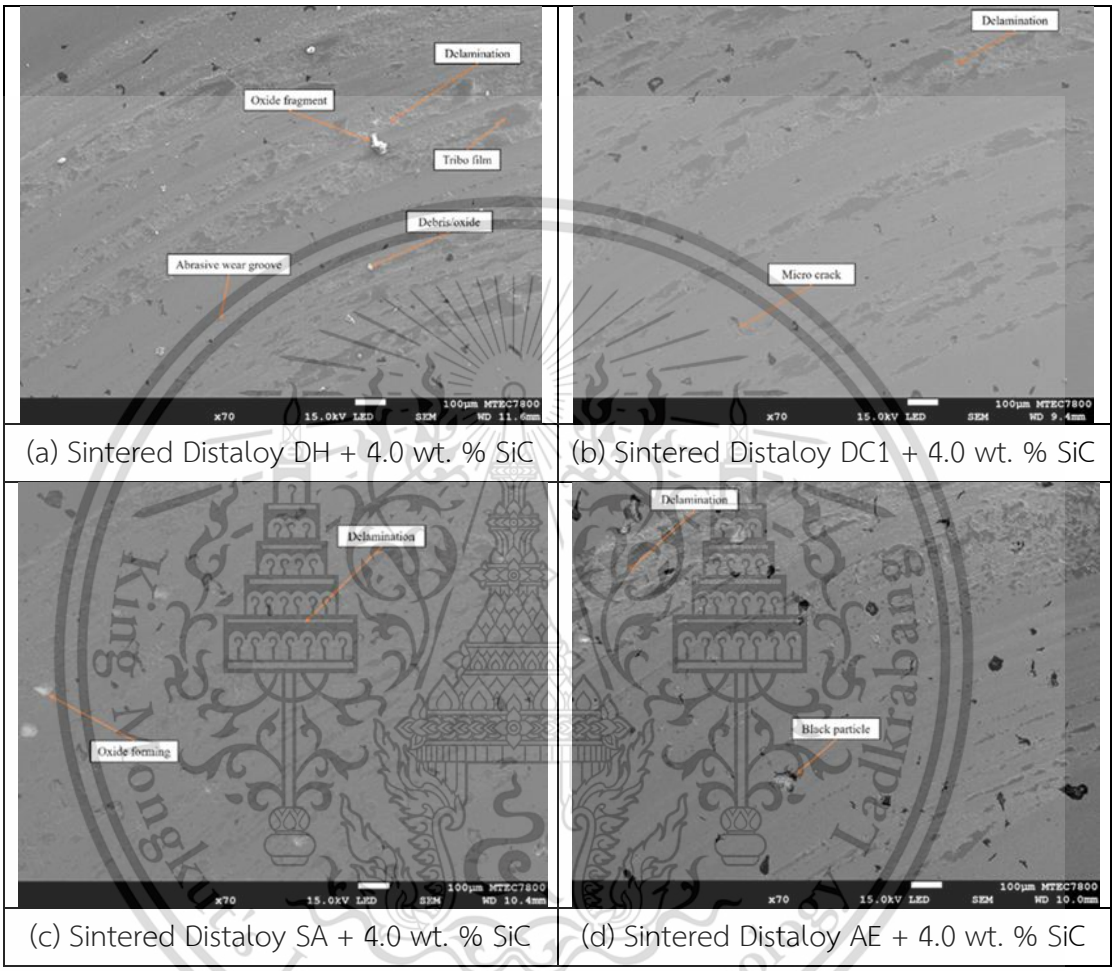

(a) Sintered Distaloy DH + 4.0 wt. % SiC (b) Sintered Distaloy DC1 + 4.0 wt. % SiC

(c) Sintered Distaloy SA + 4.0 wt. % SiC (d) Sintered Distaloy AE + 4.0 wt. % SiC

Figure 4. 26 SEM micrographs of worn surface of sintered Distaloy composites at load 15N

4.10.2 Wear Debris Of All Sintered Distaloy Composites At The Normal Load 15N

The SEM micrographs in figure 4.27 compare the wear debris resulting from the wear test of sintered Distaloy DH composite, sintered Distaloy DC1 composite, sintered Distaloy SA composite, and sintered Distaloy AE composite under a normal load of 15N. The wear debris of all sintered Distaloy composites exhibit irregular geometry, indicating the delamination wear mechanism caused by severe plastic deformation.

After the wear test at a normal load of 15N, the wear debris of sintered Distaloy DH + 4.0 wt. % SiC composites displayed irregular shapes, characteristic of wear delamination. Additionally, oxide formations were observed in the wear debris of these composites. Similarly, the wear debris of sintered Distaloy DC1 + 4.0 wt. % SiC composites exhibited irregular shapes due to wear delamination, accompanied by oxide formations. The wear debris of sintered Distaloy SA + 4.0 wt. % SiC composites also showed irregular shapes resulting from wear delamination, along with oxide formations. Likewise, the wear debris of sintered Distaloy AE + 4.0 wt. % SiC composites displayed irregular shapes attributed to wear delamination, with accompanying oxide formations. The micrographs indicate irregular geometry, confirming the presence of the delamination wear mechanism. Additionally, plate-like structures observed in the micrographs suggest the occurrence of adhesion wear [73]. Furthermore, the worn surfaces of all sintered composites display oxide agglomerates, indicating oxidative wear [71].

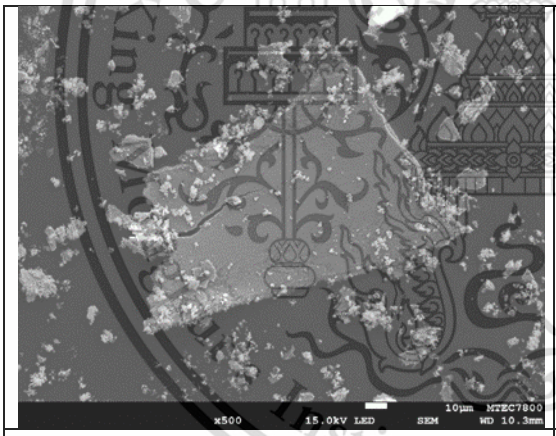

(a) Sintered Distaloy DH + 4.0 wt. % SiC

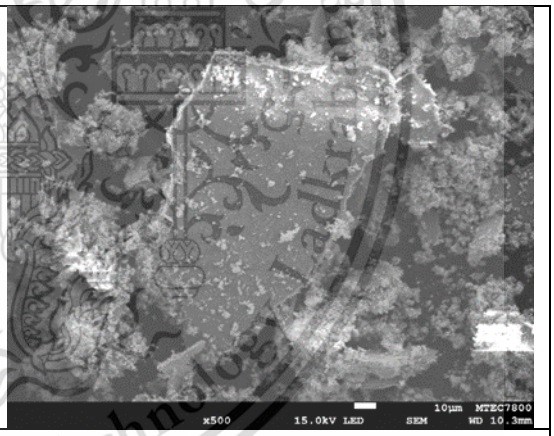

(b) Sintered Distaloy DC1 + 4.0 wt. % SiC

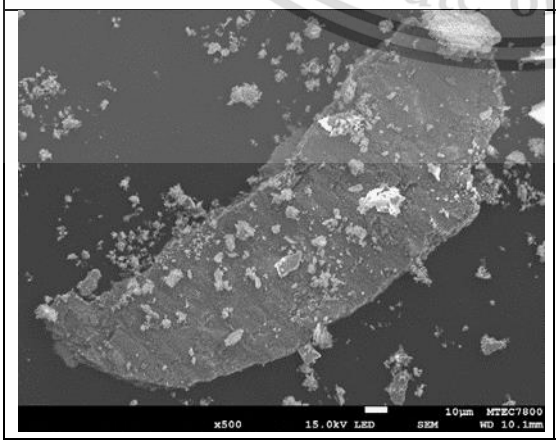

(c) Sintered Distaloy SA + 4.0 wt. % SiC

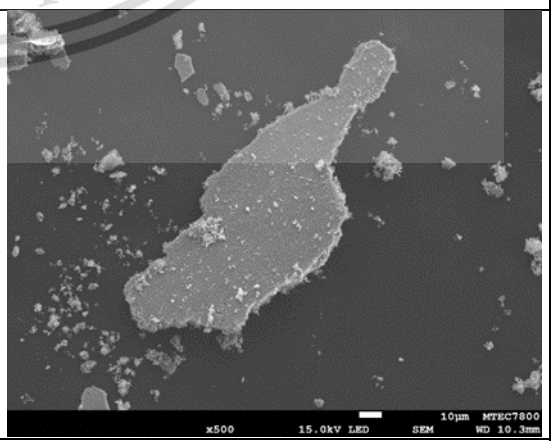

(d) Sintered Distaloy AE + 4.0 wt. % SiC

Figure 4. 27 SEM micrographs of wear debris of sintered Distaloy composite at load 15N

4.11 EDS ANALYSIS OF WEAR DEBRIS OF ALL SINTERED DISTALOY COMPOSITES AT THE NORMAL LOAD 15N

Figure 4.28 to 4.31 display the EDS spectrums of wear debris from sintered Distaloy composites under a normal load of 15N. These spectra reveal intense peaks of oxygen, indicating the presence of iron oxide resulting from oxidative wear, along with small peaks of chromium, signifying debris from the counter ball surface. Additionally, peaks of iron, carbon, and silicon are observed in the wear debris of all sintered Distaloy composites, further confirming the formation of iron oxide due to oxidative wear.

The findings from the wear test of sintered Distaloy DH + 4.0 wt. % SiC are illustrated in figure 4.28, corroborating the formation of oxides in the wear debris. Similarly, the results from the wear test of sintered Distaloy DC1 + 4.0 wt. % SiC, depicted in figure 4.29, provide evidence of oxide formation in the wear debris. Likewise, the outcomes of the wear test conducted on sintered Distaloy SA + 4.0 wt. % SiC, shown in figure 4.30, support the formation of oxides in the wear debris. Similarly, the results of the wear test carried out on sintered Distaloy AE + 4.0 wt. % SiC, presented in figure 4.31, confirm the formation of oxides in the wear debris.

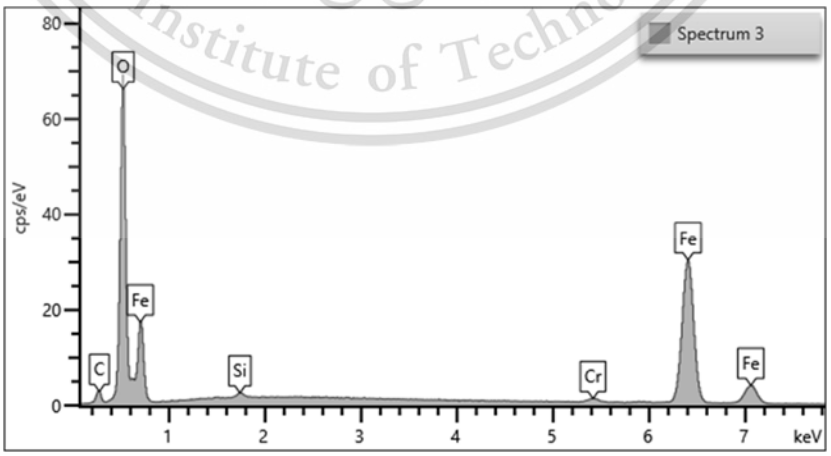

Figure 4. 28 EDS spectrum of wear debris of sintered Distaloy DH + 4.0 wt. % SiC

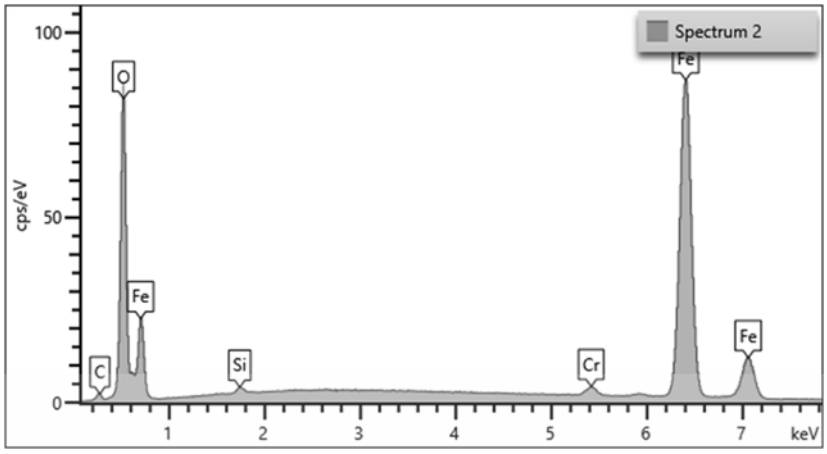

Figure 4. 29 EDS spectrum of wear debris of sintered Distaloy DC1 + 4.0 wt. % SiC

Figure 4. 30 EDS spectrum of wear debris of sintered Distaloy SA + 4.0 wt. % SiC

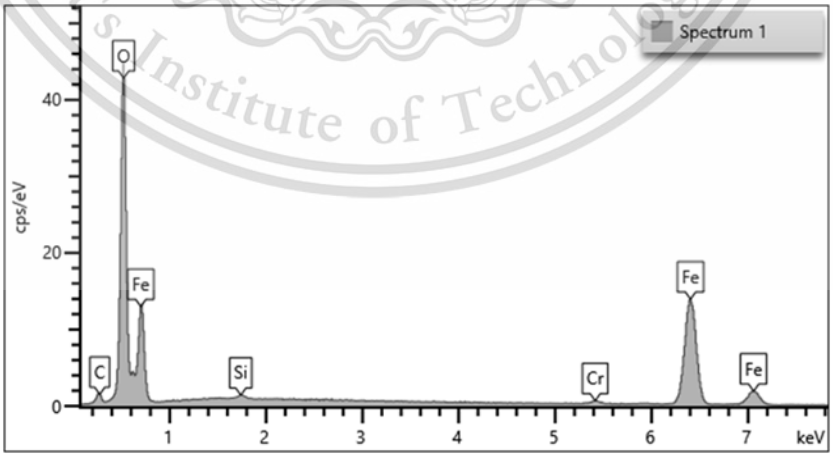

Figure 4. 31 EDS spectrum of wear debris of sintered Distaloy AE + 4.0 wt. % SiC

4.12 WORN SURFACES AND WEAR DEBRIS OF SINTERED DISTALOY DH + 4.0 WT. % SIC AT THE NORMAL LOAD 15N.

Figure 4.32 displays the SEM micrographs of the worn surfaces of sintered Distaloy DH + 4.0 wt. % SiC composite under a normal load of 15N. In contrast, figure 4.33 showcases the wear debris generated from the same composite under the same load condition. Both figures illustrate the presence of delamination wear on the worn surfaces at 15N and a little oxide fragment, tribo film, a little debris and abrasive wear groove. The irregular geometry observed in the wear debris further confirms the occurrence of delamination wear in these conditions.

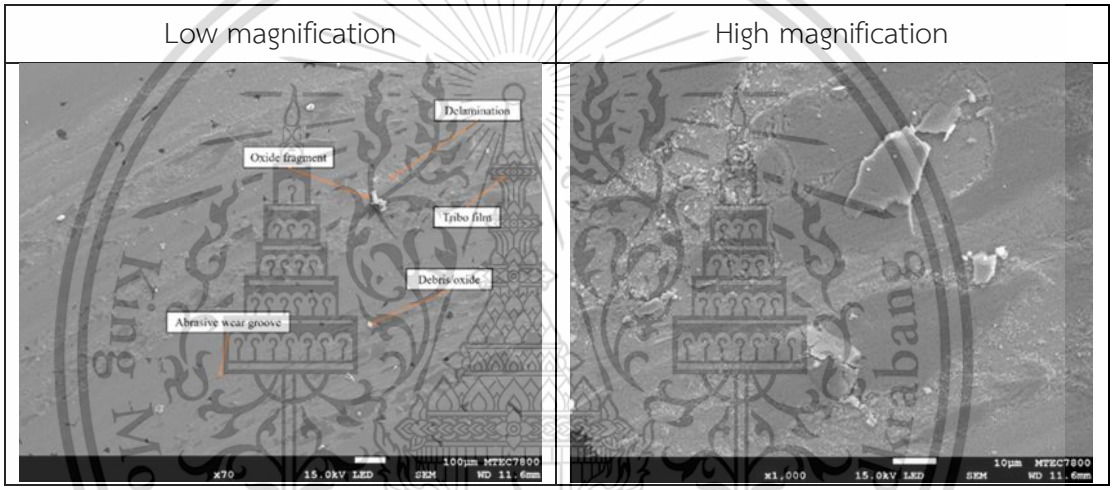

Figure 4. 32 The SEM micrograph of worn surface of sintered Distaloy DH + 4.0 % wt. SiC composites

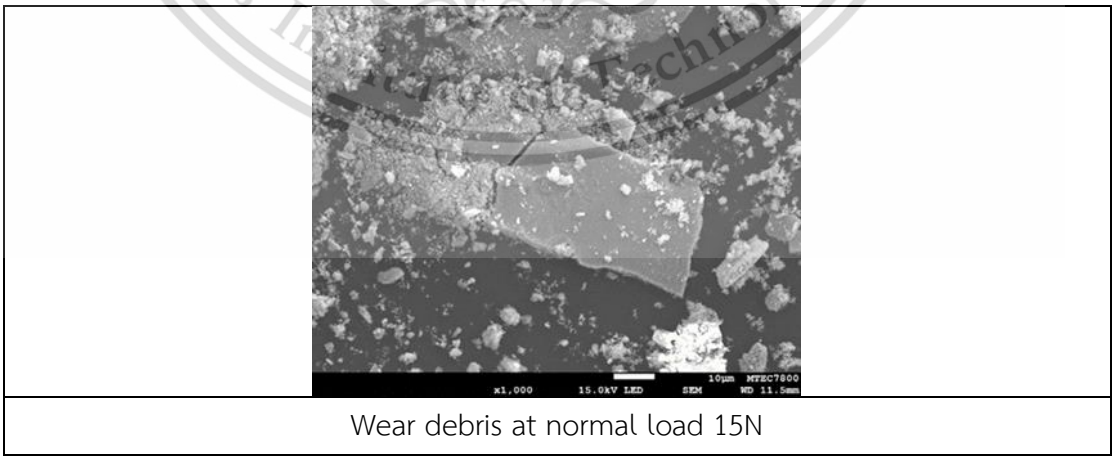

Figure 4. 33 The SEM micrograph of wear debris of sintered Distaloy DH + 4.0 wt. % SiC composites

4.13 WORN SURFACES AND WEAR DEBRIS OF SINTERED DISTALOY DC1 + 4.0 WT. % SIC AT THE NORMAL LOAD 15N.

Figure 4.34 exhibits the SEM micrographs depicting the worn surfaces of sintered Distaloy DC1 + 4.0 wt. % SiC composite under a normal load of 15N. Conversely, figure 4.35 illustrates the wear debris generated from the same composite under identical load conditions. Analysis of the SEM micrographs reveals an increase in surface damage corresponding to an increase in the normal load. At a load of 15N, the worn surface exhibits severe delamination and some abrasive grooves, indicating the presence of wear mechanisms such as delamination and microcracks. Furthermore, the presence of wear debris with a flake-like shape confirms the occurrence of delamination wear.

Low magnification	High magnification
	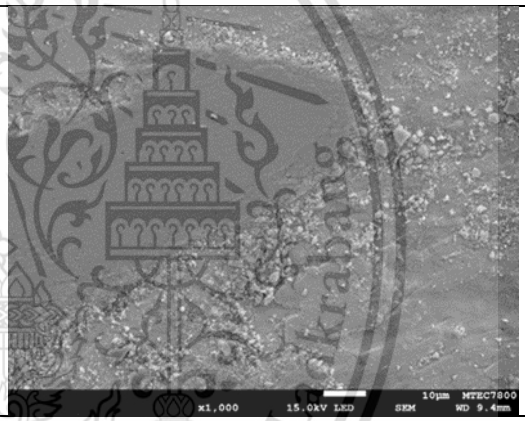

Figure 4. 34 The SEM micrograph of worn surface of sintered Distaloy DC1 + 4.0 % wt. SiC composites

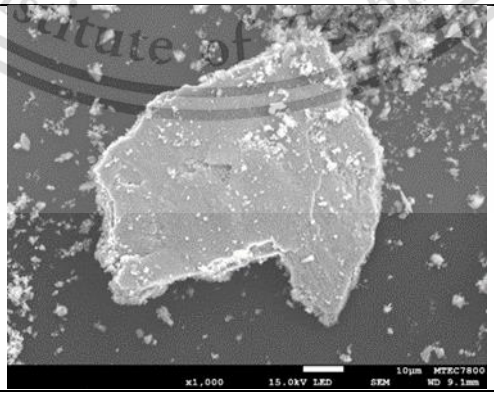

Wear debris at normal load 15N

Figure 4. 35 The SEM micrograph of wear debris of sintered Distaloy DC1 + 4.0 wt. % SiC composites

4.14 WORN SURFACES AND WEAR DEBRIS OF SINTERED DISTALOY SA + 4.0 WT. % SIC AT THE NORMAL LOAD 15N.

Figure 4.36 displays the SEM micrographs illustrating the worn surfaces of sintered Distaloy SA + 4.0 wt. % SiC composite under a normal load of 15N. Conversely, Figure 4.37 exhibits the wear debris generated from the same composite under identical load conditions. Analysis of the worn surface reveals characteristics of delamination and a little of abrasive grooves at 15N, along with the presence of microcracks. Additionally, the debris with flake-like shapes confirms the occurrence of delamination wear. Furthermore, the observed wear mechanisms include delamination and oxide forming.

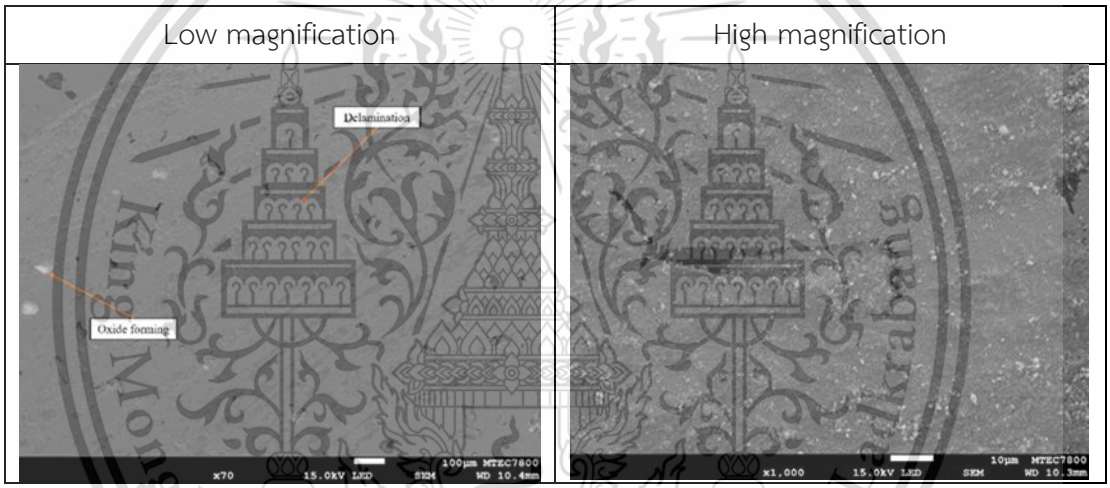

Figure 4. 36 Figure 4.36 The SEM micrograph of worn surface of sintered Distaloy SA + 4.0 % wt. SiC composites

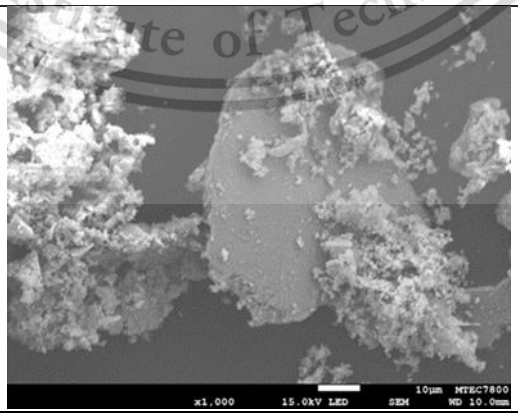

Wear debris at normal load 15N

Figure 4. 37 Figure 4.37 The SEM micrograph of wear debris of sintered Distaloy SA + 4.0 wt. % SiC composites

4.15 WORN SURFACES AND WEAR DEBRIS OF SINTERED DISTALOY AE + 4.0 WT. % SIC AT THE NORMAL LOAD 15N.

Displayed in figure 4.38 are the SEM micrographs depicting the worn surfaces of sintered Distaloy SA + 4.0 wt. % SiC composite under a normal load of 15N. Conversely, figure 4.39 showcases the wear debris resulting from the same composite under identical load conditions. The wear analysis reveals the presence of minor abrasive wear grooves and delamination wear, confirmed by the observation of wear debris with flake-like shapes. Moreover, the observed wear mechanisms include delamination and the presence of black particles.

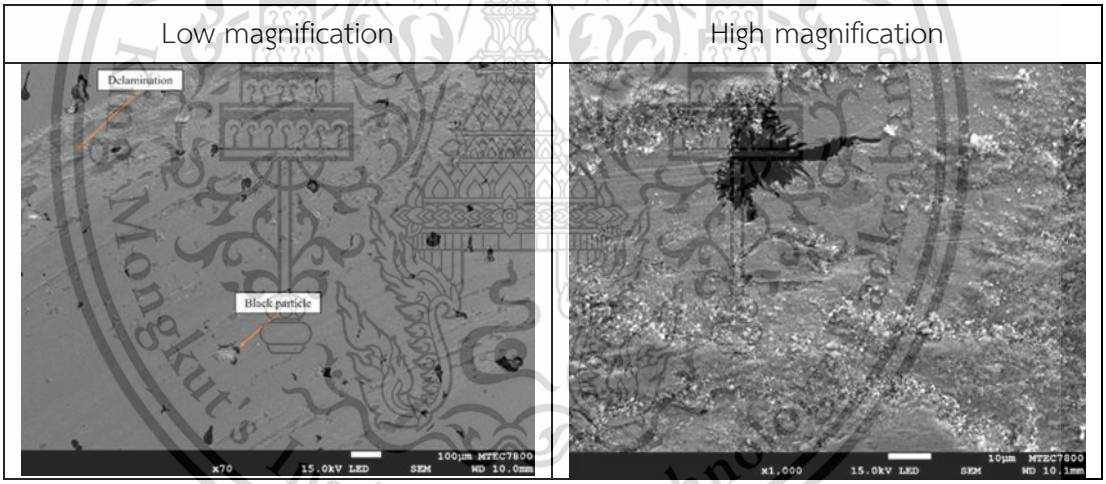

Figure 4. 38 Figure 4.38 The SEM micrograph of worn surface of sintered Distaloy AE + 4.0 % wt. SiC composites

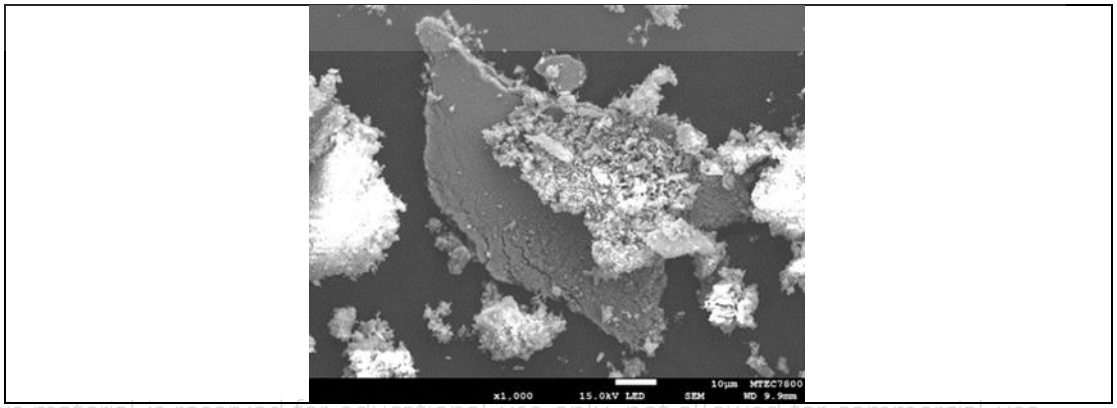

Wear debris at normal load 15N

Figure 4. 39 The SEM micrograph of wear debris of sintered Distaloy AE + 4.0 wt. % SiC composites

4.16 WEAR SCAR DIAMETER OF COUNTER BALL SURFACES ON SINTERED DISTALOY COMPOSITES AT THE NORMAL LOAD 15N.

Figure 4.40 illustrates the results of wear scar diameters on the surfaces of the counter balls. Upon examining the wear scar diameters of the counter ball surfaces under a normal load of 15N, it is evident that the smallest wear scar diameter is observed in sintered Distaloy DC1 + 4.0 wt. % SiC composites, measuring 1.62 mm. Conversely, the largest wear scar diameter is found in sintered Distaloy SA + 4.0 wt. % SiC composites, with a recorded value of 1.76 mm. Additionally, the wear scar diameters for sintered Distaloy DH + 4.0 wt. % SiC composites and sintered Distaloy AE + 4.0 wt. % SiC composites are measured at 1.65 mm and 1.63 mm, respectively. These findings suggest that sintered Distaloy SA + 4.0 wt. % SiC composites exhibit more erosion compared to the other sintered Distaloy composites.

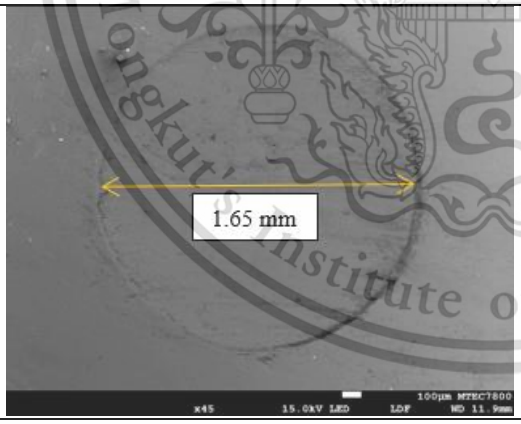	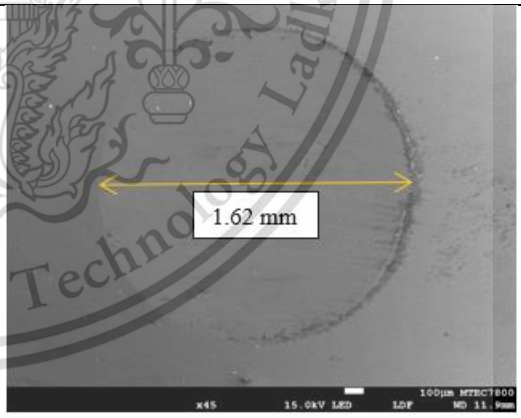
Sintered Distaloy DH + 4.0 wt. % SiC	Sintered Distaloy DC1 + 4.0 wt. % SiC

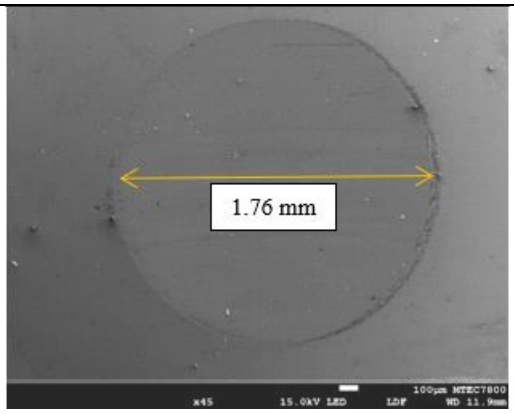

Sintered Distaloy SA + 4.0 wt. % SiC

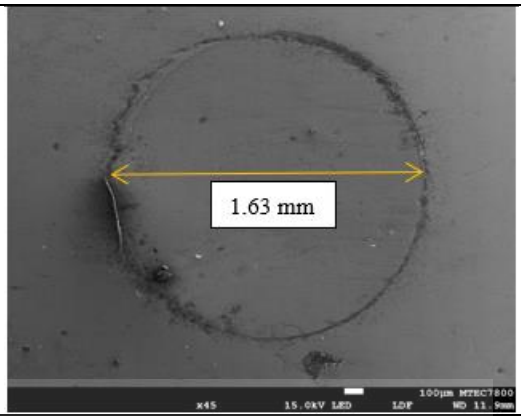

Sintered Distaloy AE + 4.0 wt. % SiC

Figure 4. 40 SEM micrograph of wear scar diameter of counter ball surfaces of all sintered Distaloy composites at the normal load 15N

CHAPTER 5

CONCLUSIONS AND RECOMMENDATIONS

5.1 SUMMARY AND CONCLUSIONS

The current research investigates sintered composites formed from diffusion-bonded powders mixed with 4.0 wt. % SiC ceramic. It examines the microstructure, mechanical properties, and dry sliding wear behavior of sintered Distaloy DH + 4.0 wt. % SiC, sintered Distaloy DC1 + 4.0 wt. % SiC, sintered Distaloy SA + 4.0 wt. % SiC, and sintered Distaloy AE + 4.0 wt. % SiC composites. These Distaloy composites undergo sintering at 1250 ℃ for 45 minutes under cracked ammonia gas, followed by slow cooling at a rate of 0.1 ℃/s. The key findings from the experimental results are summarized as follows:

1. Microstructure: Sintered steels produced from the four diffusion-bonded powders, including Distaloy SA, Distaloy AE, Distaloy DH, and Distaloy DC1, mixed with 4.0 wt. % SiC powder, exhibit microstructures comprising black particles, ferrite halo, pearlite, ausferrite, MA islands and martensite, depending on the chemistry of the diffusion-bonded powders.

2. Microstructure Variations: Sintered Distaloy composites, derived from iron or Fe-based powders mixed with SiC, can display varying microstructures ranging from ferritic-pearlitic ductile iron to dual-phase ADI to ausferrite-MA ADI microstructure, depending on the sintered composites' chemistry.

3. Phase Transformation: Addition of copper (Cu) and nickel (Ni) facilitates low-temperature austenite transformations, leading to the formation of ausferrite and martensite, replacing pearlite. This transformation contributes to overcoming the strength-ductility trade-off dilemma.

4. Mechanical Properties: Sintered Distaloy composites demonstrate promising mechanical properties, exhibiting a synergy between strength and ductility.

5. Coefficient of Friction (COF): Under a normal load of 15N, sintered Distaloy DH + 4.0 wt. % SiC exhibits the highest COF, while sintered Distaloy DC1 + 4.0 wt. % SiC displays the lowest COF under 15N loads. The presence of nickel (Ni) in Distaloy DC1 seems to positively influence the friction coefficient of sintered Distaloy composites.

6. Wear Rate: Among all sintered Distaloy composites, Distaloy SA + 4.0 wt. % SiC exhibits the highest average specific wear rate due to its dual-phase ADI microstructure, while Distaloy AE + 4.0 wt. % SiC displays the lowest average specific wear rate owing to its ausferrite-MA ADI microstructure.

7. Volume Loss: Distaloy SA + 4.0 wt. % SiC demonstrates the highest average volume loss among all sintered Distaloy composites, attributed to its dual-phase ADI microstructure, whereas Distaloy AE + 4.0 wt. % SiC exhibits the lowest average volume loss due to its ausferrite-MA ADI microstructure.

8. Wear Mechanism: Examination of the worn surface and wear debris of sintered Distaloy composites indicates that the major wear mechanism comprises delamination, abrasive, and some oxidative wear. Oxide fragment, tribo film, debris/oxide, micro crack, oxide forming, and black particles are also observed.

9. Surface Damage: The counter ball surfaces rubbing against sintered Distaloy SA + 4.0 wt. % SiC composite demonstrate the highest level of surface damage, despite the sintered Distaloy SA + 4.0 wt. % SiC composite having the smallest hardness value compared to other sintered Distaloy composites.

10. The EPMA results indicated the Ni distribution in sintered material matrices was homogeneous without NRA formation. The diffusion-bonded powders, namely Distaloy DH, Distaloy DC1, Distaloy SA and Distaloy AE powders, can be used to produce sintered 4.0 wt. % SiC-added materials without NRA problem.

5.2 RECOMMENDATIONS AND SUGGESTIONS FOR THE FUTURE STUDY

1. Future studies concerning the present research should involve conducting experiments with varying amounts of SiC addition.

This will enable a comprehensive understanding of the microstructure modification and mechanical properties of sintered composites, facilitating the optimization of SiC content for specific applications. For example, adjusting the SiC content could tailor the composites for use in high-stress automotive components such as engine blocks and transmission gears, where enhanced strength and wear resistance are critical.

2. To comprehend the influence of ambient temperature on the mechanical properties of sintered composites, it is advisable to conduct tensile tests and impact tests at different temperatures during the sintering process.

This approach will help determine the composites' performance in environments with varying temperatures, which is essential for applications in aerospace, where components like turbine blades and structural parts are exposed to extreme temperature variations. Understanding how temperature affects the composites can also inform their use in high-performance engines and braking systems.

3. To gain insights into the effects of applied loads, sliding speeds, and ambient temperature on dry sliding wear, it is recommended to perform the wear test with variations in these parameters.

Performing these tests will provide a detailed understanding of the wear behavior under different operational conditions, which is crucial for industrial applications such as cutting tools, bearings, and machinery components. These insights can lead to the development of materials that maintain their integrity and performance under varying loads and speeds, making them ideal for heavy machinery, mining equipment, and high-speed rail systems.

REFERENCES

[1] Backhaus-Ricoult, M. (1990). Interfaces between SiC and metals. Journal de Physique Colloques, 51, C1-769-C1-774.

[2] Schiepers, R. C. J., van Beek, J. A., van Loo, F. J. J., de With, G. (1993). The interaction between SiC and Ni, Fe, (Fe,Ni) and steel: Morphology and kinetics. Journal of the European Ceramic Society, 11, 211-218.

[3] Pelleg, J. (1999). Reactions in the matrix and interface of the Fe-SiC metal matrix composite system. Materials Science and Engineering A, 269, 225-241.

[4] Tang, W. M., Zheng, Z. X., Ding, H. F., Jin, Z. H. (2002). A study of the solid-state reaction between silicon carbide and iron. Materials Chemistry and Physics, 74, 258-264.

[5] Kalogeropoulou, S., Baud, L., Eustathopoulos, N. (1995). Relationship between wettability and reactivity in Fe/SiC system. Acta Metallurgica et Materialia, 43, 907-912.

[6] Kawanishi, S., Yoshikawa, T., Tanaka, T. (2014). Equilibrium phase relationship between SiC and a liquid phase in the Fe-Si-C System at 1523-1723 K.

[7] Tongsri, R., Vetayanugul, B. (2010). Thermal analysis of Fe-carbide and Fe-C mixtures. Journal of Metals, Materials and Minerals, 20, 45-49.

[8] Klein, A. N., Furlan, K. P., Schroeder, R. M., Hammes, G., Binder, C., Neto, J. B. R., Probst, S. H., de Mello, J. D. B. (2015). Thermodynamic aspects during the processing of sintered materials. Powder Technology, 271, 193-203.

[9] Chakthin, S., Poolthong, N., Tongsri, R. (2008). Effect of reaction between Fe and carbide particles on mechanical properties of Fe-base composite. Advanced Materials Research, 55-57, 357-360.

[10] Nakornkaew, P., Patcharawit, T., Wila, P., Morakotjinda, M., Yotkaew, T., Tosangthum, N., Tongsri, R. (2021). Sintered Fe-Mo-Mn-Si-C alloys. IOP Conf. Series: Materials Science and Engineering, 1137, 012034.

[11] Ruangchai, K., Wiengmoon, A., Morakotjinda, M., Tosangthum, N., Tongsri, R. (2018). Sintered Fe-Mo-Si-C alloys with ductile cast iron microstructure. IOP Conf. Series: Journal of Physics: Conf. Series, 1144, 012099.

[12] Nithimethakul, T., Karin, P., Ohtake, N., Wila, P., Yotkaew, T., Vetayanugul, B., Morakotjinda, M., Tongsri, R. (2021). The effect of molybdenum on the microstructure and mechanical behaviour of the sintered Fe-Mo-Mn-Si-C composite. IOP Conf. Series: Materials Science and Engineering, 1137, 012028.

[13] Fujiki, A. (2001). Present state and future prospects of powder metallurgy parts for automotive applications. Materials Chemistry and Physics, 67, 298-306.

[14] Tan, Z. Q., Zhang, Q., Guo, X. Y., Zhao, W. J., Zhou, C. S., Liu, Y. (2020). New development of powder metallurgy in automotive industry. Journal of Central South University, 27, 1611-1623.

[15] Rahman, M. M., Ariffin, A. K., Nor, S. S. M. (2009). Development of a finite element model of metal powder compaction process at elevated temperature. Applied Mathematical Modelling, 33, 4031-4048.

[16] Bai, Y., Li, L., Fu, L., Wang, Q. (2021). A review on high velocity compaction mechanism of powder metallurgy. Science Progress, 104(2), 1-20.

[17] Hammes, G., Schroeder, R., Binder, C., Klein, A. N., de Mello, J. D. B. (2014). Effect of double pressing/double sintering on the sliding wear of self-lubricating sintered composites. Tribology International, 70, 119-127.

[18] Atkinson, H. V., Davies, S. (2000). Fundamental aspects of hot isostatic pressing: An overview. Metallurgical and Materials Transactions A, 31, 2981-3000.

[19] Ruangchai, K., Wiengmoon, A., Morakotjinda, M., Krataitong, R., Tanprayoon, D., Yotkaew, T., Tosangthum, N., Patakham, U., Tongsri, R. (2017). Microstructure, hardness and wear properties of sintered Fe-Mo-Si-C steels with spheroidal graphite iron/compacted graphite iron-like. Key Engineering Materials, 751, 47-52.

[20] Nithimethakul, T., Karin, P., Ohtake, N., Wila, P., Yodkaew, T., Vetayanugul, B., Morakotjinda, M., Tongsri, R. (2021). The effect of molybdenum on the microstructure and mechanical behaviour of the sintered Fe-Mo-Mn-Si-C composite. IOP Conf. Series: Materials Science and Engineering, 1137, 012028.

[21] Morakotjinda, M., Yotkaew, T., Vetayanugul, B., Wanalerkngam, A., Tongsri, R. (2023). Promotion of ausferrite formation in as-sintered Fe-Mo-Si-C-(Cu) composites due to Cu addition. Materials Chemistry and Physics, 296, 127226.

[22] Kaewkam, T., Kansuwan, P., Ohtake, N., Wila, P., Krataithong, R., Tosangthum, N., Yotkaew, T., Tongsri, R. (2021). Sintered Fe-Ni-Si-C alloys. IOP Conf. Series: Materials Science and Engineering, 1137, 012035.

[23] Bernier, F., Plamondon, P., Baïlon, J.-P., L'Espérance, G. (2011). Microstructural characterisation of nickel rich areas and their influence on endurance limit of sintered steel. Powder Metallurgy, 54, 559-565. https://doi.org/10.1179/1743290111Y.0000000006.

[24] Mousavinasab, S., Blais, C. (2017). Role of microstructure heterogeneity on fatigue crack propagation of low-alloyed PM steels in the as-sintered condition. Metals, 7, 60. https://doi.org/10.3390/met7020060.

[25] Wu, M. W., Hwang, K. S., Huang, H. S., Narasimhan, K. S. (2006). Improvements in microstructure homogenization and mechanical properties of diffusion-alloyed steel compact by the addition of Cr-containing powders. Metallurgical and Materials Transactions A, 37, 2559-2568. https://doi.org/10.1007/BF02586228.

[26] Wu, M. W., Hwang, K. S. (2006). Improved homogenization of Ni in sintered steels through the use of Cr-containing prealloyed powders. Metallurgical and Materials Transactions A, 37, 3577-3585. https://doi.org/10.1007/s11661-006-1052-4.

[27] Morakotjinda, M., Yotkaew, T., Vetayanugul, B., Wanalerkngam, A., Tongsri, R. (2023). Promotion of ausferrite formation in as-sintered Fe-Mo-Si-C-(Cu) composites due to Cu addition. Materials Chemistry and Physics, 296, 127226. https://doi.org/10.1016/j.matchemphys.2022.127226.

[28] Morakotjinda, M., Kongmun, P., Wanalerkngam, A., Tosangthum, N., Yotkaew, T., Kijamnajsuk, S. (2023). Sintered Fe-Mo-Cu-Ni-Si-C composites produced by SiC, nickel, and copper additions to Fe-Mo powder. Silicon, 15, 7995-8008. https://doi.org/10.1007/s12633-023-02641-x.

[29] Online. https://www.iqsdirectory.com/articles/powder-metal-parts/powder-metallurgy.html

[30] Online. https://www.meetyoucarbide.com/application-of-powder-metallurgy-in-automobiles/

[31] Online. https://www.iqsdirectory.com/articles/powder-metal-parts/powder-metallurgy.html

[32] Online. https://www.researchgate.net/figure/Powder-compaction-stages-from-left-to-right-filling-compaction-and-ejection_fig3_352061749

[33] Online. https://www.pm-review.com/introduction-to-powder-metallurgy/sintering-in-the-powder-metallurgy-process/

[34] Online. https://www.metallurgyfordummies.com/time-temperature-transformation-ttt-diagram.html

[35] Online. https://www.researchgate.net/figure/Light-optical-micrograph-of-the-ferrite-pearlite-microstructure-of-this-steel-etched_fig1_233515844

[36] Online. https://www.researchgate.net/figure/Microstructure-of-recrystallized-fraction-in-austenite-of-steel-used-Reheating_fig1_286286336

[37] Online. https://www.researchgate.net/figure/Microstructure-of-pearlite-a-lamellar-mixture-of-ferrite-and-cementite-1_fig1_337125518

[38] Online. https://www.researchgate.net/figure/Microstructure-of-martensite-transformation-in-Fe-31wtNi-002wtC-transformed-by-cooling_fig1_281139841

[39] Online. https://en.wikipedia.org/wiki/Bainite

[40] Online. https://www.researchgate.net/figure/Microstructure-of-pearlite-a-lamellar-mixture-of-ferrite-and-cementite-1_fig1_337125518

[41] Online. https://www.researchgate.net/figure/Magnification-of-the-ausferrite-structure-It-can-be-appreciated-clearly-the-graphite_fig21_44097651

[42] Online. https://www.researchgate.net/figure/The-formation-of-ausferritic-structure-a-Nucleation-of-ferrite-platelets-b_fig4_336879595

[43] Online. https://www.researchgate.net/figure/SEM-micrographs-of-a-bainitic-microstructure-taken-by-two-different-detectors-The-marked_fig1_351878905

[44] Online. https://www.researchgate.net/figure/Lamellar-microstructure-and-alpha-colony-structure-of-the-test-alloy_fig1_257339426

[45] Online. https://www.tribonet.org/wiki/pin-on-disk-test/

[46] Online. https://www.researchgate.net/figure/Typical-curve-of-coefficient-of-friction-vs-time_fig1_341992415

[47] Online. https://www.researchgate.net/figure/Mechanisms-of-wear-in-general-adhesive-wear-abrasive-wear-fatigue-wear-corrosive-wear_fig1_321740989

[48] Online. https://www.substech.com/dokuwiki/doku.php?id=mechanisms_of_wear

[49] Online. https://www.machinerylubrication.com/Read/31928/adhesive-wear

[50] Online. https://www.researchgate.net/figure/Types-of-wear-corrosion-that-contribute-to-TiO-2-nanoparticle-release-after-orthopedic_fig1_318609993

[51] Online. https://www.tribonet.org/wiki/oxidative-wear/

[52] Online. https://www.researchgate.net/figure/Corrosive-and-oxidation-wear-of-structural-members-of-industries_fig10_347464033

[53] Chakthin, S., Poolthong, N., Tongsri, R. (2008). Effect of reaction between Fe and carbide particles on mechanical properties of Fe-base composite. Advanced Materials Research, 55-57, 357-360.

[54] Ruangchai, K., Wiengmoon, A., Morakotjinda, M., Krataitong, R., Tanprayoon, D., Yotkaew, T., Tosangthum, N., Patakham, U., Tongsri, R. (2017). Microstructure, hardness and wear properties of sintered Fe-Mo-Si-C steels with spheroidal graphite iron/compacted graphite iron-like. Key Engineering Materials, 751, 47-52.

[55] Lacaze, J., Sertucha, J., Åberg, L. M. (2016). Microstructure of as-cast ferritic-pearlitic nodular cast irons. ISIJ International, 56, 1606-1615.

[56] Kim, Y. J., Shin, H., Park, H., Lim, J. D. (2008). Investigation into mechanical properties of austempered ductile cast iron (ADI) in accordance with austempering temperature. Materials Letters, 62, 357-360.

[57] Nithimethakul, T., Karin, P., Ohtake, N., Wila, P., Yodkaew, T., Vetayanugul, B., Morakotjinda, M., Tongsri, R. (2021). The effect of molybdenum on the microstructure and mechanical behaviour of the sintered Fe-Mo-Mn-Si-C

composite. IOP Conf. Series: Materials Science and Engineering, 1137, 012028.

[58] Basso, A., Caldera, M., Rivera, G., Sikora, J. (2012). High silicon ductile iron: possible uses in the production of parts with “dual phase ADI” microstructure. ISIJ International, 52, 1130-1134. https://doi.org/10.2355/isijinternational.52.1130.

[59] Sajjadi, S. A., Zebarjad, S. M. (2007). Isothermal transformation of austenite to bainite in high carbon steels. Journal of Materials Processing Technology, 189, 107-113.

[60] Toji, Y., Matsuda, H., Raabe, D. (2016). Effect of Si on the acceleration of bainite transformation by preexisting martensite. Acta Materialia, 116, 250-262.

[61] Kaewkam, T., Kansuwan, P., Ohtake, N., Wila, P., Krataithong, R., Tosangthum, N., Yotkaew, T., Tongsri, R. (2021). Sintered Fe-Ni-Si-C alloys. IOP Conf. Series: Materials Science and Engineering, 1137, 012035. https://doi.org/10.1088/1757-899X/1137/1/012035.

[62] Caballero, F. G., Santofimia, M. J., Capdevila, C., García-Mateo, C., de Andrés, C. G. (2006). Design of advanced bainitic steels by optimisation of TTT diagrams and T0 curves. ISIJ International, 46, 1479-1488.

[63] Kozeschnik, E., Bhadeshia, H. K. D. H. (2008). Influence of silicon on cementite precipitation in steels. Materials Science and Technology, 24, 343-347.

[64] Gao, Y. F., Zhang, W., Shi, P. J., Ren, W. L., Zhong, Y. B. (2020). A mechanistic interpretation of the strength-ductility trade-off and synergy in lamellar microstructures. Materials Today Advances, 8, 100103.

[65] Srivastava, A. K., Patel, N. K., Kumar, B. R., Sharma, A., Ahn, B. (2020). Strength-ductility trade-off in dual-phase steel tailored via controlled phase transformation. Journal of Materials Engineering and Performance, 29, 2783-2791.

[66] Wei, Y., Li, Y., Zhu, L., Liu, Y., Lei, X., Wang, G., Wu, Y., Mi, Z., Liu, J., Wang, H., Gao, H. (2014). Evading the strength-ductility trade-off dilemma in steel through gradient hierarchical nanotwins. Nature Communications, 5, 3580.

[67] Du, X. H., Li, W. P., Chang, H. T., Yang, T., Duan, G. S., Wu, B. L., Huang, J. C., Chen, F. R., Liu, C. T., Chuang, W. S., Lu, Y., Sui, M. L., Huang, E. W. (2020). Dual heterogeneous structures lead to ultrahigh strength and uniform ductility in a Co-Cr-Ni medium-entropy alloy. Nature Communications, 11, 2390.

[68] Wu, S. W., Wang, G., Wang, Q., Jia, Y. D., Yi, J., Zhai, Q. J., Liu, J. B., Sun, B. A., Chu, H. J., Shen, J., Liaw, P. K., Liu, C. T., Zhang, T. Y. (2019). Enhancement of strength-ductility trade-off in a high-entropy alloy through a heterogeneous structure. Acta Materialia, 165, 444-458.

[69] Li, Z., Pradeep, K. G., Deng, Y., Raabe, D., Tasan, C. C. (2016). Metastable high-entropy dual-phase alloys overcome the strength-ductility trade-off. Nature, 534, 227-230.

[70] Guo, W., Su, J., Lu, W., Liebscher, C. H., Kirchlechner, C., Ikeda, Y., Körmann, F., Liu, X., Xue, Y., Dehm, G. (2020). Dislocation-induced breakthrough of strength and ductility trade-off in a non-equiatomic high-entropy alloy. Acta Materialia, 185, 45-54.

[71] Deuis, R. L., Subramanian, C., Yellup, J. M. (1997). Sliding of aluminium composites. Wear, 3538, 415-435.

[72] Zdravecká, E., Tkáčová, J., Ondáč, M. (2014). Effect of microstructure factors on abrasion resistance of high-strength steels. Research in Agricultural Engineering, 60, 115-120. https://doi.org/10.17221/20/2013-rae.

[73] Shaikh, M. B. N., Aziz, T., Arif, S., Ansari, A. H., Karagiannidis, P. G., Uddin, M. (2020). Effect of sintering techniques on microstructural, mechanical and tribological properties of Al-SiC composites. Surfaces and Interfaces, 20, 100598. https://doi.org/10.1016/j.surfin.2020.100598.

APPENDIX A:

ELEMENTAL DISTRIBUTION OF EPMA REPORTS

Elemental distribution of EPMA maps of sintered Distaloy DH + 4.0 wt.% SiC composites

DH-area_abnormal ferrite_AUS-AUS

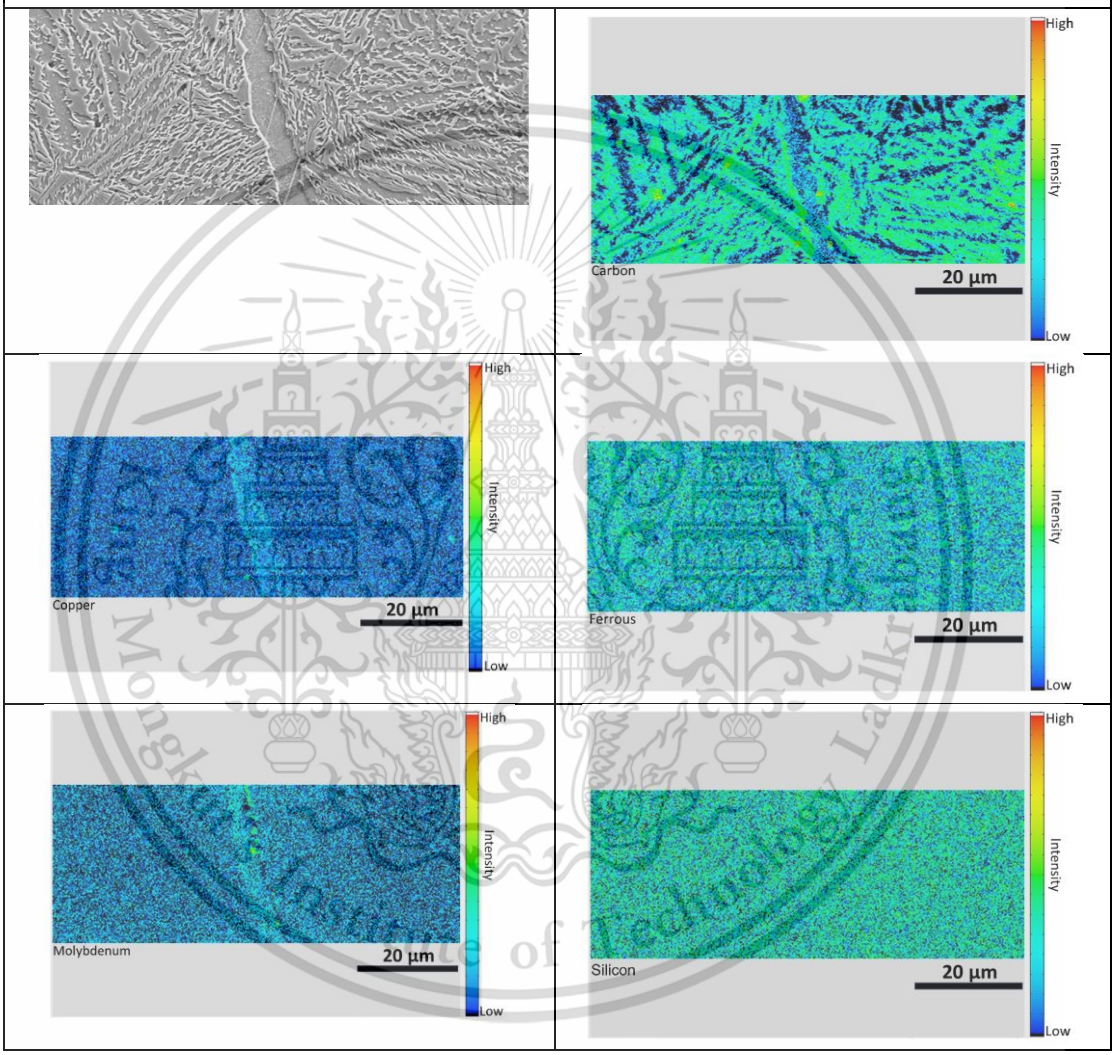

DH-area_AUS-AUS

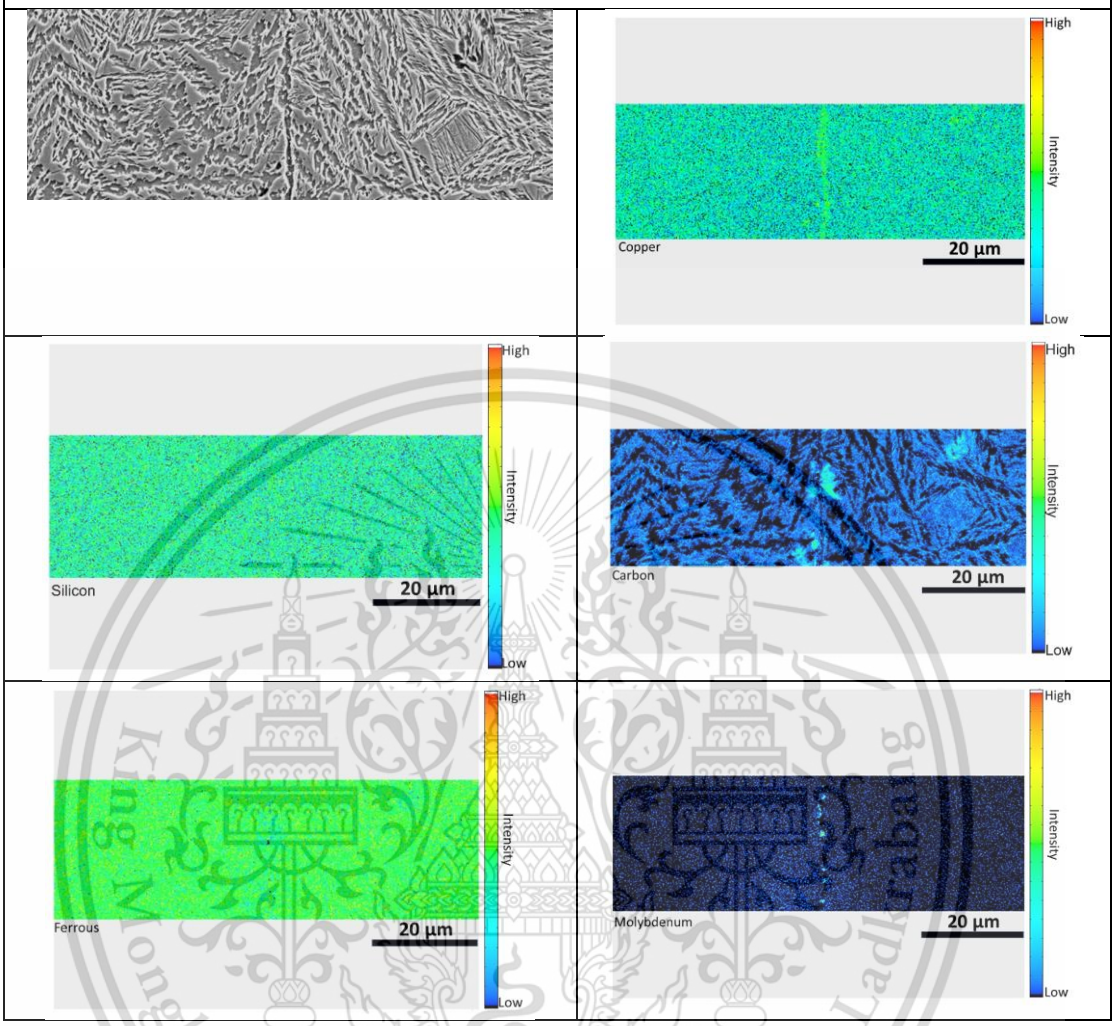

DH-area ferrite halo BP - AUS

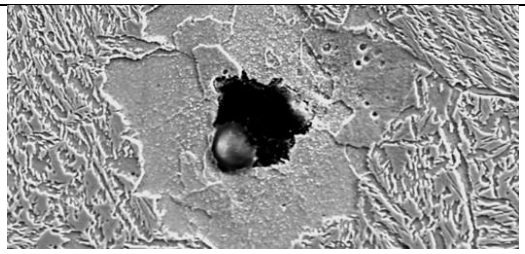

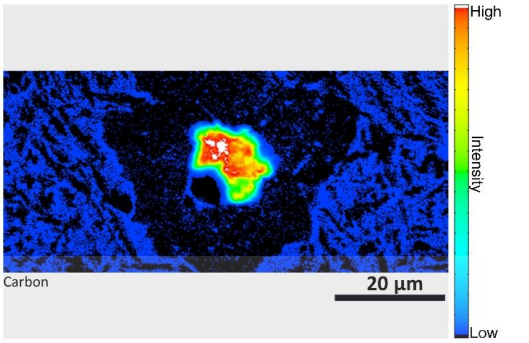

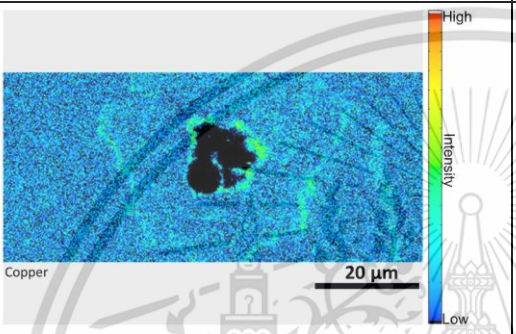

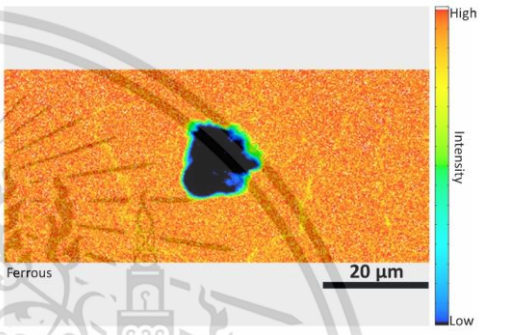

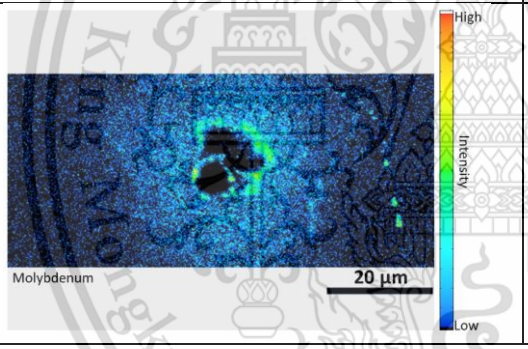

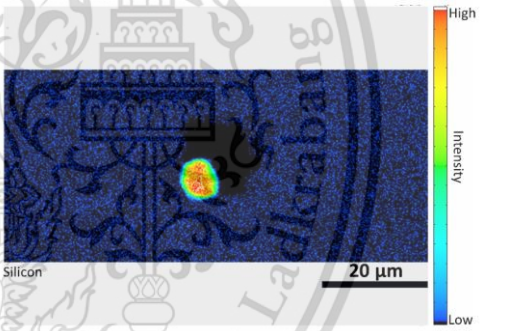

DH-area abnormal ferrite AUS-AUS

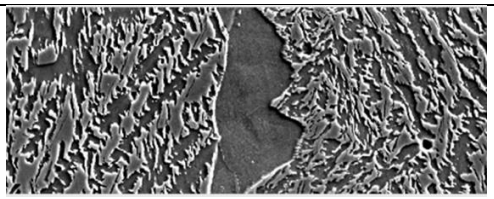

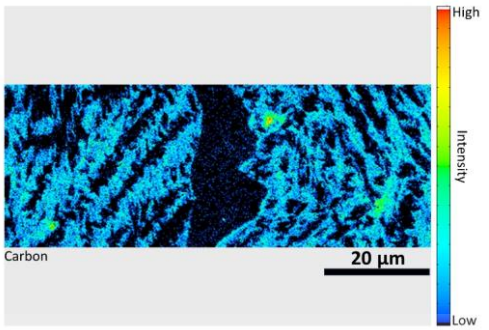

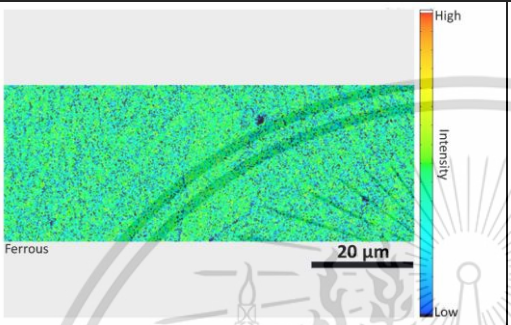

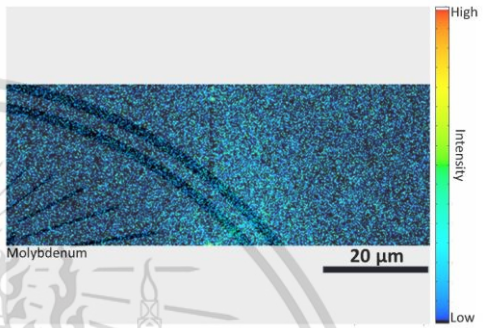

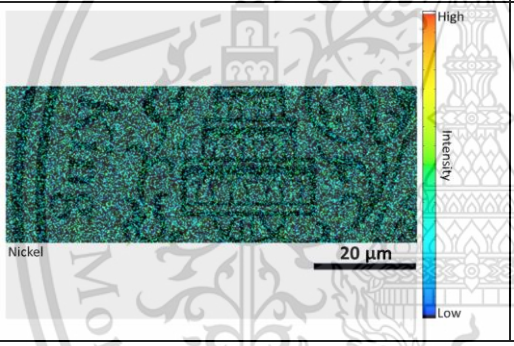

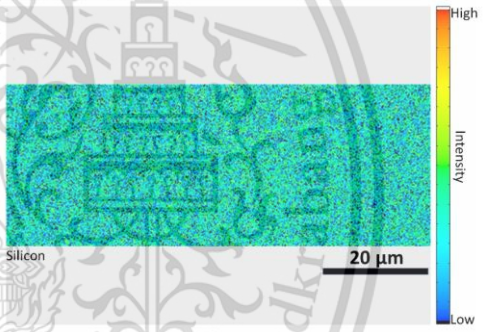

DH-area AUS-AUS

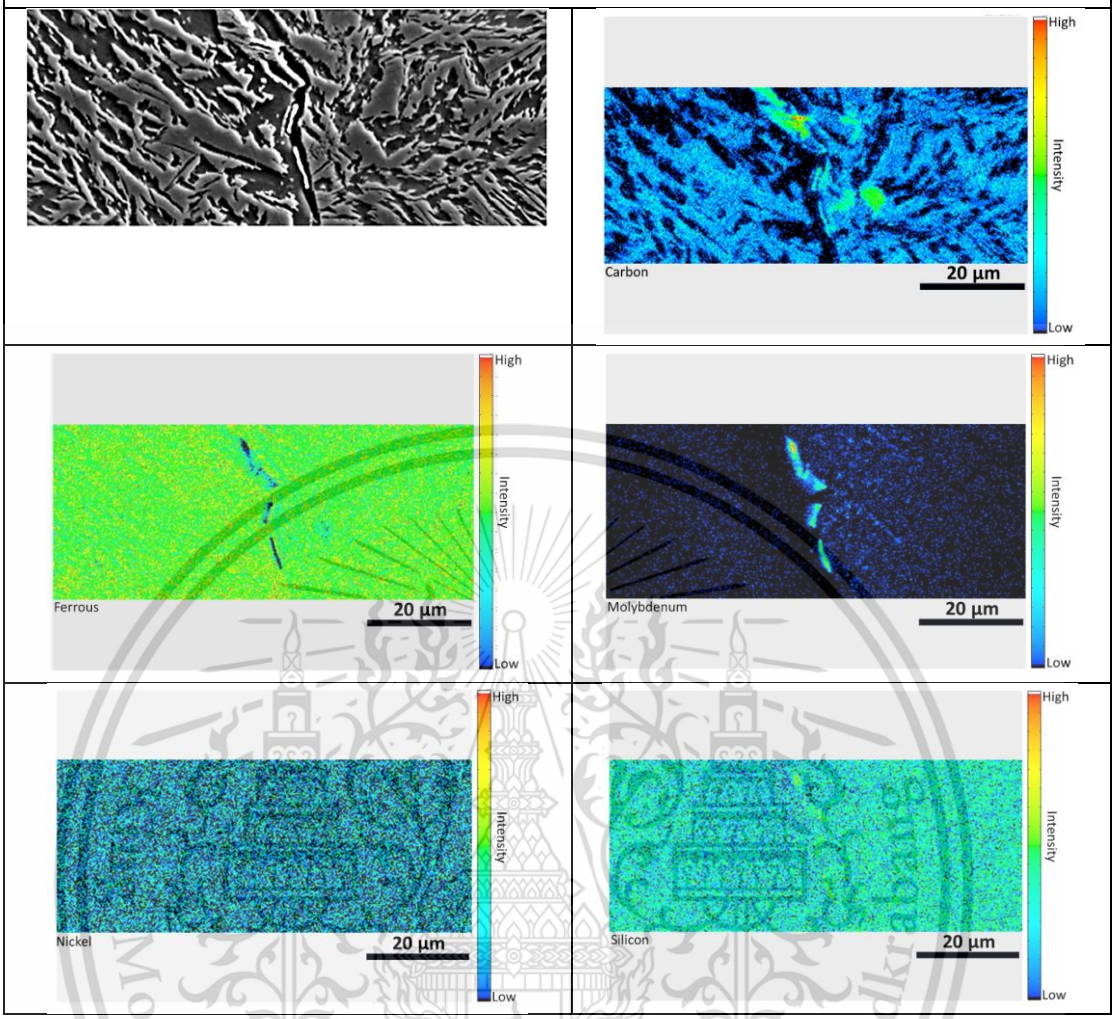

DH-area ferrite halo BP - AUS

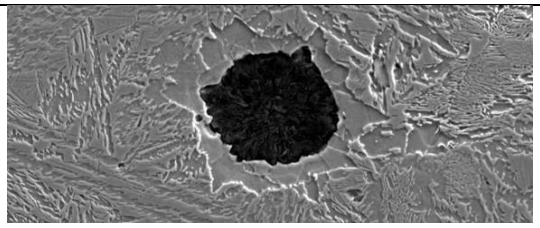

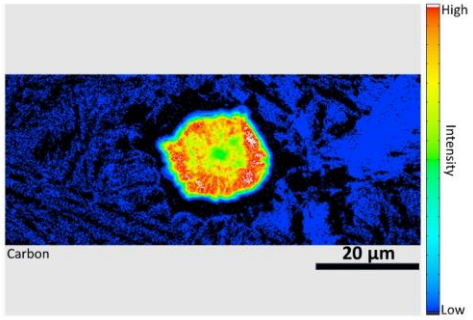

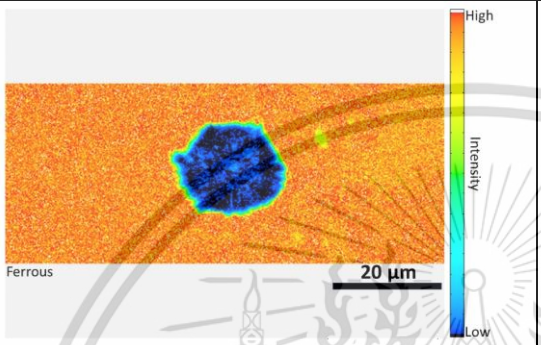

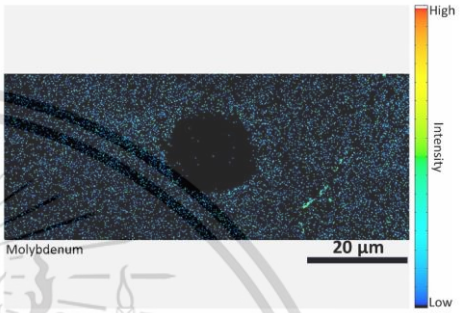

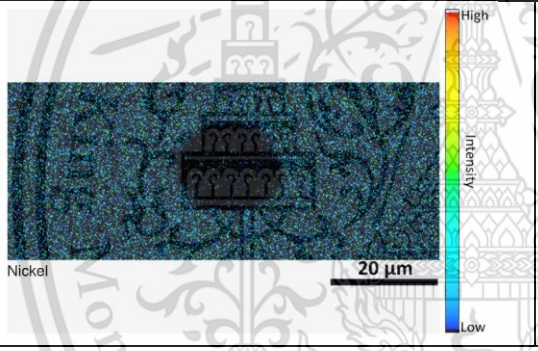

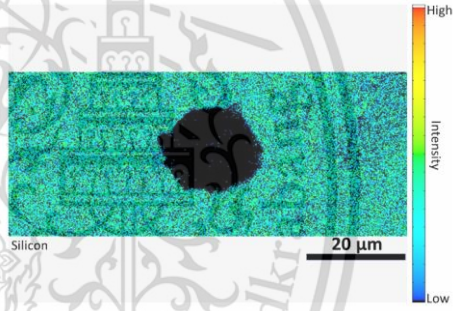

APPENDIX B:

EDS SPECTRUM OF WEAR DEBRIS REPORTS

EDS spectrum of wear debris of sintered Distaloy DH + 4.0 % wt. SiC composites.

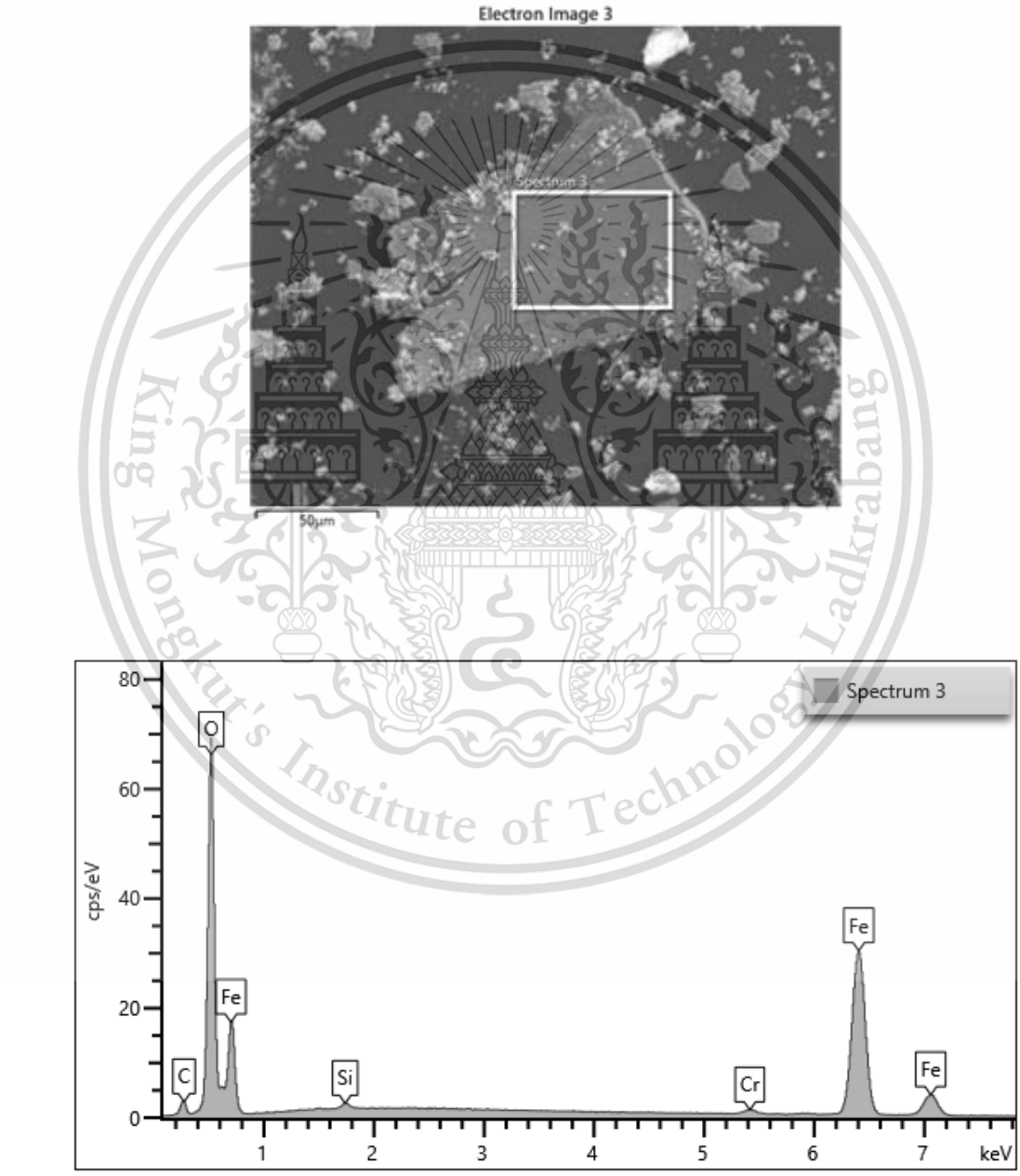

Spectrum 3 (Distaloy DH + 4.0 wt. % SiC)			
Element	Line Type	Wt%	Atomic %
C	K series	4.27	10.04
O	K series	32.79	57.92
Si	K series	0.31	0.31
Cr	K series	0.86	0.47
Fe	K series	61.78	31.26
Total:		100.00	100.00

EDS spectrum of wear debris of sintered Distaloy DC1 + 4.0 % wt. SiC composites.

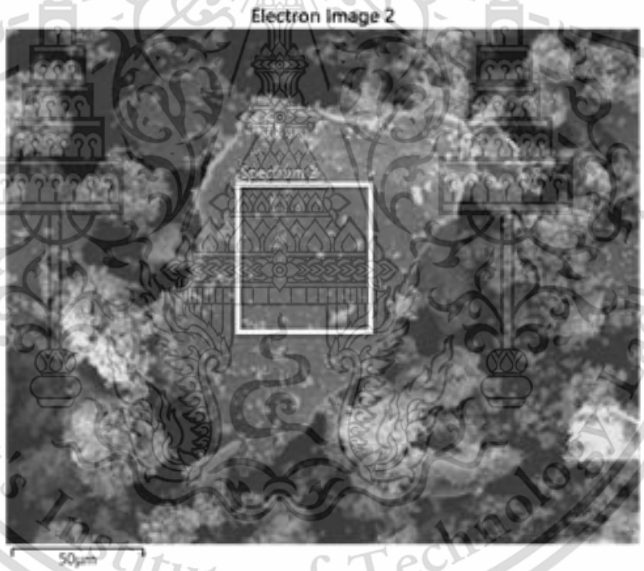

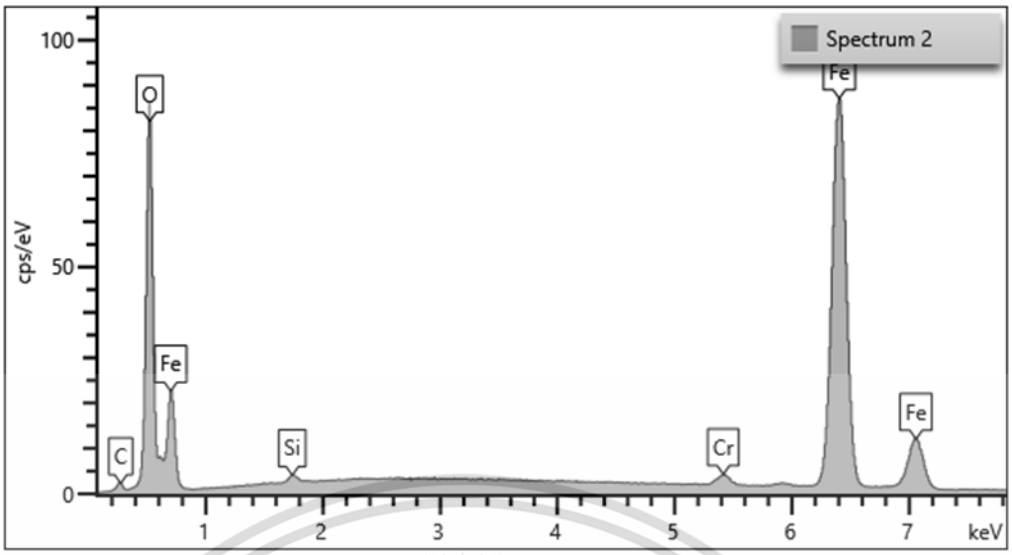

Spectrum 2 (Distaloy DC1 + 4.0 wt. % SiC)			
Element	Line Type	Wt%	Atomic %
C	K series	1.50	4.57
O	K series	18.72	42.87
Si	K series	0.25	0.32
Cr	K series	1.10	0.77
Fe	K series	78.43	51.46
Total:		100.00	100.00

EDS spectrum of wear debris of sintered Distaloy SA + 4.0 % wt. SiC composites.

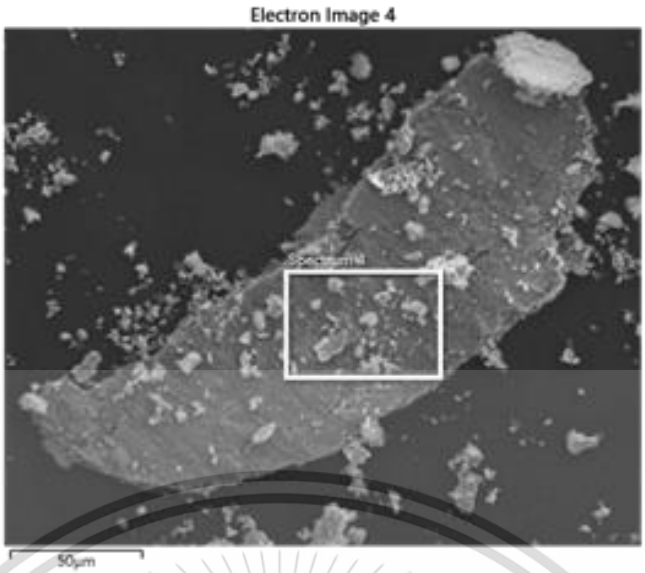

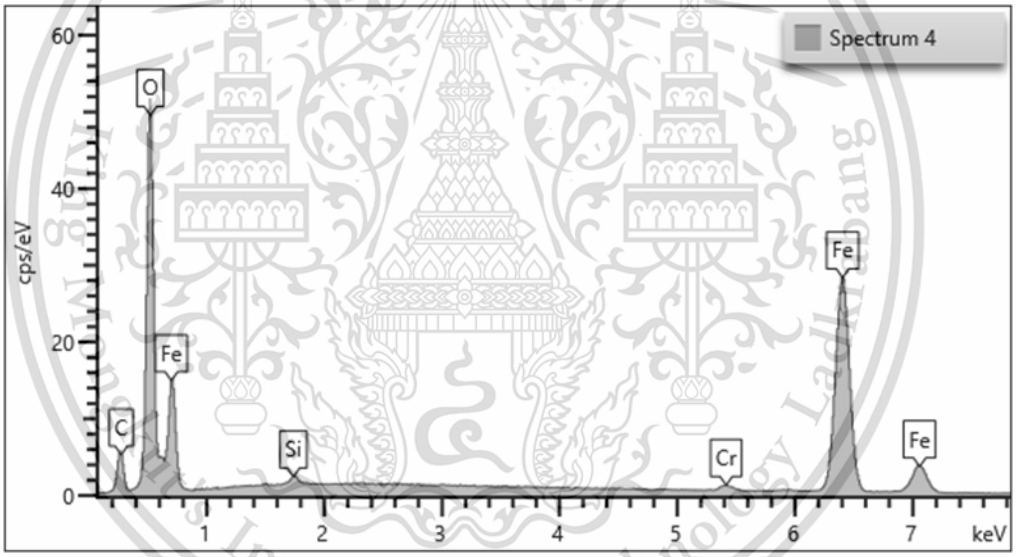

Spectrum 4 (Distaloy SA + 4.0 wt. % SiC)			
Element	Line Type	Wt%	Atomic %
C	K series	9.14	20.57
O	K series	29.25	49.42
Si	K series	0.33	0.32
Cr	K series	0.79	0.41
Fe	K series	60.49	29.28
Total:		100.00	100.00

EDS spectrum of wear debris of sintered Distaloy AE + 4.0 % wt. SiC composites.

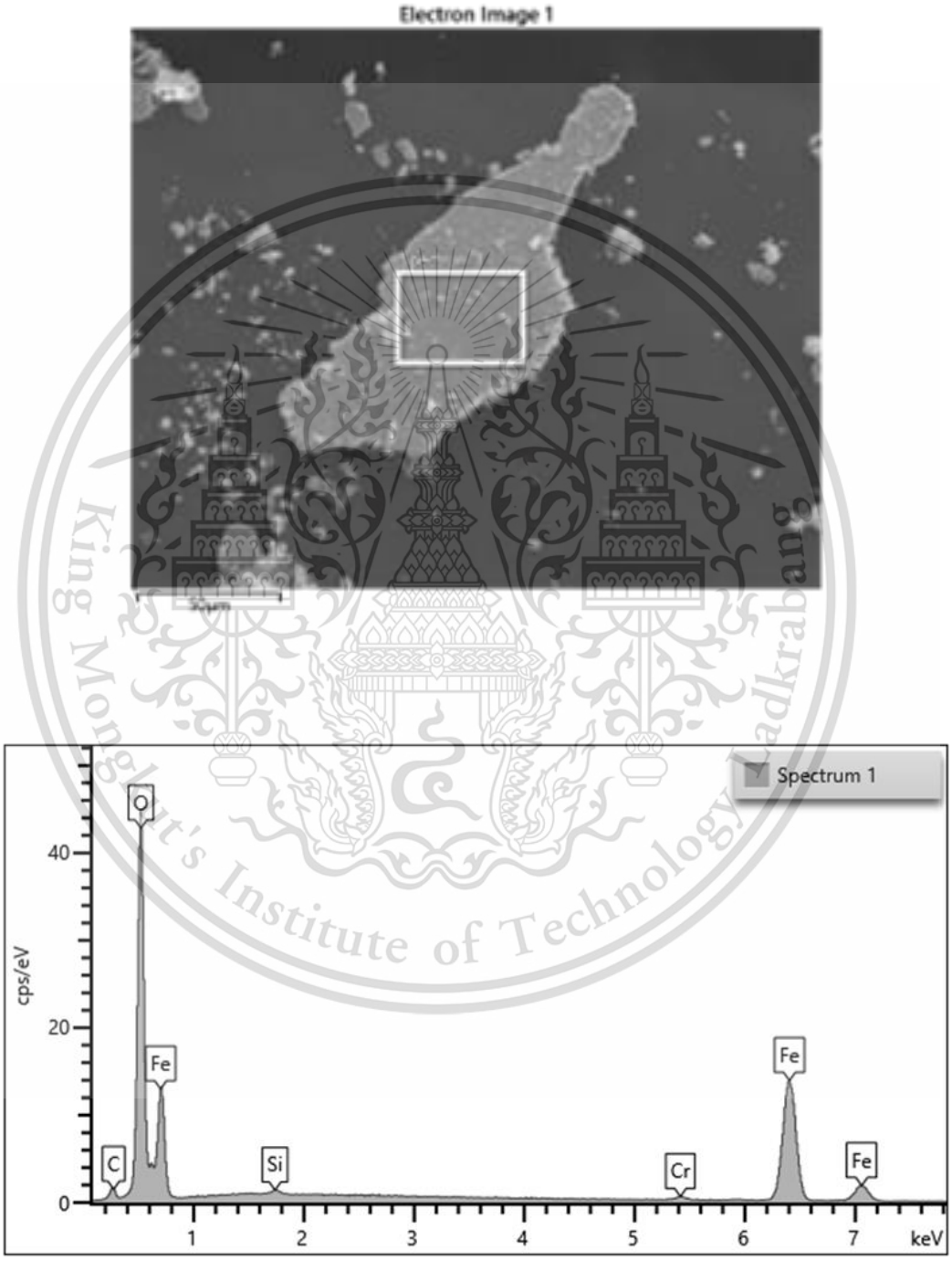

Spectrum 1 (Distaloy AE + 4.0 wt. % SiC)			
Element	Line Type	Wt%	Atomic %
C	K series	3.93	8.60
O	K series	39.17	64.44
Si	K series	0.26	0.24
Cr	K series	0.75	0.38
Fe	K series	55.88	26.33
Total:		100.00	100.00

APPENDIX C:

CONFERENCE PARTICIPATION

The 13th TSME International Conference on Mechanical Engineering
12th – 15th December 2023
Chiang Mai, Thailand

TSME ICOME 2023
Reaching Sustainable Development Goals

AMM0008

Sintered steels with improved ductility produced from diffusion-alloyed powders

A Z Myo[1,*], M Srilomsak[1], M Morakotjinda[2], T Yotkaew[2], N Tosangthum[2], P Wila[2], R Tongsri[2], and K Inaba[3]

[1]School of Engineering, King Mongkut's Institute of Technology Ladkrabang, Chalongkrung Road, Ladkrabang, Bangkok 10520, Thailand
[2]Particulate Materials Processing Technology (PMPT), National Metal and Materials Technology Center, 114 Paholyothin Road, Khlong Nueng, Khlong Luang, Pathumthani 12120, Thailand
[3]Department of Transdisciplinary Science and Engineering, Tokyo Institute of Technology, 2-12-1-I6-5 Ookayama, Meguro-ku, Tokyo, 152-8550, Japan

* Corresponding Author: ruangdt@mtec.or.th

Abstract. Conventional sintered steels have low ductility due to the presence of porosity, inherited from voids at powder particle corners in a green compact. The porosity level can be reduced by using novel processing methods, such as warm compaction, high velocity compaction, and double compaction and double sintering. However, the application of these processes can lead to higher cost of production. A new concept for producing a sintered steel with high strength and improved ductility is proposed to be based on sintered steel matrix modification and porosity reduction. In this work, the addition of 4.0 wt% silicon carbide, instead of graphite, to different diffusion bonded powders, such as Distaloy SA (with composition of Fe-0.50Mo- 1.50Cu-1.75Ni), Distaloy AE (with composition of Fe-0.50Mo-1.50Cu-4.00Ni), Distaloy DH (with composition of Fe-1.47Mo-2.0Cu), and Distaloy DC1 (with composition of 1.50Mo-2.0Ni), led the formation of pore filling particles, known as black particles, and the formation of ausferrite in sintered steel matrix. The pore filling and the presence of ausferrite matrix led to promising tensile strengths with low yield ratios and elongation values of over 5.0 %.

Keywords: Sintering, silicon carbide, austempered ductile iron microstructure, ausferrite, and tensile properties.

1. Introduction

A conventional 'press and sinter process' has been being widely applied for fabricating automotive parts because its productivity is considered as economy-scale and sintered parts require minimal or without machining [1, 2]. However, conventional sintered steels have low ductility due to the presence of porosity, inherited from voids at powder particle corners in a green compact. The porosity level can be reduced by using novel processing methods, such as warm compaction [3], high velocity compaction [4], double compaction and double sintering [5], high isostatic pressing [6]. However, the applications of these

processes can lead to higher cost of production.

The recent discovery of a new approach by tailoring sintered steel chemistry sheds light on enhancement of both strength and ductility of sintered steels. In previous works, it was reported that silicon carbide (SiC) additions with contents of 4.0 to 5.0 wt% to iron (Fe) or Fe-based powders could lead to the formation of ductile iron-like microstructure, whose feature comprised a black particle embedded in ferrite-pearlite matrix [7, 8]. The change of base powder chemistry by increasing molybdenum (Mo) content in Fe-Mo powders led to the formation of novel ductile iron-like microstructure, whose feature comprised a black particle embedded in ferrite, pearlite, and ausferrite matrix [9]. The modification of sintered alloy produced from Fe-0.85Mo + 4.0 wt% SiC mixture by copper (Cu) powder additions also led to the formation of novel austempered ductile iron microstructure, whose feature comprised a black particle embedded in ferrite-ausferrite matrix [10]. When varied alloying nickel (Ni) element contents were employed, novel austempered ductile iron microstructure, whose feature comprised a black particle embedded in ferrite, ausferrite, and martensite matrix was obtained [11]. The results given above provide the assumptions that the use of judicious SiC powder content instead of graphite can lead to the formation of ductile iron family microstructure and the combination of alloying Mo, Cu, Ni, Si and C elements can lead to the formation of as-sintered austempered ductile iron microstructure. To prove such hypothesis, different diffusion bonded powders with compositions given in Table 1 were used in this work.

Table 1. Compositions of Distaloy powders used for this work.

Metal powder	Compositions (wt%)			
	Mo	Cu	Ni	Fe
Distaloy DH	1.47	2.00	-	Balance
Distaloy DC1	1.50	-	2.00	Balance
Distaloy SA	0.50	1.50	1.75	Balance
Distaloy AE	0.50	1.50	4.00	Balance

2. Experimental procedure

The base metal powders employed in this work are given in Table 1. The names of sintered steels were the same as the names of base metal powders. The base metal powders were admixed with 4.0 wt% SiC powder. The powder mixtures were added with 1 wt.% zinc stearate as a lubricant. The powder mixtures were compacted into green tensile test bars with green density of 6.5 g/cm^3. The green tensile test bars were sintered at 1250 ºC for 45 minutes in a vacuum furnace, Schmetz of Germany, at pressure of 1.28×10^{-5} MPa. After sintering, specimens were slowly cooled at the cooling rate of 0.1 °C/s. Specimens for optical microscopy (OM) were prepared according to a standard procedure, including cutting, mounting, grinding (180 to 1200 grit silicon carbide papers), polishing (6, 3, and 1 μm diamond pastes), and etching. The etchants employed in this work was 2 % Nital in ethanol. To understand the effect of alloying elements on microstructural development, the chemical distribution was determined by using electron probe microanalyzer (EPMA) machine (Shimadzu EPMA8050G). Phase identification was carried out by using the X-ray diffraction (XRD) technique. The polished specimens were employed for XRD characterization. XRD was performed by using Rigaku TTRAX III X-ray diffractometer with copper source (wavelength of 1.54 Å) and conditions including step size of 0.2°, time 0.5 s/step and angle of 30-100°. Macrohardness test was carried out on un-etched specimens using 100 kgf load (HRB) with 15 indentations per a specimen. Tensile property of the sintered materials was carried out at room temperature using Instron Universal Instrument.

3. Results and Discussion

3.1. Characterization of experimental sintered steels

The microstructural feature of sintered Distaloy DH (Figure 1a) and Distaloy DC1 (Figure 1c) steels

comprised a black particle embedded in the matrix consisting of ferrite halo, ausferrite and pearlite. The XRD patterns of sintered Distaloy DH (Figure 1b) and Distaloy DC1 (Figure 1d) steels showed strong peaks of face-centered cubic (fcc) crystal structure of γ-austenite, moderate peaks of body-centered cubic (bcc) crystal structure of α-ferrite, and weak peaks of orthorhombic crystal structure of M_3C carbide. The XRD peaks of γ-austenite and α-ferrite confirm the presence of ausferrite, which comprises bainitic ferrite and austenite plates. The XRD peaks of M_3C carbide confirm the presence of pearlite colonies. The matrices of both sintered Distaloy DH and Distaloy DC1 steels, consisting of ferrite halo, pearlite, and ausferrite, indicate that 3 different phase transformations occurr during slow post sintered cooling. They include stable eutectoid transformation of austenite to ferrite halo, metastable eutectoid transformation of austenite to pearlite and austempering transformation of austenite to ausferrite. The formation of ferrite halo by stable eutectoid transformation and that of pearlite by metastable eutectoid transformation in sintered Fe + 5.0% SiC alloy [7], sintered Fe-0.85Mo + 4.0 wt% SiC alloy [8], and sintered Distaloy DH and Distaloy DC1 steels (this work) can follow the mechanisms given for as-cast ferritic-pearlitic ductile irons [12]. However, the formation of ausferrite, as the major microstructural component of sintered Distaloy DH and Distaloy DC1 steels under slow and continuous cooling is the novel phenomenon. The ausferrite formation is strongly dependent on austenite stability because of two reasons. The first one is that the austinite plate, one component of ausferrite, remains stable at room temperature. The second is that the typical ausferrite in an austempered ductile iron forms under isothermal heat treatment in temperature range between pearlite and martensite transformation temperatures or roughly about 300-450 °C [13]. The austenite stability, as indicated by the presence of ausferrite, is related to the combined effect of alloying Mo, Si and C elements in sintered Fe-Mo-Mn- Si-C composites [9]. The presence of Cu, as an austenite stabilizer, in sintered Distaloy DH steel or that of Ni, as an austenite stabilizer, in sintered Distaloy DC1 steel would enhance the austenite stability. Therefore, the ausferrite becomes the dominant microstructural component of the matrices of both sintered Distaloy DH and Distaloy DC1 steels. The microstructural feature of sintered Distaloy SA steel comprised a black particle embedded in the matrix consisting of ferrite halo and ausferrite (Figure 1e). The XRD pattern of this sintered steel showed strong peaks of γ-austenite and α-ferrite (Figure 1f). The microstructural feature of sintered Distaloy AE steel comprised a black particle embedded in the matrix consisting of bainitic ferrite and martensite plates (Figure 1g). The XRD pattern of this sintered steel showed strong peaks of γ-austenite and α- ferrite (Figure 1h). Since the XRD peaks of α-ferrite and α' martensite overlap, only peaks of α-ferrite are labelled in Figure 1h.

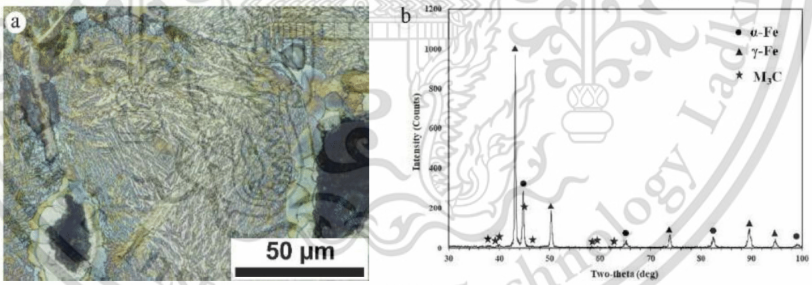

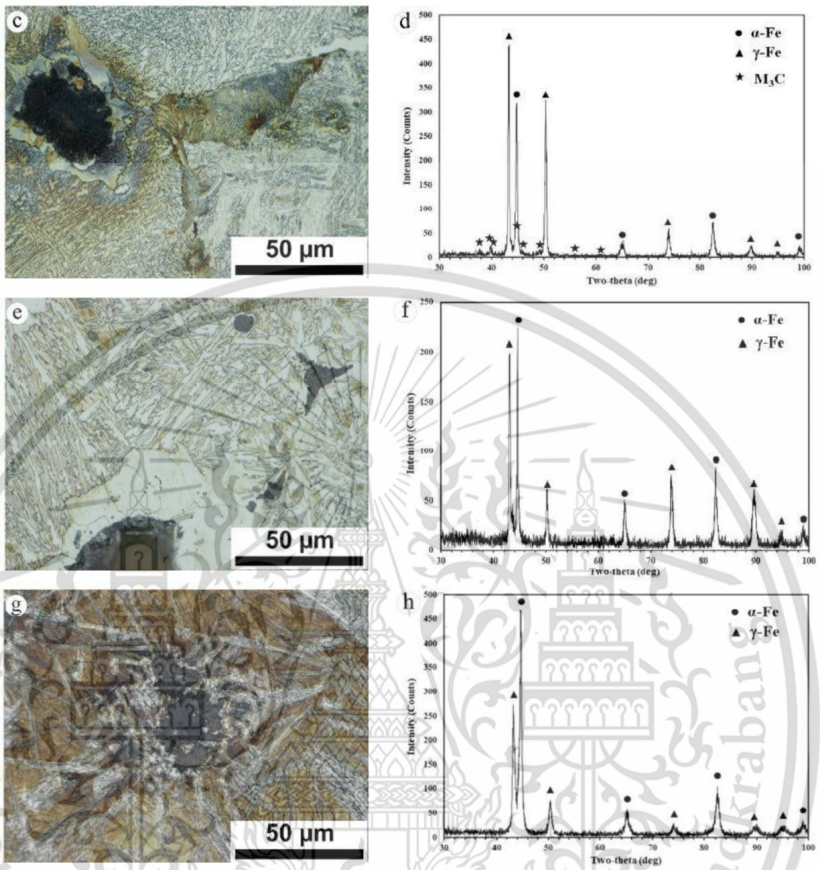

Figure 1. Optical images and XRD patterns of experimental sintered steels; (a, b) Distaloy DH, (c, d) Distaloy DC1, (e, f) Distaloy SA, and (g, h) Distaloy AE.

The microstructure of sintered Distaloy SA steel shows that the combined effect of alloying Mo, Cu, Ni, Si and C elements leads to the total replacement of pearlite by ausferrite. Since the microstructural feature has a black particle embedded in the matrix consisting of ferrite halo and ausferrite, the sintered Distaloy SA steel microstructure can be identified as that of a dual phase austempered ductile iron [14]. The microstructure of sintered Distaloy SA steel consisting of a black particle embedded in the matrix consisting of bainitic ferrite and martensite plates indicates that the stable and metastable eutectoid transformations are totally suppressed. The coexistence of bainitic ferrite and martensite constituents in sintered Distaloy SA steel indicates that its austenite has strong stability due to high Ni content of 4.0 wt%, leading to low temperature bainitic and martensitic phase transformations. When a low-carbon steel is isothermally heat-treated at low temperatures the coexistence of bainitic ferrite and martensite laths is

commonly observed [15-17]. When a high-carbon steel is isothermally heat-treated at low temperatures the bainitic ferrite laths distributed in martensite matrix is commonly observed [18, 19]. The matrix microstructure of sintered Distaloy SA steel resembles that of a high-carbon steel isothermally heat-treated at low temperatures.

3.2 Chemical distribution in experimental sintered steels

EPMA elemental distribution maps were determined in an area around pearlite colonies in sintered Distaloy DH steel (Figure 2). It was found that pearlite colonies had high concentrations of C, Mo and Cu but low concentrations of Fe and Si, compared to surrounding ausferrite. All C, Cu, Fe, Mo, and Si elements showed homogeneous distribution in ausferrite regions. In sintered Distaloy DC1 steel (Figure 3), it was found that pearlite colonies had high C concentration and low Fe and Si concentrations, compared to surrounding ausferrite. Alloying Mo and Ni showed considerably homogenous distribution in both pearlite and ausferrite. Due to the elemental distribution maps given above, it can be implied that pearlite formation required low Si concentration. It is commonly known that judicious Si content can suppress carbide precipitation from austenite [20]. The reason for carbide precipitation inhibition by Si is that the precipitation of para- equilibrium carbide from austenite becomes impossible because of a lack of a driving force for precipitation. The carbide can then only form with the partitioning of silicon, which may take an inordinately long time [21]. The precipitation of M_3C carbide lamellae of pearlite colonies in both sintered Distaloy DH and Distaloy DC1 steels is also attributed to high C concentration in austenite, that leads to carbide precipitation because of a large driving force for the reaction even for para-equilibrium precipitation.

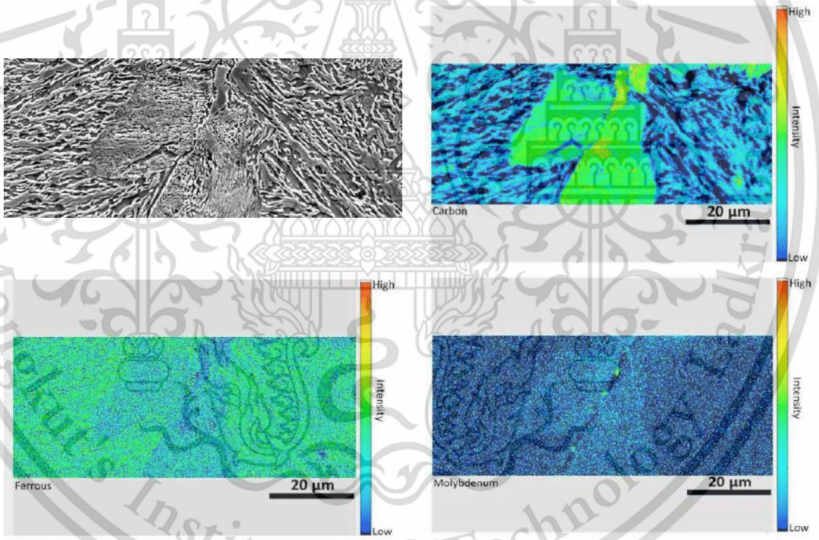

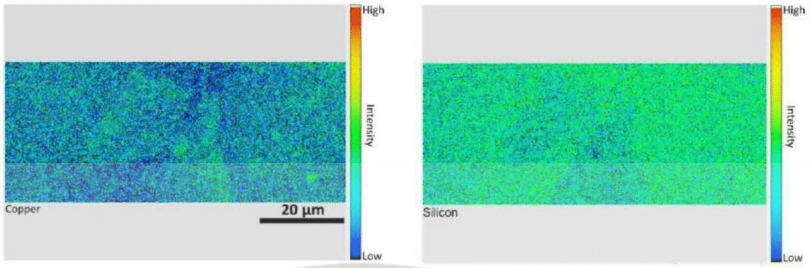

Figure 2. EPMA elemental distribution maps in sintered Distaloy DH steel.

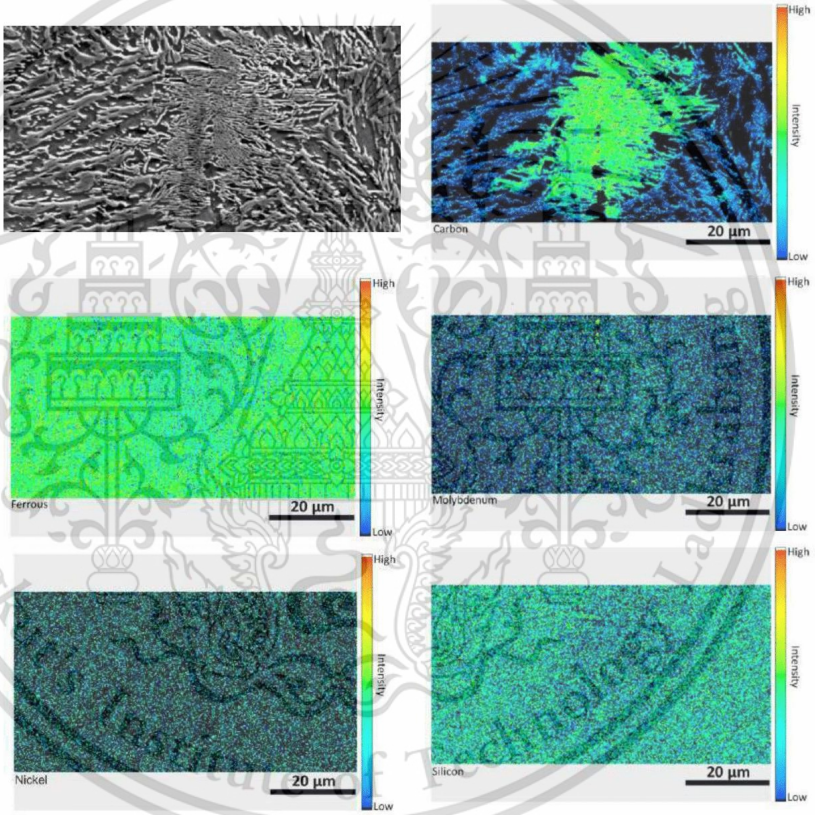

Figure 3. EPMA elemental distribution maps in sintered Distaloy DC1 steel.

3.3 Mechanical property

All experimental sintered steels showed promising mechanical properties, such as ultimate tensile strength (UTS) values of > 700 MPa, yield strength (YS) values of > 250 MPa, elongation values of >5.0 %, and hardness values of > 80 HRB (Figure 4). When tensile strength and elongation are considered, it is found that the increasing order of tensile strength value in experimental sintered steels is that sintered SA < sintered DC1 < sintered DH < sintered AE while the increasing order of elongation value is that sintered DC1 < sintered SA < sintered DH < sintered AE. This indicates that experimental sintered steels have synergy between strength and ductility. In general, a material with high strength suffers low ductility, known strength-ductility trade off dilemma. There are several approaches for evading of strength-ductility trade off dilemma in materials, such as, the dual-phase lamellar microstructure [22], core-shell microstructure [23], nano twinning [24], dual heterogeneous structure [25], heterogeneous structure [26], metastability- engineering strategy [27], and micro-banding and the accumulation of a high density of dislocations in single-phase high-entropy alloys (HEAs) [28]. When the microstructural feature of sintered Distaloy DH, Distaloy DC1, and Distaloy SA steels are considered, the dual-phase lamellar microstructure, alternating bainitic ferrite and austenite plates, seems to be the mechanism for evading of strength- ductility trade off dilemma. However, when compared to the microstructures of the materials having ability to overcome strength- ductility trade off dilemma, as given in references [22-28] the microstructural feature of sintered Distaloy AE steel seems to be the novel microstructural feature showing ability to evade the strength- ductility trade off dilemma.

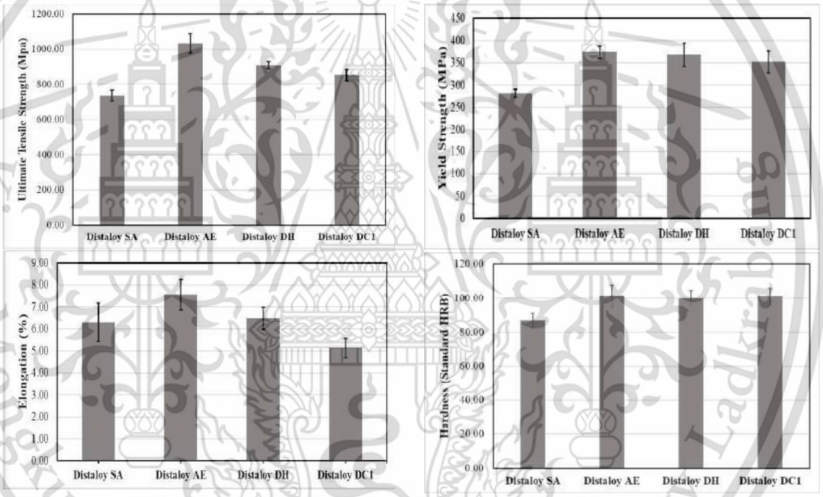

Figure 4. Mechanical properties of experimental sintered steels.

4. Conclusions

The concluding remarks could be drawn from the experimental results as given below.

(1) Slowly cooled sintered steels produced from 4 diffusion bonded powders, such as Distaloy SA (with composition of Fe-0.50Mo-1.50Cu-1.75Ni), Distaloy AE (with composition of Fe-0.50Mo-1.50Cu-4.00Ni), Distaloy DH (with composition of Fe-1.47Mo-2.0Cu), and Distaloy DC1 (with composition of 1.50Mo-2.0Ni) powders, mixed with 4.0 wt % SiC powder had microstructures consisting of black particle, ferrite halo, pearlite, ausferrite and martensite, depending on chemistry

of diffusion bonded powders.

(2) These sintered steels exhibited promising mechanical properties with synergy of strength and ductility.

5. Acknowledgements

The first author (A. Z. Myo) is grateful for financial support from National Science and Technology Development Agency (NSTDA) TAIST scholarships. This work is financially supported via the project 'Design and manufacturing of replacement parts for railway applications (P1951261)' under NSTDA, Pathum Thani, Thailand. Technical supports are obtained from National Metal and Materials Technology Center (MTEC), Pathum Thani, Thailand.

6. References

[1] Fujiki, A. (2001). Present state and future prospects of powder metallurgy parts for automotive applications. *Materials Chemistry and Physics, 67,* 298-306.

[2] Tan, Z. Q., Zhang, Q., Guo, X.Y., Zhao, W.J., Zhou, C. S., Liu, Y. (2020) New development of powder metallurgy in automotive industry. *Journal of Central South University, 27,* 1611-1623.

[3] Rahman, M. M., Ariffin, A. K., Nor S. S. M. (2009). Development of a finite element model of metal powder compaction process at elevated temperature. *Applied Mathematical Modelling, 33*, 4031-4048.

[4] Bai, Y., Li, L., Fu, L., Wang, Q. (2021). A review on high velocity compaction mechanism of powder metallurgy. *Science Progress, 104*(2), 1-20.

[5] Hammes, G., Schroeder, R., Binder, C., Klein, A. N., de Mello, J. D. B. (2014). Effect of double pressing/double sintering on the sliding wear of self-lubricating sintered composites. *Tribology International, 70*, 119-127.

[6] Atkinson, H. V., Davies, S. (2000). Fundamental aspects of hot isostatic pressing: An overview. *Metallurgical and Materials Transactions A, 31*, 2981-3000.

[7] Chakthin, S., Poolthong, N., Tongsri, R. (2008). Effect of reaction between Fe and carbide particles on mechanical properties of Fe-base composite. *Advanced Materials Research, 55-57,* 357-360.

[8] Ruangchai, K., Wiengmoon, A., Morakotjinda, M., Krataitong, R., Tanprayoon, D., Yotkaew, T., Tosangthum, N., Patakham, U., Tongsri, R. (2017). Microstructure, hardness and wear properties of sintered Fe-Mo-Si-C steels with spheroidal graphite iron/compacted graphite iron-like. *Key Engineering Materials, 751*, 47-52.

[9] Nithimethakul, T., Karin, P., Ohtake, N., Wila, P., Yodkaew, T., Vetayanugul, B., Morakotjinda, M., Tongsri, R. (2021). The effect of molybdenum on the microstructure and mechanical behaviour of the sintered Fe-Mo-Mn-Si-C composite. *IOP Conf. Series: Materials Science and Engineering, 1137,* 012028.

[10] Morakotjinda, M., Yotkaew, T., Vetayanugul, B., Wanalerkngam, A., Tongsri, R. (2023). Promotion of ausferrite formation in as-sintered Fe-Mo-Si-C-(Cu) composites due to Cu addition. *Materials Chemistry and Physics, 296*, 127226.

[11] Kaewkam, T., Kansuwan, P., Ohtake, N., Wila, P., Krataithong, R., Tosangthum, N., Yotkaew, T., Tongsri, R. (2021). Sintered Fe-Ni-Si-C alloys. *IOP Conf. Series: Materials Science and Engineering, 1137*, 012035.

[12] Lacaze, J., Sertucha, J., Åberg, L. M. (2016). Microstructure of as-cast ferritic-pearlitic nodular cast irons. *ISIJ International, 56,* 1606-1615.

[13] Kim, Y. J., Shin, H., Park, H., Lim, J. D. (2008). Investigation into mechanical properties of austempered ductile cast iron (ADI) in accordance with austempering temperature. *Materials Letters, 62*, 357-360.

[14] Basso, A., Caldera, M., Massone, J. (2015). Development of high silicon dual phase austempered ductile iron. *ISIJ International, 55,* 1106-1113.

[15] Samanta, S., Biswas, P., Giri, S., Singh, S. B., Kundu, S. (2016). Formation of bainite below the MS temperature: Kinetics and crystallography. *Acta Materialia, 105*, 390-403.

[16] Rampelberg, C., Allain, S. Y. P., Geandier, G., Teixeira, J., Lebel, F., Sourmail, T. (2021). Carbide- free bainite transformations above and below martensite start temperature investigated by in-situ high- energy X-Ray diffraction. *JOM, 73*, 3181-3194.

[17] Łukaszewicz, G., Szczygieł, M., Węsierska-Hinca, M., Chmielarz, K., Wierzbicka, E., Wasiak, K. (2023). Interrupted quenching and bainitising below Ms temperature of EN X37CrMoV5-1 hot-work tool steel: Bainitic transformation kinetics, microstructure and mechanical properties. *Materials Science and Engineering*

A, 869, 144740.

[18] Sajjadi, S. A., Zebarjad, S. M. (2007). Isothermal transformation of austenite to bainite in high carbon steels. *Journal of Materials Processing Technology, 189*, 107-113.

[19] Toji, Y., Matsuda, H., Raabe, D. (2016). Effect of Si on the acceleration of bainite transformation by preexisting martensite. *Acta Materialia, 116*, 250-262.

[20] Caballero, F. G., Santofimia, M. J., Capdevila, C., García-Mateo, C., de Andrés, C. G. (2006). Design of advanced bainitic steels by optimisation of TTT diagrams and T_0 curves. *ISIJ International, 46*, 1479-1488.

[21] E. Kozeschnik, E., Bhadeshia, H.K.D.H. (2008). Influence of silicon on cementite precipitation in steels. *Materials Science and Technology, 24*, 343-347.

[22] Gao, Y. F., Zhang, W., Shi, P. J., Ren, W. L., Zhong, Y. B. (2020). A mechanistic interpretation of the strength-ductility trade-off and synergy in lamellar microstructures. *Materials Today Advances, 8*, 100103.

[23] Srivastava, A. K., Patel, N. K., Kumar, B. R., Sharma, A., Ahn, B. (2020). Strength-ductility trade- off in dual-phase steel tailored via controlled phase transformation. *Journal of Materials Engineering and Performance, 29,* 2783-2791.

[24] Wei, Y., Li, Y., Zhu, L., Liu, Y., Lei, X., Wang, G., Wu, Y., Mi, Z., Liu, J., Wang, H., Gao, H. (2014). Evading the strength-ductility trade-off dilemma in steel through gradient hierarchical nanotwins. *Nature Communications, 5*, 3580.

[25] Du, X. H., Li, W. P., Chang, H. T., Yang, T., Duan, G. S., Wu, B. L., Huang, J.C., Chen, F. R., Liu, C. T., Chuang, W. S., Lu, Y., Sui, M. L., Huang, E.W. (2020). Dual heterogeneous structures lead to ultrahigh strength and uniform ductility in a Co-Cr-Ni medium-entropy alloy. *Nature Communications, 11,* 2390.

[26] Wu, S. W., Wang, G., Wang, Q., Jia, Y. D., Yi, J., Zhai, Q. J., Liu, J. B., Sun, B. A., Chu, H. J., Shen, J., Liaw, P. K., Liu, C. T., Zhang, T.Y. (2019). Enhancement of strength-ductility trade-off in a high-entropy alloy through a heterogeneous structure. *Acta Materialia, 165*, 444-458.

[27] Li, Z., Pradeep, K. G., Deng, Y., Raabe, D., Tasan, C. C. (2016). Metastable high-entropy dual- phase alloys overcome the strength-ductility trade-off. Nature 534 (2016) 227-230.

[28] Guo, W., Su, J., Lu, W., Liebscher, C. H., Kirchlechner, C., Ikeda, Y., Körmann, F., Liu, X., Xue, Y., Dehm, G. (2020). Dislocation-induced breakthrough of strength and ductility trade-offin a non- equiatomic high-entropy alloy. *Acta Materialia, 185,* 45-54.

International Conference on Materials Processing Technology 2023
November 23-24, 2023 · Bangkok · Thailand

MFT-14

Ausferrite promotion in sintered low molybdenum containing alloy by mutual copper and nickel addition

Aung Zaw Myo [1], Mek Srilomsak [1], Kazuaki Inaba [2], Preeya Nakornkaew [3], Monnapas Morkotjinda [3], Nattaya Tosangthum [3], Thanyaporn Yotkaew [3], and Ruangdaj Tongsri [3]*
[1]Automotive and Advanced Transportation Engineering Program, Department of Mechanical Engineering, School of Engineering, King Mongkut's Institute of Technology Ladkrabang
[2]Department of Transdisciplinary Science and Engineering, Tokyo Institute of Technology
[3]Particulate Materials Processing Technology Laboratory (PMPT)
Thailand National Metal and Materials Technology Center (MTEC)
National Science and Technology Development Agency (NSTDA)
Corresponding Author E-mail: ruangdt@mtec.or.th

Sintered alloys, produced from iron (Fe) or Fe-based powders mixed with a proper amount of silicon carbide (SiC), exhibit microstructures similar to those of cast ductile irons. Previous work showed that sintered alloys, produced from Fe-Mo powders with different molybdenum (Mo) contents, could have different portions of ausferrite in addition to ferrite-pearlite matrix when Mo contents were high enough. The formation of ausferrite in sintered alloys is due to transformation of remaining austenite at low temperatures. The austenite stability is the key factor for ausferrite transformation. Because of such reason, it is hypothesized that it is possible for ausferrite to form in sintered alloys produced from low Mo containing Fe-based powders by adding austenite stabilizers. In this work, 3 different sintered alloys, such as (1) Fe-Mo-Mn+ SiC, (2) Fe-Mo + SiC + 1.5Cu + 1.75Ni, and (3) Fe-Mo + SiC + 1.5Cu + 4.0 Ni alloys were produced by sintering at 1250 ºC and slow cooling in a furnace. It was found that mutual copper (Cu) and nickel (Ni) addition led to low temperature austenite transformations resulting in formations of ausferrite and martensite that totally replaced pearlite. The formation of ausferrite and martensite-austenite (MA) structure led to evading the strength-ductility trade-off dilemma.

Keywords: Sintering / Austenite stabilizer / Ausferrite / Strength / Ductility

Introduction

In general, the increase of strength is usually accompanied by ductility loss in metal alloys, known as the strength-ductility trade-off dilemma. Recently, there are several approaches to evade the strength-ductility trade off dilemma in metal alloys. In the dual-phase lamellar microstructures, failures are preceded by necking in the hard phase, the growth of which is significantly confined and suppressed by the surrounding soft phase [1]. The core-shell microstructure constituting martensite core and ferrite shell in a matrix was claimed to show ductility increase at high martensite fractions [2]. Cylindrical twinning-induced plasticity steel samples, with gradient nanotwinned structure along the radial direction, showed high yielding strength without reduction in ductility [3], A medium-entropy alloy, with dual heterogeneous structure consisting of heterogeneous matrix with both coarse grains (10~30 μm) and ultra-fine grains (0.5~2 μm), together with heterogeneous L12-structured nanoprecipitates ranging from several to hundreds of nanometers, showed ultra-high strength and sufficient ductility [4]. In the heterogeneous structuring method employed in high-entropy alloys [5], evading the strength-ductility trade-off is due to the microstructure comprising non-recrystallized and recrystallized grains arranged in complex heterogeneous structures with a characteristic dimension spanning from the submicron scale to the coarse-sized scale. The metastability-engineering strategy was applied to nanostructured bulk high-entropy alloys with multiple compositionally equivalent high-entropy phases [6]. The introduction of micro-banding and the accumulation of a high density

of dislocations to single-phase high-entropy alloys also led to evading strength-ductility trade-off dilemma [7].

The traditional powder metallurgy involves heat treatment consisting of powder compact heating, sintering (austenitization) and cooling steps. The common microstructure of sintered carbon steels inherited from powder metallurgical processes often contains porosities, known as the crack initiator and ductility reducer, and matrices with phase transformation products, such as ferrite and carbides. However, it was observed that the microstructures of some sintered alloys, produced from Fe-0.85Mo-0.15Mn + 4.0 wt. % SiC and Fe-1.50Mo-0.15Mn + 4.0 wt. % SiC, showed microstructures consisting of black particles embedded in the matrix of ferrite, pearlite and ausferrite [8]. The sintered Fe-Ni-Si-C alloys, produced from Fe-Ni base powders + 4.0 wt. % SiC, also showed similar microstructures but with higher fractions of ausferrite and martensite-austenite (MA) structures in the matrices [9]. Interestingly, due to such microstructures, the sintered Fe-Ni-Si-C alloys showed increases of tensile strengths and elongation values with increasing ausferrite and MA fractions.

Since the ausferrite structure, comprising austenite (soft phase) and bainitic ferrite (hard phase) plates, and the MA structure, comprising austenite (soft phase) and martensite (hard phase) plates, can be considered as the dual-phase lamellar microstructure it is assumed that these microstructural features can evade the strength-ductility trade-off dilemma as given elsewhere [1]. In this article, experimental sintered alloys, such as Fe-Mo + SiC, (2) Fe-Mo + SiC + 1.5Cu + 1.75Ni, and (3) Fe-Mo + SiC + 1.5Cu + 4.0 Ni alloys, were produced and tested for validation of the assumption.

Experimental

Materials preparation

The base metal powders used in this investigation included pre-alloyed Fe-0.50Mo-0.15Mn (ATOMET4001 from Rio Tinto Metal Powders of Canada), diffusion alloyed Fe-0.5Mo-1.5Cu-2.0Ni (Distaloy SA of Hoganas of Sweden), and Fe-0.5Mo-1.5Cu-4.0Ni (Distaloy AE of Hoganas of Sweden). The base metal powders were admixed with 4.0 wt% silicon carbide (SiC) powder. The nominal compositions of experimental sintered alloys are given in Table 1. The powder mixtures were added with 1 wt.% zinc stearate as a lubricant. The powder mixtures were compacted into green tensile test bars with green density of 6.5 g/cm3. The green tensile test bars were sintered at 1250 ºC for 45 minutes in a vacuum furnace, Schmetz of Germany, at pressure of 1.28x10-5 MPa. After sintering, specimens were slowly cooled at the cooling rate of 0.1 °C/s.

Characterization

Specimens for optical microscopy (OM) were prepared according to a standard procedure, including cutting, mounting, grinding (180 to 1200 grit silicon carbide papers), polishing (6, 3, and 1 µm diamond pastes), and etching. The etchants employed in this work were 2 % Nital in ethanol. Specimens for scanning electron microscopy (SEM) were prepared according to the standard procedure given above. Microstructural observation was conducted by using Hitachi SU5000.

Phase identification was carried out by using the X-ray diffraction (XRD) technique. The polished specimens were employed for XRD characterization. XRD was performed by using Rigaku TTRAX III X-ray diffractometer with copper source (wavelength of 1,54 Å) and conditions including step size of 0.2°, time 0.5 s/step and angle of 30-100°.

Mechanical property test

Macrohardness test was carried out on un-etched specimens using 100 kgf load (HRB) with 15 indentations per specimen. Tensile property of the sintered materials was carried out at room temperature using Instron Universal Instrument. The stress-strain plots were reported.

Table1 Nominal compositions of experimental sintered alloys

Sintered alloy	Nominal composition (wt. %)						
	C	Si	Mo	Mn	Cu	Ni	Fe
05Mo02Mn	1.2	2.8	0.48	0.19	0.00	0.00	Balance
05Mo15Cu20Ni	1.2	2.8	0.48	0.00	1.44	1.68	Balance
05Mo15Cu40Ni	1.2	2.8	0.48	0.00	1.44	3.84	Balance

Results and Discussion

Sintered 05Mo02Mn alloy

The common microstructural feature of sintered 05Mo02Mn alloy comprised a black particle embedded in a matrix consisting of ferrite halo and pearlite nodules (Fig. 1a). The black particle comprised graphite as the main component (Fig. 1b). Thin and discontinuous proeutectoid carbide particles could be observed along some prior austenite grain boundaries (Fig. 1c). XRD pattern of sintered 05Mo02Mn alloy showed strong peaks of body-centered cubic (bcc) crystal structure of α-ferrite and moderate peaks of orthorhombic crystal structure of M_3C carbide (Fig. 1d).

The microstructure of sintered 05Mo02Mn alloy (Figs. 1a and 1b) resembles that of a ferritic-pearlitic ductile iron. The development of such microstructure involves the formation of black particles and phase transformations in matrix. Regarding the black particle formation, chemical analysis and formation mechanism of a black particle was previously given somewhere else [10]. The phase transformations in matrix can follow the mechanism given for a ductile iron [11]. The stable eutectoid transformation results in formation of ferrite halo surrounding a black particle during slow and continuous cooling. When stable eutectoid transformation stops, it is followed by metastable eutectoid transformation resulting in pearlite nodule formation.

(a) OM image (1000X)

(b) SEM image

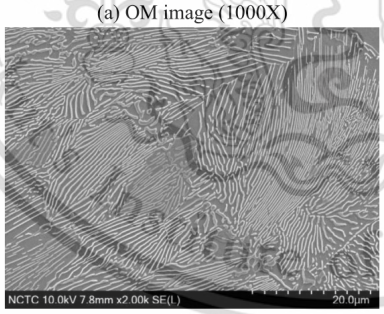

(c) pearlite structure

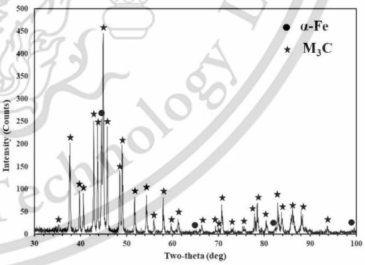

(d) XRD pattern

Figure 1 Characterization of sintered 05Mo02Mn alloy

The microstructure of sintered 05Mo02Mn alloy (Figs. 1a and 1b) resembles that of a ferritic-pearlitic ductile iron. The development of such microstructure involves the formation of black particles and phase transformations in matrix. Regarding the black particle formation, chemical analysis and formation mechanism of a black particle was previously given somewhere else [10]. The phase transformations in matrix can follow the mechanism given for a ductile iron [11]. The stable eutectoid transformation results in formation of ferrite halo surrounding a black particle during slow and continuous cooling. When stable eutectoid transformation stops, it is followed by metastable eutectoid transformation resulting in pearlite nodule formation.

Sintered 05Mo15Cu20Ni alloy

The microstructural feature of sintered 05Mo15Cu20Ni alloy comprised a black particle enveloped with ferrite halo and unresolved zones (Fig. 2a). With high magnification OM, unresolved zones were revealed to contain white bainitic ferrite plates and brown austenite plates (Fig. 2b). The structure consisting of bainitic ferrite and austenite plates is known as ausferrite. XRD pattern of sintered 05Mo15Cu20Ni alloy showed strong peaks of α-ferrite and strong peaks of face-centered cubic (fcc) crystal structure of γ-austenite (Fig. 2c).

As far as the composition of sintered 05Mo15Cu20Ni alloy is concerned, it can be implied that the additions of 1.5 wt% Cu and 2.0 wt% Ni to the sintered 05Mo02Mn alloy result in complete replacement of pearlite nodules by ausferrite. In the field of foundry metallurgy, the ductile iron consisting of graphite nodules, free ferrite and ausferrite is known as dual phase austempered ductile iron (Dual phase ADI) [12]. To obtain the dual phase ADI microstructure, a special heat treatment procedure must be employed. However, in sintered 05Mo15Cu20Ni alloy, the dual phase ADI microstructure is easily obtained by using only a single sintering cycle. It is thus expected that the sintered 05Mo15Cu20Ni alloy can be replaced by some austempered ductile irons in some applications in the future.

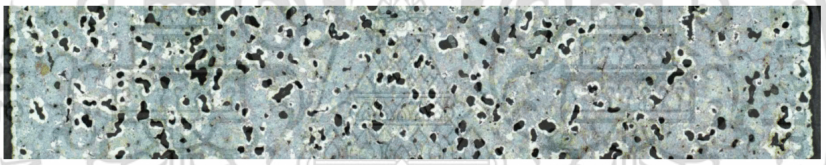

(a) low magnification OM image (100X)

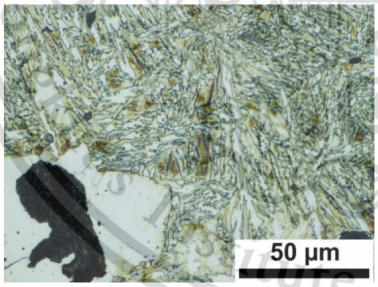

(b) high magnification OM image (1000X)

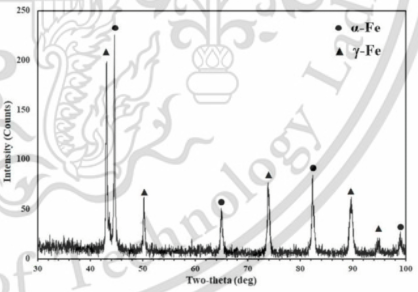

(c) XRD pattern

Figure 2 Characterization of sintered 05Mo15Cu20Ni alloy

Sintered 05Mo15Cu40Ni alloy

The common microstructural feature of sintered 05Mo15Cu40Ni alloy comprised a black particle enveloped with light blue areas and brown zones (Fig. 3a). Ferrite halos disappeared completely from this sintered alloy. With high magnification OM, light blue areas were revealed to be ausferrite, which contained white bainitic ferrite plates and brown austenite plates (Fig. 3b). The brown zones were revealed to be MA islands, which contain martensite-austenite plates. XRD pattern of sintered 05Mo15Cu40Ni alloy showed strong peaks of α-ferrite and strong peaks of γ-austenite (Fig. 3c).

As far as the composition of sintered 05Mo15Cu40Ni alloy is concerned, it can be implied that the additions of 1.5 wt% Cu and 4.0 wt% Ni to the sintered 05Mo02Mn alloy result in complete replacement of pearlite nodules by ausferrite and MA islands. The microstructure comprising black particles, ausferrite and MA islands was previously reported in sintered Fe-Ni-Si-C alloy with Ni content of 4.0 wt% [9]. This type of microstructure was assigned ausferrite-MA ADI microstructure. However, in traditional foundry practices, the ausferrite-MA ADI microstructure has been hardly reported in austempered ductile irons because tempering temperatures are not low to allow martensite to form.

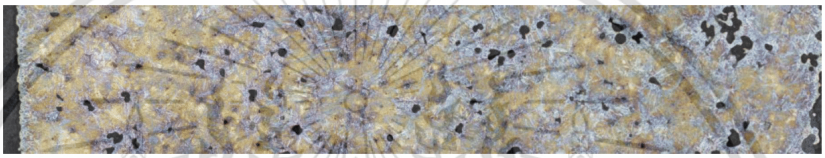

(a) low magnification OM image (100X)

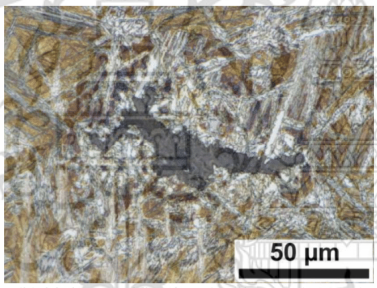

(b) high magnification OM image (1000X)

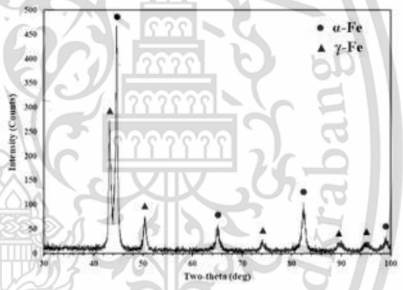

(c) XRD pattern

Figure 3 Characterization of sintered 05Mo15Cu40Ni alloy

Effect of alloying elements on phase transformations

In previous work, the slowly cooled sintered alloy produced from the mixture of Fe-0.50Mo-0.15Mn and 1.2 wt% graphite showed complicated microstructure consisting of proeutectoid $M_{23}C_6$ carbide particles, abnormal ferrite layers, lamellar pearlite (ferrite + $M_{23}C_6$ lamellae), upper bainite (ferrite + M_3C), and inverse bainite (ferrite + M_3C) [13]. Multiple phase transformations occurring in the sintered Fe-0.50Mo-0.15Mn-1.2C alloy (previous work [13]) change to only ferrite and pearlite transformations in the sintered 05Mo02Mn alloy (this work) is due to the incorporation of 2.8 wt% Si into the latter sintered alloy.

When austenite stabilizers of Cu and Ni are added to the sintered 05Mo02Mn alloy to form sintered 05Mo15Cu20Ni alloy, the pearlite transformation is changed to ausferrite transformation. The combined effect of alloying Cu and Ni elements on ausferrite transformation

promotion is the novel phenomenon, which can be added to the previous finding on ausferrite transformation promotion by Cu addition [14].

The increase of Ni content from 2.0 wt.% in sintered 05Mo15Cu20Ni alloy to 4.0 wt.% in sintered 05Mo15Cu40Ni alloy results in formation of MA islands in addition to ausferrite. This confirms the Ni role on martensite formation promotion [15].

Mechanical property

The mechanical properties of experimental sintered alloys are given in Table 2. The sintered 05Mo02Mn alloy showed high tensile strength and hardness but low elongation value. The sintered 05Mo15Cu40Ni alloy showed high tensile strength, hardness, and high elongation value. The sintered 05Mo15Cu20Ni alloy showed the lowest tensile strength and hardness but high elongation value.

The materials showing synergy between strength and ductility are sintered 05Mo15Cu20Ni and 05Mo15Cu40Ni alloys. According to literatures, evading of strength-ductility trade off dilemma in materials depends on several factors, such as, the dual-phase lamellar microstructure [1], core-shell microstructure [2], nano twinning [3], dual heterogeneous structure [4], heterogeneous structure [5], metastability-engineering strategy [6], and micro-banding and the accumulation of a high density of dislocations in single-phase high-entropy alloys (HEAs) [7]. When the microstructural features of sintered 05Mo15Cu20Ni and 05Mo15Cu40Ni alloys are considered, the dual-phase lamellar microstructure seems to be the mechanism for evading of strength-ductility trade off dilemma.

Conclusions

Sintered alloys, produced from iron (Fe) or Fe-based powders mixed with a proper amount of silicon carbide (SiC), could have different microstructures from ferritic-pearlitic ductile iron to dual-phase ADI to ausferrite-MA ADI microstructure, depending on sintered alloy chemistry. It was found that mutual copper (Cu) and nickel (Ni) addition led to low temperature austenite transformations resulting in formations of ausferrite and martensite that totally replaced pearlite. The formation of ausferrite and MA structures led to evading the strength-ductility trade-off dilemma.

Table 2 Mechanical properties of experimental sintered alloys

Sintered alloy	Nominal composition (wt. %)			
	UTS (MPa)	YS (MPa)	Elongation (%)	Hardness (HRB)
05Mo02Mn	1,028.56	685.05	3.46	113.13
05Mo15Cu20Ni	735.52	282.28	6.30	86.85
05Mo15Cu40Ni	1032.45	373.87	7.56	101.43

Acknowledgement

The first author (A.Z. Myo) is grateful for financial support from National Science and Technology Development Agency (NSTDA) TAIST scholarships. This work is financially supported via the project 'Design and manufacturing of replacement parts for railway applications (P1951261)' under NSTDA, Pathum Thani, Thailand. Technical supports are obtained from National Metal and Materials Technology Center (MTEC), Pathum Thani, Thailand.

References

[1] Y.F. Gao, W. Zhang, P.J. Shi, W.L. Ren and Y.B. Zhong, *A mechanistic interpretation of the strength-ductility trade-off and synergy in lamellar microstructures*, Materials Today Advances, Vol.8 (2020), 100103 https://doi.org/10.1016/j.mtadv.2020.100103.

[2] A.K. Srivastava, N.K. Patel, B.R. Kumar, A. Sharma and B. Ahn, *Strength-ductility trade-off in dual-phase steel tailored via controlled phase transformation*, Journal of Materials Engineering and Performance Vol.29 (2020), 2783-2791. https://doi.org/10.1007/s11665-020-04799-6.

[3] Y. Wei, Y. Li, L. Zhu, Y. Liu, X. Lei, G. Wang, Y. Wu, Z. Mi, J. Liu, H. Wang and H. Gao, *Evading the strength-ductility trade-off dilemma in steel through gradient hierarchical nanotwins*, Nature Communications Vol.5 (2014), 3580. https://doi.org/10.1038/ncomms4580.

[4] X.H. Du, W.P. Li, H.T. Chang, T. Yang, G.S. Duan, B.L. Wu, J.C. Huang, F.R. Chen, C.T. Liu, W.S. Chuang, Y. Lu, M.L. Sui, E.W. Huang, *Dual heterogeneous structures lead to ultrahigh strength and uniform ductility in a Co-Cr-Ni medium-entropy alloy*, Nature Communications Vol.11 (2020), 2390. https://doi.org/10.1038/s41467-020-16085-z.

[5] S.W. Wu, G. Wang, Q. Wang, Y.D. Jia, J. Yi, Q.J. Zhai, J.B. Liu, B.A. Sun, H.J. Chu, J. Shen, P.K. Liaw, C.T. Liu, T.Y. Zhang, *Enhancement of strength-ductility trade-off in a high-entropy alloy through a heterogeneous structure*/ Acta Materialia Vol.165 (2019) 444-458. https://doi.org/10.1016/j.actamat.2018.12.012.

[6] Z. Li, K. G. Pradeep, Y. Deng, D. Raabe and C.C. Tasan, *Metastable high-entropy dual-phase alloys overcome the strength-ductility trade-off*, Nature Vol.534 (2016), 227-230 https://doi.org/10.1038/nature17981.

[7] W. Guo, J. Su, W. Lu, C.H. Liebscher, C. Kirchlechner, Y. Ikeda, F. Körmann, X. Liu, Y. Xue and G. Dehm, *Dislocation-induced breakthrough of strength and ductility trade-offin a non-equiatomic high-entropy alloy*, Acta Materialia Vol.185 (2020), 45-54 https://doi.org/10.1016/j.actamat.2019.11.055.

[8] T. Nithimethakul, P. Karin, N. Ohtake, P. Wila, T. Yodkaew, B. Vetayanugul, M. Morakotjinda and R. Tongsri, *The effect of molybdenum on the microstructure and mechanical behaviour of the sintered Fe-Mo-Mn-Si-C composite*, IOP Conf. Series: Materials Science and Engineering Vol. 1137 (2021), 012028 https://doi.org/10.1088/1757-899X/1137/1/012028.

[9] T. Kaewkam, P. Kansuwan, N. Ohtake, P. Wila, R. Krataithong, N. Tosangthum, T. Yotkaew and R. Tongsri, *Sintered Fe-Ni-Si-C alloys*, IOP Conf. Series: Materials Science and Engineering Vol. 1137 (2021), 012035 https://doi.org/10.1088/1757-899X/1137/1/012035.

[10] K. Ruangchai, A. Wiengmoon, M. Morakotjinda, R. Krataitong, D. Tanprayoon, T. Yotkaew, N. Tosangthum, U. Patakham and R. Tongsri, *Microstructure, hardness and wear properties of sintered Fe-Mo-Si-C steels with spheroidal graphite iron/compacted graphite iron-like*, Key Engineering Materials Vol. 751 (2017), 47-52 https://doi.org/10.4028/www.scientific.net/KEM.751.47..

[11] J. Lacaze, J. Sertucha and L.M. Åberg, *Microstructure of as-cast Ferritic-pearlitic nodular cast irons*, ISIJ International Vol.56 (2016), 1606-1615 https://doi.org/10.2355/isijinternational.ISIJINT-2016-108.

[12] A. Basso, M. Caldera, G. Rivera and J. Sikora, *High silicon ductile iron: possible uses in the production of parts with "dual phase ADI" microstructure*, ISIJ International Vol. 52 (2012), 1130-1134 https://doi.org/10.2355/isijinternational.52.1130.

[13] W. Srijampan, A. Wiengmoon, A. Wanalerkngam, S. Boonmee, T. Yotkaew, N. Tosangthum and R. Tongsri, *Identification of carbides and phase transformations in sintered Fe-Mo-Mn-C alloys produced under a slow continuous cooling*, ISIJ International Vol.62 (2022), 2366-2373 https://doi.org/10.2355/isijinternational.ISIJINT-2022-124.

[14] M. Morakotjinda, T. Yotkaew, B. Vetayanugul, A. Wanalerkngam and R. Tongsri, *Promotion of ausferrite formation in as-sintered Fe-Mo-Si-C-(Cu) composites due to Cu addition*, Materials Chemistry and Physics Vol.296 (2023), 127226 https://doi.org/10.1016/j.matchemphys.2022.127226.

[15] G. Mao, R. Cao, C. Cayron, R. Logé, X. Guo, Y. Jiang, and J. Chen, *Microstructural evolution and mechanical property development with nickel addition in low-carbon weld butt joints*, Journal of Materials Processing Technology Vol. 262 (2018), 638-649 https://doi.org/10.1016/j.jmatprotec.2018.07.009.

AUTHOR BIOGRAPHY

Author	Mr. Aung Zaw Myo
Nationality	Myanmar
Email:	65016112@kmitl.ac.th

Educational Background:

2024: Master of Engineering, Automotive and Advanced Transportation Engineering, Faculty of Engineering, King Mongkut's Institute of Technology Ladkrabang, Bangkok, Thailand

2019: Master of Business Administration, Industrial Administration and Development, Faculty of Management Sciences, Kasetsart University, Thailand

2016: Bachelor of Engineering, Aerospace – Propulsion and Flight Vehicles, Myanmar Aerospace Engineering University, Myanmar

Conference Participation and Publication:

[1] A Z Myo, M Srilomsak, M Morakotjinda, T Yotkaew, N Tosangthum, P Wila, R Tongsri, and K Inaba, "Sintered Steels with Improved Ductility Produced from Diffusion-Alloyed Powders", 2024, The 13th TSME International Conference on Mechanical Engineering 2023 (TSME-ICoME 2023), 12-15 DECEMBER, Chiang Mai, Thailand.

[2] A Z Myo, M Srilomsak, K Inaba, P. Nakornkaew, M Morakotjinda, N Tosangthum, T Yotkaew, and R Tongsri, "Ausferrite Promotion in Sintered Low Molybdenum Containing Alloy by Mutual Copper and Nickel Addition", 2023, International Conference on Materials Processing Technology 2023, 23-24 NOVEMBER, Bangkok, Thailand.

[3] A Z Myo, J Thaweepaiboonwong, "The effect of human resource management and supervisor leadership styles on innovative work behaviors of employee working in manufacturing sectors in Chon Buri

province, Thailand", 2019, Modern Management Journal, 2019, ISSN 2630-0664, July-December, Submitted, 2019.